
Unterschrift BetreuerIn



TECHNISCHE
UNIVERSITÄT
WIEN

DIPLOMARBEIT

Implementation of a confocal Synchrotron radiation induced micro X-ray fluorescence system for bone analysis at the X-ray fluorescence beamline of ELETTRA Synchrotron

ausgeführt am Atominstitut
der Technischen Universität Wien

unter der Anleitung von
Ao.Univ.Prof. Dipl.-Ing. Christina Strelt

durch

Lukas Perneczky

Hagenmüllergasse 28/32
1030 Wien

22. März 2018

Unterschrift StudentIn

Acknowledgements

I would first like to express my sincerest gratitude to my thesis advisor Ao.Univ.Prof. Dipl.-Ing. Christina Streli for her continuous support and encouragement, her confidence in my work and for always having an open door whenever I ran into difficulties.

I am immensely grateful to my second advisor Anna Turyanskaya, for being an infinite source of encouragement, for helping and supporting me in any and every possible way, but also for assisting me in improving my work by being critical when necessary.

I would also like to thank Ao.Univ.Prof.i.R. Dipl.-Ing. Dr.techn. Peter Wobrauschek for sharing his immense knowledge as well as his constant enthusiasm and for always taking the time to aid with any difficulties that might occur.

I would like to thank the all members of the X-ray physics group for creating a friendly, creative and productive work environment. I count myself lucky to have worked with this group of people.

Finally, I can not thank my parents Eva and Gida, my brothers Nikolaus and Julian, my girlfriend Joana, as well as all my friends enough, for their endless love and support and for always believing in me, even in times when I had difficulties to do so myself.

The research leading to the results presented in this work has received funding from the Austrian Science Fund (FWF, project number: P27715).

Abstract

Micro X-Ray fluorescence (μ XRF) is a well established analytical method, capable of the non-destructive determination of spatial distributions of major, minor and trace elements in a wide range of different types of samples. A common area of application is the determination of the distributions of trace elements in biological samples, e.g. bone samples. The multicomponent nature and complicated structure of biological samples present a challenge in the analysis of such specimens. For different elemental components the information depth is strongly varying, due to the varying absorption of different fluorescence energies, when propagating through the sample. Furthermore, since the micro beam penetrates the sample at a 45° angle, this also leads to the distortion of the lateral resolution to some extent. The method of confocal μ XRF is able to resolve these issues by introducing a focussing X-ray optic between sample and detector, limiting the detector's field of vision. The overlap of the foci of the primary X-ray optic in the excitation channel and of the additional X-ray optic in the detection channel forms the so-called confocal volume. Only X-rays originating from this defined volume reach the detector, eliminating the unwanted contributions from subjacent layers of the sample.

The use of synchrotron radiation for μ XRF experiments is highly advantageous, especially for the measurement of trace elements, which can be time consuming, as the high brightness and low background conditions of synchrotron sources reduce the required measurement time per point considerably.

The confocal μ XRF spectrometer of Atominstut (ATI) was modified for the implementation at a synchrotron source. In order to focus the parallel synchrotron beam, the full lens in the excitation channel was replaced by a half lens. To accurately adjust the angle of the half lens to the incoming beam, an adjustment mechanism was designed and constructed. The Si(Li) detector was replaced by a smaller SDD detector, which was implemented in the control software, while the chamber was adapted to the different detector's size.

The ATI μ XRF spectrometer was transported to and set up at the XRF beamline of the synchrotron facility ELETTRA (Basovizza, Trieste, Italy) in the course of two beamtimes. Since there is no μ XRF setup currently available at ELETTRA, the goal was to examine the possible viability of such a setup and test its capabilities. The spectrometer was successfully adjusted during both experiments. In order to determine the capabilities of the different setups and to compare them with lab measurements, several areas on different bone samples were scanned and are presented in this work.

Additionally, a software for the validation and creation of elemental maps from fitted data was developed.

Parts of this work have been submitted for publication:

1. L. Perneczky, M. Rauwolf, D. Ingerle, D. Eichert, F. Brigidi, W. Jark, S. Bjeoumikhova, G. Pepponi, P. Wobrauschek, C. Streli, and A. Turyanskaya. Temporary implementation and testing of a confocal SR- μ XRF system for bone analysis at the X-Ray Fluorescence beamline at Elettra. submitted to Nuclear Instruments & Methods in Physics Research A, 2018.

Some parts were also presented at conferences in the form of posters:

1. L. Perneczky, A. Turyanskaya, S. Smolek, M. Rauwolf, P. Wobrauschek, C. Streli: "Confocal μ XRF spectrometer for analysis of 3-dimensional spatial distribution of low to high Z elements"; Poster: 66th Yearly Meeting of the Austrian Physical Society (2016), Vienna, Austria; 2016-09-27 - 2016-09-29.

2. L. Perneczky, A. Turyanskaya, S. Smolek, M. Rauwolf, P. Wobrauschek, C. Streli: "Confocal μ XRF spectrometer for low to high Z element analysis"; Poster: 26th Seminar Activation Analysis and Gamma Spectroscopy (SAAGAS 26), Vienna, Austria; 2017-02-20 - 2017-02-22.

3. A. Turyanskaya, L. Perneczky, M. Rauwolf, P. Wobrauschek, C. Streli, D. Eichert, F. Brigidi, W. Jark, S. Bjeoumikhova, G. Pepponi, P. Roschger: "Implementation of a Confocal SR-microXRF System for Bone Analysis at the X-ray Fluorescence Beam Line at Elettra"; Poster: Annual Denver X-ray Conference 2017, Big Sky, USA; 2017-07-31 - 2017-08-04.

Additionally, during the course of this thesis, I was given the opportunity to contribute to other ongoing research projects of the X-ray physics group:

Submitted for publication:

1. A. Svirkova, A. Turyanskaya, L. Perneczky, C. Streli, and M. Marchetti-Deschmann. Multimodal imaging by MALDI MS and μ XRF. submitted to Analyst, 2018.

Posters:

1. G. Gamauf, L. Perneczky, A. Turyanskaya, J.H. Sterba, C. Streli: "Non-destructive depth analysis of Sueki ceramics using confocal μ XRF spectrometry combined with NAA data"; Poster: 26th Seminar Activation Analysis and Gamma Spectroscopy (SAA-GAS 26), Vienna, Austria; 2017-02-20 - 2017-02-22.
2. A. Turyanskaya, T. Grünewald, M. Meischel, M. Rauwolf, J. Prost, L. Perneczky, H. Lichtenegger, S.E. Stanzl-Tschegg, A. Weinberg, P. Wobrauschek, C. Streli: "Elemental imaging on biodegradable orthopedic implants by μ XRF"; Poster: 65nd Annual Denver X-ray Conference 2016, Chicago, USA; 2016-08-01 - 2016-08-05.
3. A. Turyanskaya, T. Gruenewald, M. Rauwolf, M. Meischel, J. Prost, L. Perneczky, H. Lichtenegger, S.E. Stanzl-Tschegg, A. Weinberg, P. Wobrauschek, C. Streli: "Magnesium-based biodegradable orthopedic implants by μ XRF"; Poster: European Conference on X-ray Spectrometry (EXRS 2016), Gothenburg, Sweden; 2016-06-19 - 2016-06-24.
4. A. Turyanskaya, M. Rauwolf, L. Perneczky, T. Gruenewald, M. Meischel, H. Lichtenegger, S.E. Stanzl-Tschegg, A. Weinberg, P. Wobrauschek, C. Streli: " μ XRF spectrometer at Atominstitut for bio-imaging applications"; Poster: 26th Seminar Activation Analysis and Gamma Spectroscopy (SAAGAS 26), Vienna, Austria; 2017-02-20 - 2017-02-22.
5. A. Turyanskaya, M. Rauwolf, L. Perneczky, T. Grünewald, M. Meischel, H. Lichtenegger, S.E. Stanzl-Tschegg, A. Weinberg, P. Wobrauschek, C. Streli: "Exploitation of μ XRF spectrometer for Bio-Imaging"; Poster: X-Ray Microscopy Conference (XRM 2016), Oxford, UK; 2016-08-15 - 2016-08-19.

Talks:

1. A. Turyanskaya, M. Rauwolf, L. Perneczky, A. Svirkova, M. Bonta, A. Limbeck, M. Marchetti-Deschmann, A. Roschger, P. Roschger, P. Wobrauschek, C. Streli: "Multimodal Imaging of Biological Samples: Correlation of μ XRF with MALDI-MSI and with LA-ICP-MS"; Keynote Lecture: Annual Denver X-ray Conference 2017, Big Sky, USA; 2017-07-31 - 2017-08-04.

Kurzfassung

Mikro-Röntgenfluoreszenzanalyse (Mikro-RFA) ist eine etablierte analytische Methode, mit der man zerstörungsfrei die Verteilungen von Haupt-, Neben- und Spurenelementen in einer Vielzahl von unterschiedlichen Arten von Proben bestimmen kann. Eine verbreitete Anwendung ist die Bestimmung der Verteilung von Spurenelementen in biologischen Proben, wie z.B. in Knochenproben. Die mehrkomponentige Beschaffenheit und komplizierte Struktur von biologischen Proben stellt eine Herausforderung für deren Analyse dar. Die Informationstiefe für unterschiedliche Elemente variiert deutlich, aufgrund der unterschiedlich starken Absorption der verschiedenen Fluoreszenz Energien beim Durchgang durch die Probe. Da der fokussierte Strahl unter einem Winkel von 45° auf die Probe trifft, kommt es zudem zu einer lateralen Verzerrung der Abbildung. Die Methode der konfokalen Mikro-RFA schafft es, diese Schwierigkeiten zu überwinden, indem eine fokussierende Röntgenoptik zwischen Probe und Detektor das Sichtfeld des Detektors begrenzt. Die Überschneidung der Fokusse der primären Röntgenoptik im Anregungskanal und der zusätzlichen Röntgenoptik im Detektionsskanal bilden das sogenannte konfokale Volumen. Nur Röntgenstrahlen die in diesem definierten Volumen entstehen erreichen den Detektor, deshalb werden unerwünschte Beiträge aus tieferen Schichten der Probe beseitigt.

Die Verwendung von Synchrotronstrahlung ist generell vorteilhaft für Mikro-RFA Experimente, insbesondere aber für die oft zeitaufwendige Messung von Spurenelementen, da die hohe Brillianz und der niedrige spektrale Hintergrund von Synchrotronquellen die benötigte Messzeit pro Punkt signifikant verringern.

Das konfokale Mikro-RFA Spektrometer des Atom Instituts (ATI) wurde modifiziert, um die Installation an einer Synchrotronquelle zu ermöglichen. Um den parallelen Synchrotronstrahl auf die Probe zu fokussieren, wurde die Volllinse im Anregungskanal durch eine Halblinse ersetzt. Damit man den Winkel der Halblinse präzise einstellen kann, wurde ein spezieller Mechanismus entwickelt und hergestellt. Der Si(Li)-Detektor wurde durch einen kleineren SSD Detektor ersetzt, der in die Steuerungssoftware eingebunden wurde. Außerdem wurde die Vakuumkammer an die unterschiedliche Detektorgröße angepasst.

Das ATI Mikro-RFA-Spektrometer wurde im Rahmen von zwei "Beamtimes" zur XRF "Beamline" des Synchrotrons ELETTRA (Basovizza, Trieste, Italien) transportiert, aufgebaut und justiert. Da es momentan keine Mikro-RFA Anlage am Synchrotron ELETTRA gibt, war es das Ziel, die Realisierbarkeit eines derartigen Aufbaus zu prüfen und dessen Leistungsvermögen zu erproben. Das Spektrometer wurde bei beiden

“Beamtimes” erfolgreich aufgebaut und justiert. Um das Leistungsvermögen der beiden Aufbauten zu testen und sie mit Labormessungen zu vergleichen, wurden mehrere Bereiche auf unterschiedlichen Knochenproben abgerastert. Diese Messungen werden in der vorliegenden Arbeit präsentiert.

Zusätzlich wurde ein Programm zur Überprüfung und Erstellung von Elementkarten aus gefitteten Daten entwickelt.

Teile dieser Arbeit wurden zur Veröffentlichung eingereicht:

1. L. Perneczky, M. Rauwolf, D. Ingerle, D. Eichert, F. Brigidi, W. Jark, S. Bjeoumikhova, G. Peponi, P. Wobrauschek, C. Streli, and A. Turyanskaya. Temporary implementation and testing of a confocal SR- μ XRF system for bone analysis at the X-Ray Fluorescence beamline at Elettra. submitted to Nuclear Instruments & Methods in Physics Research A, 2018.

Außerdem wurden Teile der Arbeit als Poster präsentiert:

1. L. Perneczky, A. Turyanskaya, S. Smolek, M. Rauwolf, P. Wobrauschek, C. Streli: "Confocal μ XRF spectrometer for analysis of 3-dimensional spatial distribution of low to high Z elements"; Poster: 66th Yearly Meeting of the Austrian Physical Society (2016), Vienna, Austria; 2016-09-27 - 2016-09-29.

2. L. Perneczky, A. Turyanskaya, S. Smolek, M. Rauwolf, P. Wobrauschek, C. Streli: "Confocal μ XRF spectrometer for low to high Z element analysis"; Poster: 26th Seminar Activation Analysis and Gamma Spectroscopy (SAAGAS 26), Vienna, Austria; 2017-02-20 - 2017-02-22.

3. A. Turyanskaya, L. Perneczky, M. Rauwolf, P. Wobrauschek, C. Streli, D. Eichert, F. Brigidi, W. Jark, S. Bjeoumikhova, G. Peponi, P. Roschger: "Implementation of a Confocal SR-microXRF System for Bone Analysis at the X-ray Fluorescence Beam Line at Elettra"; Poster: Annual Denver X-ray Conference 2017, Big Sky, USA; 2017-07-31 - 2017-08-04.

Darüber hinaus, hatte ich die Möglichkeit an weiteren Forschungsprojekten der Arbeitsgruppe Röntgenphysik mitzuarbeiten:

Zur Veröffentlichung eingereicht:

1. A. Svirkova, A. Turyanskaya, L. Perneczky, C. Streli, and M. Marchetti-Deschmann. Multimodal imaging by MALDI MS and μ XRF. submitted to Analyst, 2018.

Poster:

1. G. Gamauf, L. Perneczky, A. Turyanskaya, J.H. Sterba, C. Streli: "Non-destructive depth analysis of Sueki ceramics using confocal μ XRF spectrometry combined with NAA data"; Poster: 26th Seminar Activation Analysis and Gamma Spectroscopy (SAA-GAS 26), Vienna, Austria; 2017-02-20 - 2017-02-22.
2. A. Turyanskaya, T. Grünewald, M. Meischel, M. Rauwolf, J. Prost, L. Perneczky, H. Lichtenegger, S.E. Stanzl-Tschegg, A. Weinberg, P. Wobrauschek, C. Streli: "Elemental imaging on biodegradable orthopedic implants by μ XRF"; Poster: 65nd Annual Denver X-ray Conference 2016, Chicago, USA; 2016-08-01 - 2016-08-05.
3. A. Turyanskaya, T. Gruenewald, M. Rauwolf, M. Meischel, J. Prost, L. Perneczky, H. Lichtenegger, S.E. Stanzl-Tschegg, A. Weinberg, P. Wobrauschek, C. Streli: "Magnesium-based biodegradable orthopedic implants by μ XRF"; Poster: European Conference on X-ray Spectrometry (EXRS 2016), Gothenburg, Sweden; 2016-06-19 - 2016-06-24.
4. A. Turyanskaya, M. Rauwolf, L. Perneczky, T. Gruenewald, M. Meischel, H. Lichtenegger, S.E. Stanzl-Tschegg, A. Weinberg, P. Wobrauschek, C. Streli: " μ XRF spectrometer at Atominstitut for bio-imaging applications"; Poster: 26th Seminar Activation Analysis and Gamma Spectroscopy (SAAGAS 26), Vienna, Austria; 2017-02-20 - 2017-02-22.
5. A. Turyanskaya, M. Rauwolf, L. Perneczky, T. Grünewald, M. Meischel, H. Lichtenegger, S.E. Stanzl-Tschegg, A. Weinberg, P. Wobrauschek, C. Streli: "Exploitation of μ XRF spectrometer for Bio-Imaging"; Poster: X-Ray Microscopy Conference (XRM 2016), Oxford, UK; 2016-08-15 - 2016-08-19.

Vorträge:

1. A. Turyanskaya, M. Rauwolf, L. Perneczky, A. Svirkova, M. Bonta, A. Limbeck, M. Marchetti-Deschmann, A. Roschger, P. Roschger, P. Wobrauschek, C. Streli: "Multimodal Imaging of Biological Samples: Correlation of μ XRF with MALDI-MSI and with LA-ICP-MS"; Keynote Lecture: Annual Denver X-ray Conference 2017, Big Sky, USA; 2017-07-31 - 2017-08-04.

Contents

1. Introduction	1
2. Theoretical Background	3
2.1. Properties Of X-Rays	3
2.2. Interaction Of X-Rays With Matter	3
2.2.1. Photoelectric Effect (Emission Of Characteristic X-Rays / Auger electrons)	4
2.2.2. Coherent Scattering (or Elastic/Rayleigh)	7
2.2.3. Incoherent Scattering (or Inelastic/Compton)	7
2.2.4. Lambert-Beer Law	8
2.2.5. Penetration Depth / Information Depth	9
2.2.6. Refraction, Reflection & Total-Reflection Of X-Rays	9
2.2.7. Bragg Diffraction	10
2.3. Characteristic Spectrum	11
2.4. Continuous Spectrum	12
3. Methods & Techniques	13
3.1. EDXRF (Energy Dispersive X-Ray Fluorescence)	13
3.2. Components Of An EDXRF Spectrometer	14
3.2.1. X-Ray Sources	14
3.2.2. X-Ray Optics	18
3.2.3. Semi-Conductor Detectors	21
3.3. μ XRF	24
3.3.1. μ XRF	24
3.3.2. Confocal μ XRF	25
4. Experimental Setup & Data Analysis	27
4.1. Components Of ATI spectrometer	27
4.2. Adjustment procedure	27
4.2.1. Adjusting Polycapillary Full-Lens	28
4.2.2. Adjusting The Microscope Focus	28
4.2.3. Adjusting Polycapillary Half-lens	29
4.2.4. Determining The Size The Confocal Volume	30
4.3. Data Analysis	30

4.4.	Data Visualization with LP-map	31
4.4.1.	Plotting Elemental Maps	32
4.4.2.	Plotting Spectra	36
5.	Implementation Of The ATI μXRF Spectrometer At The ELETTRA Synchrotron	38
5.1.	Beamline specifications	38
5.2.	1st Beamtime	40
5.2.1.	Preparations	40
5.2.2.	Setup Procedure	41
5.2.3.	Summary	45
5.3.	Second Beamtime	46
5.3.1.	Preparations & Improvements	46
5.3.2.	Setup Procedure	51
5.3.3.	Summary	59
5.4.	Measurements	59
5.4.1.	MN4 - Area B	59
5.4.2.	MN8 - Area B	66
5.4.3.	MN8 - Area C	68
5.4.4.	TU14	70
5.4.5.	TUx1A	72
6.	Conclusion	74
	References	75
A.	Part Drawings	77
A.1.	First beamtime	77
A.2.	Second beamtime	82

1. Introduction

X-ray fluorescence (XRF) spectroscopy is a well established analytical method for a variety of different samples, from solid bulk samples or thin slices, to powders or even liquids. The method is non-destructive, opening up the option to analyze valuable items (e.g. cultural heritage) or combining it with other analytical methods [1]. While standard XRF is perfectly suited to determine the elemental composition of a sample, it is not capable of mapping the inhomogenous structure of, for example a biological sample. This task can be realized by the method of micro-X-ray fluorescence (μ XRF) spectroscopy. Here, the exciting radiation is focussed onto a small spot on the sample. By moving the sample through this focussed beam in steps and performing measurements at each step, elemental maps of the sample can be acquired. Depending on the type of focussing optic, the range of achievable spatial resolution goes from μm to mm. However, depending on the fluorescence energy, the detected radiation will originate not only from surface layers, but also from deeper layers. On top of that, due to the 45° geometry of μ XRF setups, the photons are also coming from adjacent regions. This leads to the distortion of the spatial resolution to some extent. The method of confocal μ XRF overcomes these issues, as it allows the analysis of the elemental distribution within one well-defined layer, e.g. the surface of the sample. In addition, it also makes depth scans or 3D scans possible.

ATI's μ XRF spectrometer was constructed in the course of a previous master thesis [2]. With the whole instrument being situated in a vacuum chamber and the utilization of a detector with ultra-thin window, the spectrometer is capable of measuring low to high Z elements. Eventually, the spectrometer was upgraded by a second polycapillary optic in the detection channel [3], opening up the possibility of confocal μ XRF measuring. This setup has already proven useful in the lab for the analysis of bone samples [4].

The utilization of synchrotron radiation represents a significant improvement for μ XRF experiments, as the high brilliance substantially reduces the required measurement time per point and the linear polarization results in low background conditions. There are not many confocal synchrotron setups available worldwide, and at the moment there is no such setup available at the synchrotron source ELETTRA in Basovizza, Italy [5]. For this reason, the viability of a confocal μ XRF instrument at ELETTRA was of great interest. With its compact design, the ATI μ XRF spectrometer was a perfect candidate for a temporary implementation at ELETTRA, in order to examine the feasibility of such a setup on the one hand, and to test the practicability of such a transportation

process on the other.

The goals of this work was to characterize the capabilities of the spectrometer, to prepare and adapt the setup for transportation and implementation at ELETTRA, and hopefully to successfully adjust the spectrometer to the synchrotron beam and perform test measurements on different bone samples. A consistent adjustment procedure for the synchrotron environment had to be developed. The Si(Li) detector's large size and heavy weight, as well as the liquid nitrogen cooling, made it unpractical for transportation. Therefore, it had to be replaced by a smaller SDD detector, which had to be implemented in the software, while the chamber had to be adapted to the different detector's snout. The full lens in the excitation channel had to be replaced by a half lens optic, in order to focus the incoming parallel beam at the synchrotron beamline. This also lead to the requirement of a new adjustment mechanism, since the small acceptance angle of such an optic makes the precise alignment a necessity. Additionally, while the measurement software of the ATI μ XRF spectrometer is both sophisticated and user-friendly, the available software for the creating of elemental maps was leaving room for improvement. Thus, the new visualization software "LP-map" was developed, enabling easy creation of elemental maps from processed data, while also improving the whole processing and data analysis procedure.

After giving an overview of the relevant theoretical background and the experimental methods, this thesis aims to give a detailed description of all development steps leading up to the two beamtimes at ELETTRA - Sincrotrone. Finally, all successfully acquired measurements will be presented and discussed.

2. Theoretical Background

For the formulation of this section (as well as section 3) the following documents were consulted: [6, 7, 8, 9].

2.1. Properties Of X-Rays

The spectrum of X-rays goes from 100 eV to several 100 keV:

- 100 eV - 1 keV: soft X-rays
- 1 keV - 25 keV: energy scale of XRF, fluorescence radiation
- 25 keV - 120 keV: can also be used for elemental analysis (higher Z elements)
- > 120 keV: hard x-rays, e.g. for technical radiography

X-rays are invisible. They propagate in straight lines with light speed. They are unaffected by electrical and magnetical fields. They are differentially absorbed while passing through matter of varying composition, density, or thickness. They can be reflected, diffracted, refracted, and polarized. They are capable of ionizing gases, affecting electrical properties of liquids and solids. They are able to liberate photoelectrons and recoil electrons. They are emitted in a continuous spectrum (bremsstrahlung) as well as in a line spectrum characteristic for the chemical elements. X-rays have absorption spectra characteristic of the chemical elements.

As for any electromagnetic wave, the relation of energy and wavelength is given by

$$E = \frac{h \cdot c}{\lambda} \quad (1)$$

2.2. Interaction Of X-Rays With Matter

X-rays interact with matter in a multitude of different ways, giving rise to a variety of analytical methods. Figure 1 illustrates the possible interactions of X-ray with matter. They can be elastically or inelastically scattered, or they are absorbed in the target material, giving rise to photoelectrons, and consequently fluorescence radiation or Auger electrons.

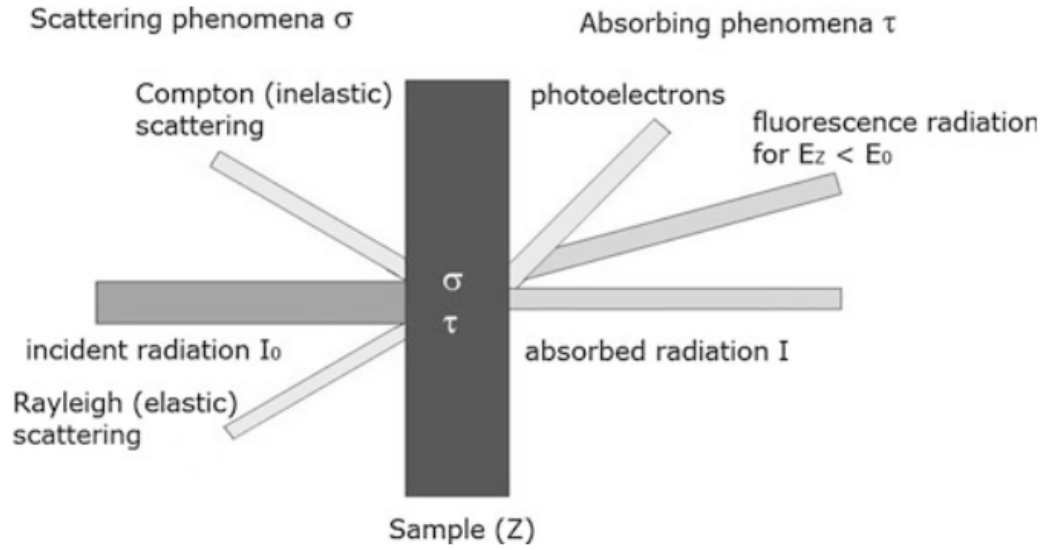


Figure 1: Illustration of possible interactions of X-rays with matter [6].

2.2.1. Photoelectric Effect (Emission Of Characteristic X-Rays / Auger electrons)

If a high energy photon (with energy E_{ph}) strikes a bound atomic electron (with binding energy ϕ), and if $E_{ph} > \phi$, there is a possibility that the photon is absorbed while the electron is ejected from its atomic position and leaves the atom with a kinetic energy of $(E_{ph} - \phi)$. The ejected electron is called a photoelectron. It leaves behind a vacancy (at energy E_1), which eventually will be filled by another electron from a higher energy shell (at energy E_2). The energy that becomes available ($E = E_2 - E_1$) will either go to the creation of a characteristic photon or it will be transferred to another bound electron, which can then leave the atom, a so-called Auger electron. For XRF, we are only interested in the characteristic radiation. The fluorescence yield (Fig. 2), which is the probability that the excited atom is deexcited by emission of a photon is approximately given by:

$$\omega = \frac{Z^4}{A + Z^4} \quad (2)$$

where Z is the atomic number and A is constant for a given shell but varies between different shells. As can be seen in Figure 2, for the lowest values of the atomic number Z , the Auger electron yield is dominating and the fluorescence yield is comparatively

small, making it difficult to detect these low Z elements using X-ray fluorescence.

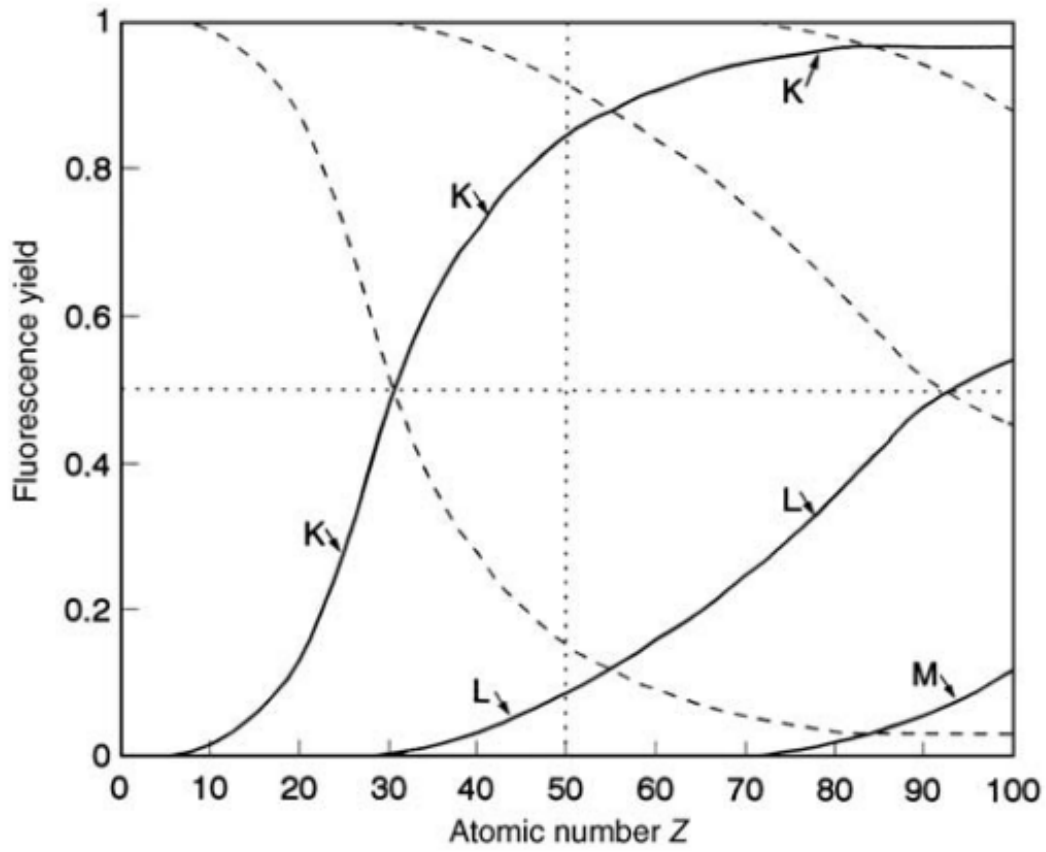


Figure 2: Fluorescence yield (solid lines) and the competing Auger electron yield (dotted lines) for K, L and M shells [7].

For the deexcitation process, not all electron transitions are possible. The emission is governed by the quantum mechanical selection rules:

$$\Delta n > 0 \quad (3)$$

$$\Delta l = \pm 1 \quad (4)$$

$$\Delta j = 0, \pm 1 \quad (5)$$

where n is the principal quantum number, l is the angular momentum quantum number and j is the total angular momentum number. Figure 3 shows possible electron transitions. The transitions are labeled using the Siegbahn notation, where the

first letter describes the final shell of the transition, and the greek letter with subscript number contains the remaining information about the subshells involved in the transition. The subsequently produced characteristic X-ray lines have the same names as the energy transitions they originated from.

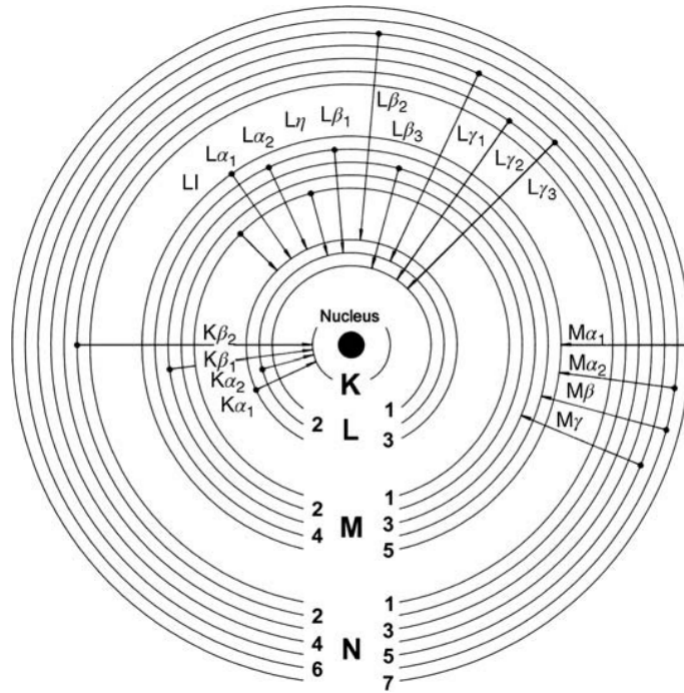


Figure 3: Illustration of possible electron transitions for the K,L and M shells, labeled using the Siegbahn notation [7].

2.2.2. Coherent Scattering (or Elastic/Rayleigh)

In the case of coherent or elastic scattering, photons are scattered by bound atomic electrons, only changing the photon direction while the energy stays the same. For unpolarized incoming X-rays, the scattering intensity can be described by [6]

$$I_{scat} = I_0 \frac{1}{r^2} \left(\frac{e^2}{m_0 c^2} \right)^2 (1 + \cos^2 \vartheta) \quad (6)$$

with

- I_{scat} ... scattered intensity
- I_0 ... primary intensity
- r ... distance to the observation point
- e, m_0 ... electron charge and mass
- ϑ ... scatter angle

There is a definite phase relation between the incoming and outgoing waves, hence it is called coherent scattering. Summing up the amplitudes of the radiation coherently scattered by each electron in an atom gives the total scattered intensity of this atom. Rayleigh scattering is predominantly occurring at low energies and for high Z materials.

2.2.3. Incoherent Scattering (or Inelastic/Compton)

Another possible interaction is incoherent or inelastic scattering. Here, the incoming photon loses energy and changes direction. The relative energy loss is described by the Compton formula

$$\frac{E_{scat}}{E_0} = 1 + \frac{1}{mc^2} (1 - \cos \vartheta) \quad (7)$$

For incoherent scattering there is no interference between the scattered waves, therefore the total scattered intensity is given by the sum of the scattering intensities of all individual electrons. The inelastic cross section is relatively independent of the atomic number Z, i.e. the number of electrons of the atom. At lower energies the inelastic scattering cross section is lower than for elastic scattering, but at higher energies the inelastic cross section is higher.

2.2.4. Lambert-Beer Law

When X-Rays pass through matter some of them will be lost, either by photoelectric absorption or scattering, as described in the previous sections. The Lambert-Beer law describes this attenuation of X-ray radiation:

$$I(x) = I_0 e^{-\mu(E)x} = I_0 e^{-\frac{\mu(E)}{\rho} \frac{m}{F}} \quad (8)$$

The attenuation is exponentially dependent on the distance x traveled through the matter and the linear attenuation coefficient

$$\mu(E) = \tau(E) + \sigma_{coh}(E) + \sigma_{inc}(E) \quad (9)$$

$$\mu(E) = \mu_m \cdot \rho \quad (10)$$

where

- $\mu(E)$ is the linear attenuation coefficient
- μ_m is the mass attenuation coefficient
- $\tau(E)$ is the coefficient for photoabsorption
- $\sigma_{coh}(E)$ is the elastic scattering cross-section (Rayleigh-Scattering)
- $\sigma_{inc}(E)$ is the inelastic scattering cross-section (Compton-Scattering)

These coefficients, and thus the attenuation coefficient, are dependent on the energy of the incoming radiation as well as material properties such as chemical composition, density and structure of the irradiated matter. Figure 4 displays the total photon cross section and the contributions of the different interactions as a function of photon energy for C and Pb.

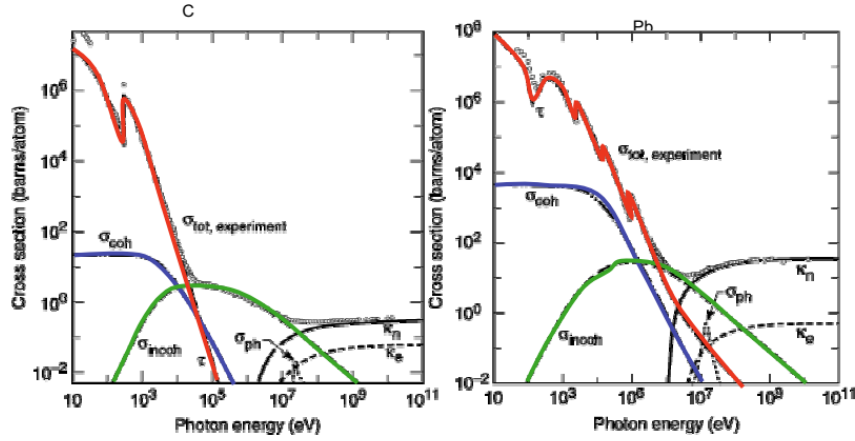


Figure 4: Total photon cross section (σ_{tot}) for C (left) and Pb (right), showing the contributions of different interactions, i.e. coherent (σ_{coh} , in blue) and incoherent scattering (σ_{incoh} , in green), photoelectric effect (τ , in red) and pair production [8].

2.2.5. Penetration Depth / Information Depth

The penetration depth describes how deep X-rays can penetrate into a material. It is defined as the depth at which the incoming radiation has been attenuated by a factor of $\frac{1}{e}$. The penetration depth can be written as

$$d_{penetration} = \frac{1}{\mu} \quad (11)$$

The information depth is the depth in the sample, from which $\frac{1}{e}$ of the fluorescence radiation can escape.

2.2.6. Refraction, Reflection & Total-Reflection Of X-Rays

The angles of refraction and reflection of electromagnetic waves when propagating from one medium to another are described by Snell's law:

$$n \cos \varphi = n' \cos \varphi' \quad (12)$$

with

$$n = 1 - \delta - i\beta \quad (13)$$

where δ (between $\sim 10^{-6}$ and 10^{-7}) describes the dispersion and β (between $\sim 10^{-10}$ and 10^{-6}) describes the absorption of the wave. For X-rays, $n = 1$ in vacuum (and approximately also in air), while $n < 1$ for other materials. This means, that when X-rays are propagating from vacuum to another medium, they will be refracted towards the boundary. Since the margin between different values of n are generally quite small (n is close to 1 for all materials), the refraction angle is also small. However, if the incidence angle onto a medium is small enough, the refracted beam will not penetrate the medium, but rather it will be total reflected. The critical angle for total reflection can be approximated by

$$\varphi_{crit} \approx \sqrt{2\delta} \quad (14)$$

and is typically in the order of several mrad. The total reflection of X-rays has an application that is crucial for μ XRF techniques, namely polycapillary optics (section 3.2.2.3).

2.2.7. Bragg Diffraction

Like all waves, X-rays can be diffracted on the periodical structure of a crystal lattice. The diffracted wave will be a superposition of waves, with each scattering center adding a diffracted wave to the result. Depending on the wavelength of the incoming wave, the incidence angle and the lattice spacing, this superposition will either lead to constructive or destructive interference. This is described by Bragg's law

$$n \cdot \lambda = 2d \cdot \sin\vartheta \quad (15)$$

with

- n ... order of diffraction
- λ ... wavelength of the scattered radiation
- d ... spacing of the scattering lattice
- ϑ ... scattering angle

This relation is illustrated in Figure 5. For a fixed value of d (e.g. in a single crystal lattice) and at a fixed angle, the possible values of λ are unambiguously given by Bragg's

law. An important application of this principle are monochromators (section 3.2.2.2), where it is utilized to filter out a small energy band from a continuous spectrum.

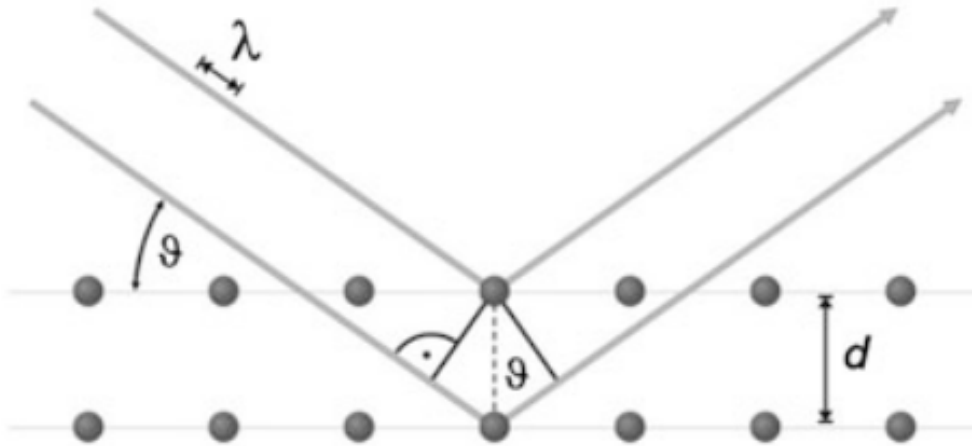


Figure 5: Bragg diffraction of a wave with wavelength λ on a lattice with spacing d at an angle ϑ [6].

2.3. Characteristic Spectrum

Characteristic radiation originates from electron transitions between energy shells of an atom (section 2.2.1). The energy of this radiation is uniquely related to the element that is responsible for its emission by Moseley's law (Fig. 6).

$$\frac{1}{\lambda} = k(Z - \sigma)^2 \quad (16)$$

with

- λ ... wavelength of the emitted radiation
- Z ... atomic number
- k ... proportionality constant, dependent on involved energy shells
- σ ... screening constant

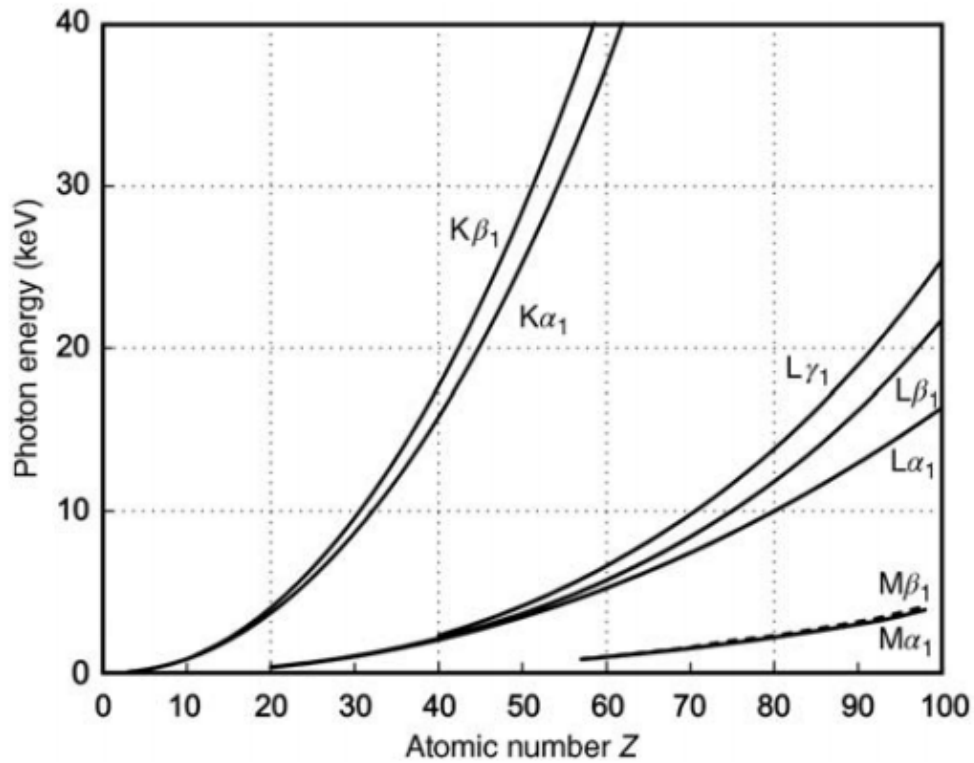


Figure 6: Plot of Mosely's law

Therefore, by measuring the characteristic energies of the fluorescence radiation coming from the sample, one can identify the elements contained in the sample, which is the basic principle of X-ray fluorescence spectroscopy.

2.4. Continuous Spectrum

The continuous spectrum is related to the fact that any charged particle emits radiation when it is accelerated or decelerated. When e.g. a free electron comes close to an atom, it gets deflected (is decelerated) in the coulomb field of the nucleus. The energy that the electron loses is emitted in the form of radiation, the so called "bremsstrahlung". Here, unlike the case of the quantized energy levels of the bound electrons in the atom, the energy that electron loses when it is deflected is not quantized. This results in a continuous spectrum (see section 3.2.1.1). This principle is also utilized in synchrotron facilities, where charged particles with high velocities are producing a brilliant continuous spectrum when being deflected in a magnetic field (see section 3.2.1.2).

3. Methods & Techniques

3.1. EDXRF (Energy Dispersive X-Ray Fluorescence)

The basic components of an EDXRF components are presented in Fig. 7. An X-ray source produces an X-ray spectrum composed of characteristic and continuous radiation (section 3.2.1.1). Optionally, this primary radiation can then be modified spectrally, e.g. filters, polarizer, monochromators etc., or in shape and size, e.g. focussing optics, mirror systems etc. . A fraction of this radiation reaches the sample where it can interact with the electrons and atoms of the sample material. As discussed in section 2.2 multiple types of interactions are possible. Some photons will be elastically or inelastically scattered, while others might be absorbed by bound electrons, leading to the emission of characteristic photons or Auger electrons. The radiation coming from the sample is detected (section 3.2.3), processed (section 3.2.3.3) and analysed (sections 4.3 & 4.4).

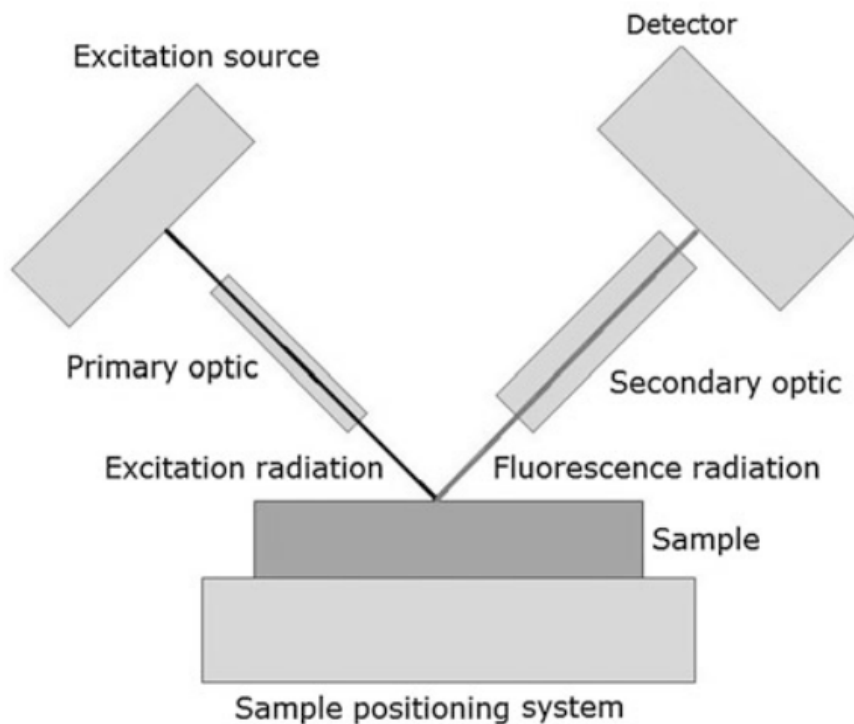


Figure 7: Schematic drawing of general principle of EDXRF instrument. Primary and secondary optics are optional. [6]

EDXRF has a variety of advantageous properties, making it an analytical technique that is suited for a wide range of different applications, such as the investigation of biological samples, cultural heritage or environmental analysis, but also materials research or industrial process control. It is a non-destructive technique, and can therefore be used for analysis of the composition of valuable items (e.g. cultural heritage), furthermore, this makes it perfectly suited for combination with other analytical methods [1]. Measurable concentrations range from ppm to percent and, depending on the experimental setup, detection of low to high Z elements is possible.

3.2. Components Of An EDXRF Spectrometer

3.2.1. X-Ray Sources

3.2.1.1. X-Ray Tubes

The most common radiation sources in X-ray fluorescence spectroscopy are X-ray tubes. The basic structure of an X-ray tube is shown in Fig. 8. It contains a spiral filament (usually made of W), which acts as a cathode, and an anode placed inside a vacuum housing. A heating current through the filament (0.1-1 mA) is causing electrons to gain enough energy to leave the cathode. Between cathode and anode a high voltage is applied (10-50 kV), which leads to the electrons being accelerated towards the anode. When the electrons hit the anode material they are decelerated, giving rise to the continuous bremsstrahlung spectrum (section 2.4). Additionally, a fraction of the electrons that impinge onto the atoms of the anode will excite them. The subsequent deexcitation of those atoms can then lead to the emission of characteristic x-rays (section 2.2.1). The arising spectrum is a superposition of those two types of radiation (Fig. 9).

X-Ray tubes have a very poor efficiency ($\sim 1\%$). The remaining power is converted into heat, which has to be removed by a cooling system. Depending on the power of the tube, air (low power), water or oil can be utilized as a cooling agent.

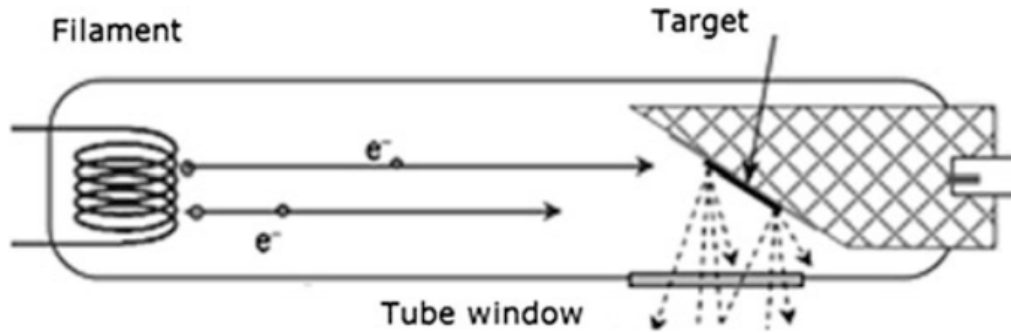


Figure 8: Operating principle of an X-ray tube. [6]

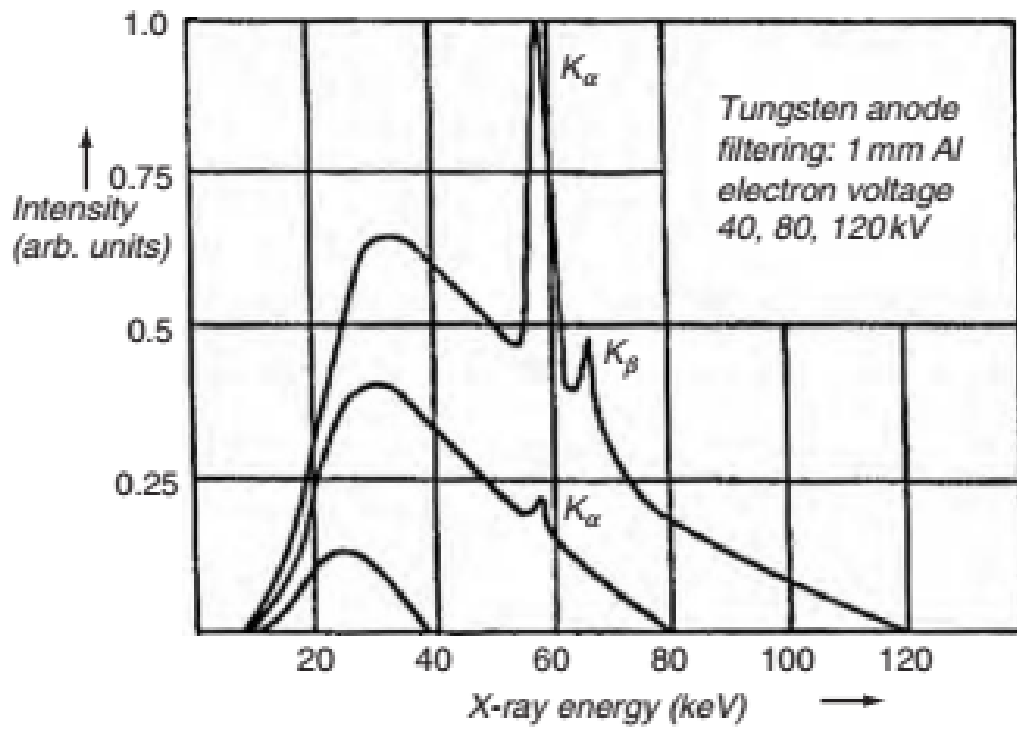


Figure 9: Tube spectrum of tube with tungsten anode (with 1mm Al filter) at different voltages, from [9]

3.2.1.2. Synchrotron Radiation

In synchrotron facilities, bunches of charged particles (electrons or protons) are

accelerated and injected into a storage ring and maintained at relativistic velocity. To keep them on a circular path, dipole magnets along the storage ring are utilized to deflect them (Lorentz force). When the particles are deflected, they emit continuous radiation (from infra-red to x-rays) in a small cone around their momentary direction of movement. This radiation has a high intensity, a high degree of collimation and linear polarization in the orbit plane, as well as a small source size, which is determined by the particle beam dimensions. As a result, synchrotron sources have an exceptionally high brilliance (Fig. 11). Depending on the application, the radiation will go through a number of components in order to spectrally modify and adjust shape, size and spatial properties of the beam before it reaches the experiment. In Figure 10, a schematic drawing of a synchrotron setup is shown. It generally consists of a linear accelerator and a booster ring, where the electron or positron bunches are accelerated before they are injected into the storage ring. Since the particles are losing energy in the form of radiation when they are deflected, high frequency cavities along the storage ring provide them with energy, while also keeping the bunches together by accelerating slower particles more than faster ones (in the direction of their movement). Additionally, multipole magnets are utilized to prevent the particle bunches from diverging in directions perpendicular to the storage ring.

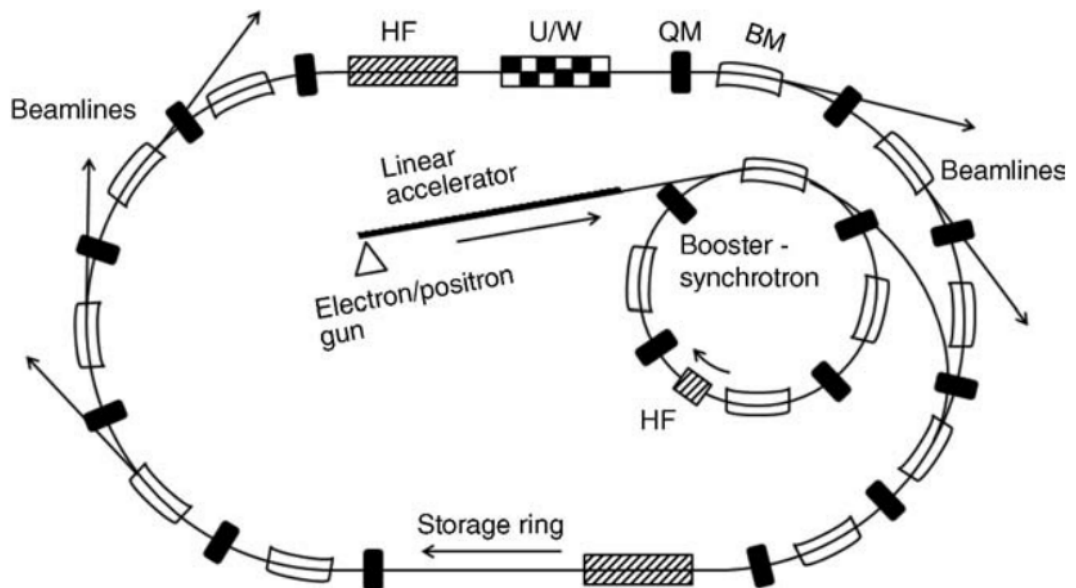


Figure 10: Schematic drawing of a synchrotron facility [7].

Radiation for experiments is extracted either at the bending magnets or by sophisticated insertion devices, so-called wiggler and undulators, that are positioned in the straight sections of the storage ring. These insertion devices are capable of producing even brighter radiation (Brightness $:= \frac{\text{photons}}{\text{s} \cdot \text{mm}^2 \cdot 0.1 \frac{\Delta E}{E}}$) that can be tailored as needed by changing the device parameters. As can be seen from Figure 11, the brilliance of radiation produced at synchrotron sources is several orders of magnitudes higher than for an X-ray tube source.

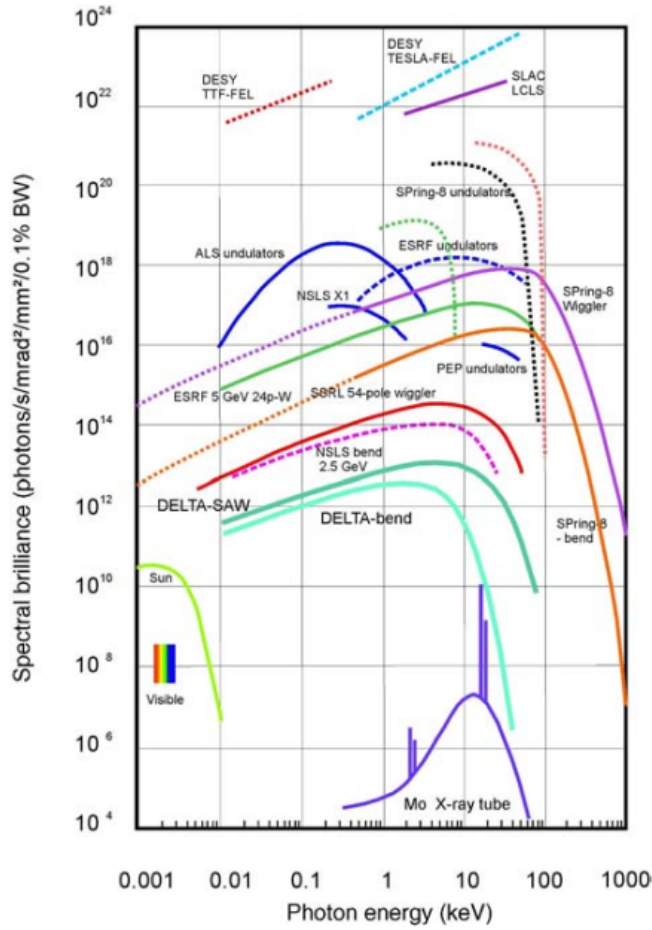


Figure 11: Comparison of the brilliance ($:= \frac{\text{photons}}{\text{s} \cdot \text{mm}^2 \cdot 0.1\% \text{BW}}$) of Mo X-ray tube source and different synchrotron sources [10].

Usually, a small bandwidth of the continuous spectrum is selected utilizing some kind of monochromator (section 3.2.2.2), in order to perform experiments with quasi-monochromatic radiation.

3.2.1.3. Radioactive Sources

Radioactive sources are materials that are naturally emitting X-ray radiation, as a product of a nuclear decay process. Although radioactive sources have the downside of the related safety issues when handling them, they can be practical for test measurements, as they do not need any power and are easy to handle.

3.2.2. X-Ray Optics

Optical elements should tailor spectral distribution to requirements of the experiment and reduce the beam size and increase the flux. For example, in μ XRF setups, polycapillary optics are essential to focus the incoming beam onto a small spot on sample, and in synchrotron sources, monochromators with tunable energy are utilized for optimal excitation of the elements of interest.

3.2.2.1. Spectral Modification Devices

- **Filters:** Filters can be used to attenuate parts of the primary spectrum, as the radiation will be absorbed depending on the energy. The resulting spectrum will be the product of the original spectrum with a filter function, which can be used to reduce the unwanted background. Another possible application is the insertion of a filter between sample and detector in order to attenuate high peaks in the spectrum, therefore also reducing any related artefacts that might overlap with regions of interest.
- **Polarizers:** By polarizing the outgoing tube radiation in the sample-detector axis, no radiation will be scattered in the direction sample to detector, therefore mainly fluorescence radiation originating from the sample can reach the detector. This will result in a significant background reduction.

3.2.2.2. Monochromators

Crystal Monochromators As discussed in section 2.2.7, when X-rays are diffracted on a single crystal lattice, for a given interplanar distance (depends on the used material) and angle only photons with wavelength λ (or multiples of λ) are constructively superimposed, so the reflected spectrum will consist of sharp peaks at the corresponding energies. Higher orders can be filtered, if they are present in the primary spectrum, resulting in a monochromatic spectrum. However, the monochromatic spectrum

will have a finite width, which determines the monochromator's energy resolution $\frac{\Delta E}{E}$. There are two factors contributing: Firstly, the incoming beam will not be perfectly parallel, therefore not all photons will hit the monochromator at exactly the same angle, resulting in a broadening of the spectrum. Secondly, the monochromator crystal will not be a perfect crystal, which will also result in a broader monochromatic peak.

So in order to tune the monochromator energy, one has to change the angle of the monochromator crystal. Changing the angle will also result in the outgoing beam changing direction depending on the adjusted energy. To solve this problem a two-reflection monochromator in a fixed-exit geometry is utilized (Fig. 12).

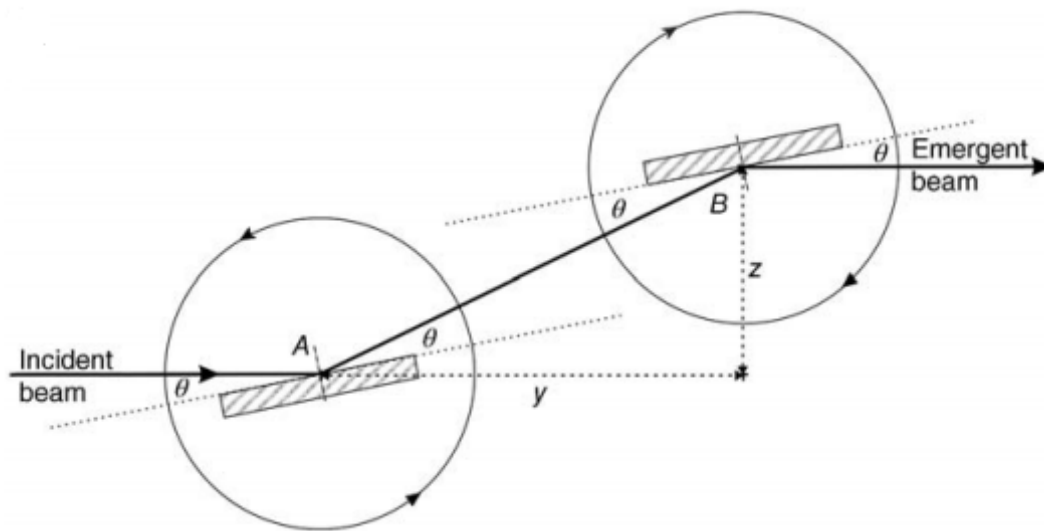


Figure 12: Double reflection monochromator geometry [7].

Multilayer Monochromators Multilayer monochromators consist of alternating layers of high and low Z materials, which results in a periodic structure. Just as for single crystals, incoming x-rays are diffracted according to Bragg's law. Since a lot less layers ($\sim 10-200$) are contributing to the diffraction process, compared to single crystals, the resulting spectrum will be a lot broader and the integrated area under the peak will be larger, meaning more photons will pass. In more technical terms this means that crystal monochromators have a higher reflectivity (peak height) and narrow energy resolution, while multilayer monochromators have a higher integral reflecting power (Fig. 13). This makes multilayer monochromators especially interesting for μ XRF, since high intensities are desired, while an extremely good energy resolution is not that critical.

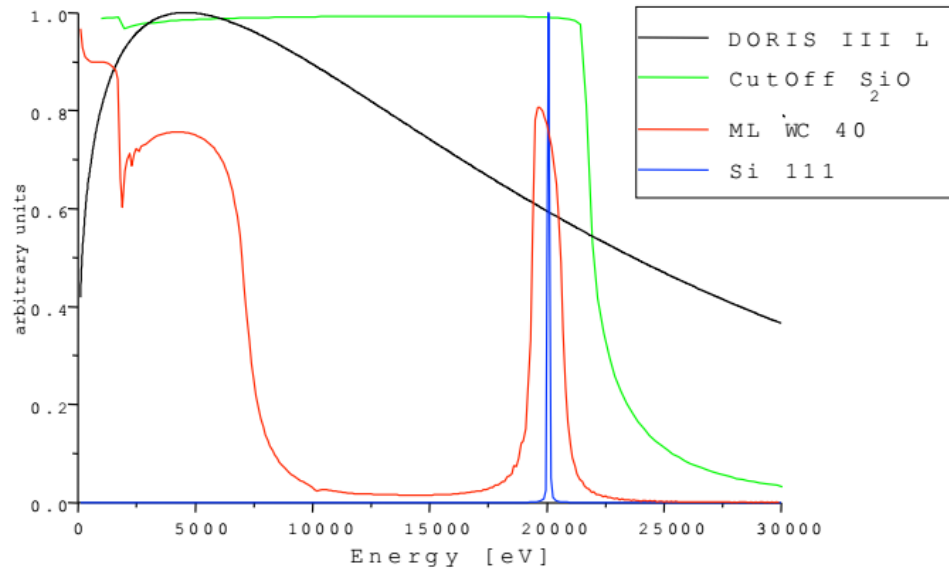


Figure 13: Comparison of monochromatic spectrum obtained by Si single crystal (blue line) and multilayer monochromator (red line) [8].

3.2.2.3. Poly-Capillary Optics

The fact that X-rays can be total reflected on solid materials (section 2.2.6) is utilized in a variety of optical devices. One of them that has a significant importance for μ XRF is the polycapillary optic. Figure 14 illustrates how X-rays can be propagated in capillaries by multiple total reflections inside the capillary. Only radiation with an incidence angle smaller than the critical angle (which depends on the X-ray energy) can be captured by the capillary. Compared to a pin hole with the same cross-section as the capillary, an intensity gain is achieved by the increased capture angle compared to the pin hole.

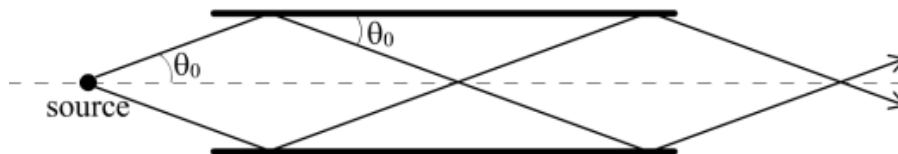


Figure 14: X-rays propagating through single capillary [8].

A vast improvement to this simple design is the combination of large bundles of

capillaries in special geometries, in the form of polycapillary optics.

They exist as full and half lenses, as shown in Figure 15. Polycapillary optics can have intensity gains up to factors > 100 , depending on the energy range, and focal spot-sizes are in the range of several ten μm (see Fig. 34).

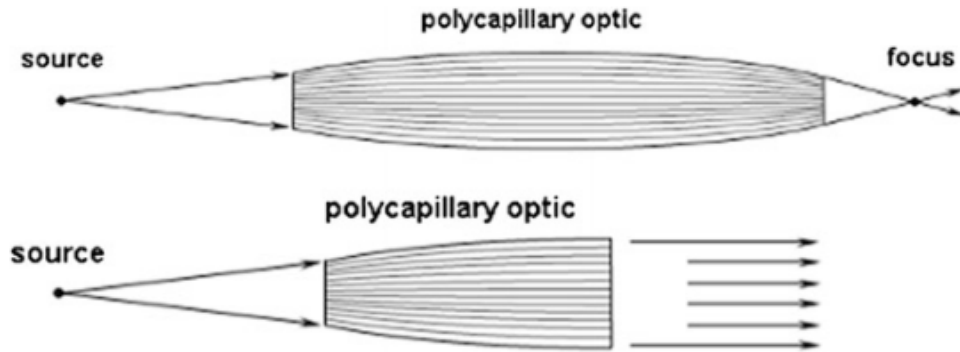


Figure 15: Polycapillary optics as full and half lens [6].

3.2.3. Semi-Conductor Detectors

A semiconductor is a material that has a small but finite band gap between valence and conduction band. That means that it is an insulator at 0K, but electrons can jump to the conduction band if they are excited, e.g. if they are thermally excited at temperatures above 0K. A semiconductor detector consists of a cooled semiconductor crystal (Si or Ge) that has a high voltage applied over the length of the crystal. When X-ray photons propagate through the crystal they create electron-hole pairs, with the number of pairs being proportional to the X-ray energy. The high voltage then sucks them away and the resulting electrical pulse, which has an amplitude proportional to the photon energy, is registered, amplified and shaped, and sorted by amplitude by a multi-channel analyzer (MCA). The resulting distribution is an X-ray spectrum.

At room temperature the thermal energy would result in electrons being able to jump to the conduction band, leading to a thermal noise signal. Therefore most detectors have to be cooled, depending on the type of detector, either using liquid nitrogen or Peltier cooling. Furthermore, to prevent contamination, the detector crystal is operated in vacuum. Thus, a suitable entrance window to the detector, that has to be sturdy enough to withstand atmospheric pressure, while not absorbing too much radiation or adding peaks to the spectrum, is needed. Most commonly, Beryllium is the material of choice for this purpose.

3.2.3.1. Si(Li) detector

A Si(Li) or lithium drift detector crystal is produced by depositing a layer of Li on one side of a p-doped silicon crystal. By heating it up (300 - 600 °C) the Li atoms (which act as n-doping) can diffuse into the Si crystal whereas the Li concentration is decreasing with increasing distance to the Li layer. So the doping changes continually from n-doped (at the Li layer end of the crystal) to p-doped. Since the Li atoms are not incorporated into the Si lattice but are sitting on interstitial sites, they are relatively mobile. At 100 °C - 200 °C a reverse-bias is applied, forcing the Li atoms to drift into the p zone. The result is an intrinsically conducting region between n- and p-zone, where there is a balance between Li-donor and acceptor atoms. The detector crystal has a so-called dead-layer, where electron-hole pairs are not fully collected, hence photons are measured with a lower pulse height, leading to so-called low energy tailing, i.e. peaks have a tailing on the low energy side.

Active areas of Si(Li) detectors range from 10 to 80 mm². They are cooled with liquid nitrogen, not only to reduce the thermal noise, but also to prevent further diffusion of the Li atoms.

3.2.3.2. SDD (Silicon drift detector)

The core part of a SDD detector is a silicon wafer of high purity, with several millimeters in diameter and a few hundred micrometers thickness. On the front side of the crystal (direction of the incoming X-rays), there is a thin p^+ -type layer, and on the opposite side there is a series of concentric p^+ -type rings with a small anode ring in the center (Fig. 16). While the front layer is switched as a cathode, there is an additional electrical field applied parallel to the wafer, with increasingly negative voltage from inside to outside rings, guiding electrons to the anode ring in the center.

SDDs provide high countrates and good spectral resolution (< 130 eV for Mn-K α) without the need of liquid nitrogen cooling. Since the leakage current is low, less cooling is needed for SDD detectors (~ -20 to -40 °C), hence a simple Peltier cooler is sufficient.

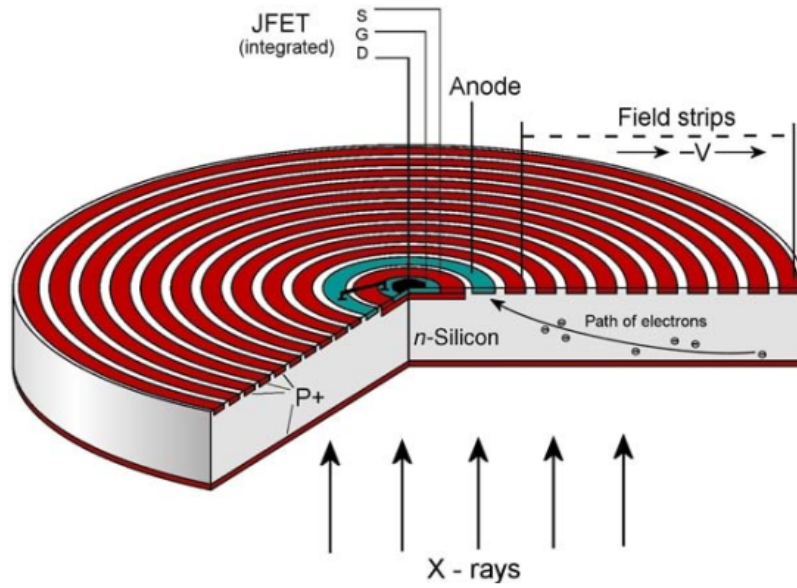


Figure 16: Cross-section of a silicon drift detector [7].

3.2.3.3. Signal processing

Each current pulse that is coming from the detector, following the impact of an x-ray photon, is amplified, shaped and sorted according to its amplitude and registered by a multichannel analyzer (MCA) which matches it to a channel according to its energy, where each channel represents an energy region E_n to $E_n + \Delta E$ (with n being the channel number). For each incoming pulse the count number of the according channel is increased by one. The processing of a pulse takes a certain amount of time. If a second pulse reaches the pulse processor during this time, none of the two signals can be evaluated viably. To prevent the continuing processing of such signals, a second, faster channel registers such events, and they get rejected by the pile-up rejector. During such an occurrence no viable information is reaching the MCA, this time interval is lost time for the measurement. Therefore it is referred to as dead time.

3.2.3.4. Detector artefacts

Sum Peaks When two photons reach the detector crystal within a time interval shorter than the fast channel of the pile-up-rejector, the pile-up rejector will not be able to distinguish them as two events, hence they will be registered as a single event with the sum of the single photon energies. For energy regions in the spectrum with particular high countrate (e.g. the Ca peaks for bone samples), this can lead to sum peaks, where the corresponding energy is the sum of other peaks in the spectrum.

Escape peaks If a photon strikes the detector crystal near its edge, an X-ray with the characteristic energy of the detector material (1.76 keV in the case of Si) might escape the detector, therefore shifting the detected energy, resulting in so-called escape peaks. If this happens almost at the same time as another photon strikes the detector, and the two events are therefore registered as one, it is even possible to observe escape peaks of sum peaks (sum escape peaks). Since the probability of this happening is quite low, this is only observable for very high peaks.

3.3. μ XRF

3.3.1. μ XRF

In μ XRF, the incoming beam is focussed onto a small spot of the sample (of the order of several ten μm). The sample is excited only locally, therefore the radiation that is detected is giving information about the elemental composition of only this small area. By moving the sample though the beam focus in steps while measuring spectra at each step, it is possible to create two dimensional elemental maps of the sample. The focussing of the incoming beam is most commonly achieved by introducing a focussing polycapillary lens (section 3.2.2.3) between tube and sample.

When X-ray radiation enters and passes through matter, it is attenuated according to the Lambert-Beer law. The same holds true for the fluorescence radiation leaving the sample in the direction of the detector. This means that the detected radiation is only coming from a certain depth region below the sample surface. Consequently, this information depth is depending on the parameters as stated by the Lambert-Beer law, i.e. the energy of the exciting radiation as well as the fluorescence radiation, the density and the chemical composition of the irradiated sample.

This means, especially for higher Z elements, that the measured photons are not originating only from the sample surface but also from deeper layers. Furthermore, since

the focussed beam hits the sample in a 45° angle, photons coming from deeper layers are not coming from the region directly below the irradiated surface region, but from adjacent regions. Therefore, the spatial resolution will be distorted to some extent. These issues can be resolved by confocal μ XRF.

3.3.2. Confocal μ XRF

In confocal μ XRF-spectroscopy a second polycapillary optics is introduced to the system, namely between sample and detector (Fig. 17). It is positioned in such a way that its entry focus coincides with the exit focus of the first polycapillary optics. Consequently, only X-rays coming from this defined volume of the intersection of both polycapillary beam paths are reaching the detector. Therefore, the information depth is limited by the confocal volume size, which improves the surface sensitivity of this method compared to non-confocal μ XRF. Furthermore, this opens up the possibility of depth scans or even 3D scans of a samples structure. As an example, Figure 18 shows the results of a 3D scan using the ATI confocal μ XRF spectrometer [3].

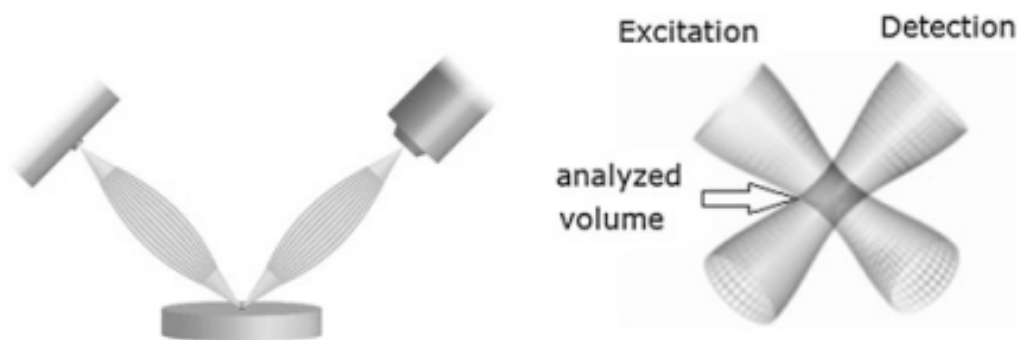


Figure 17: Confocal geometry [6].

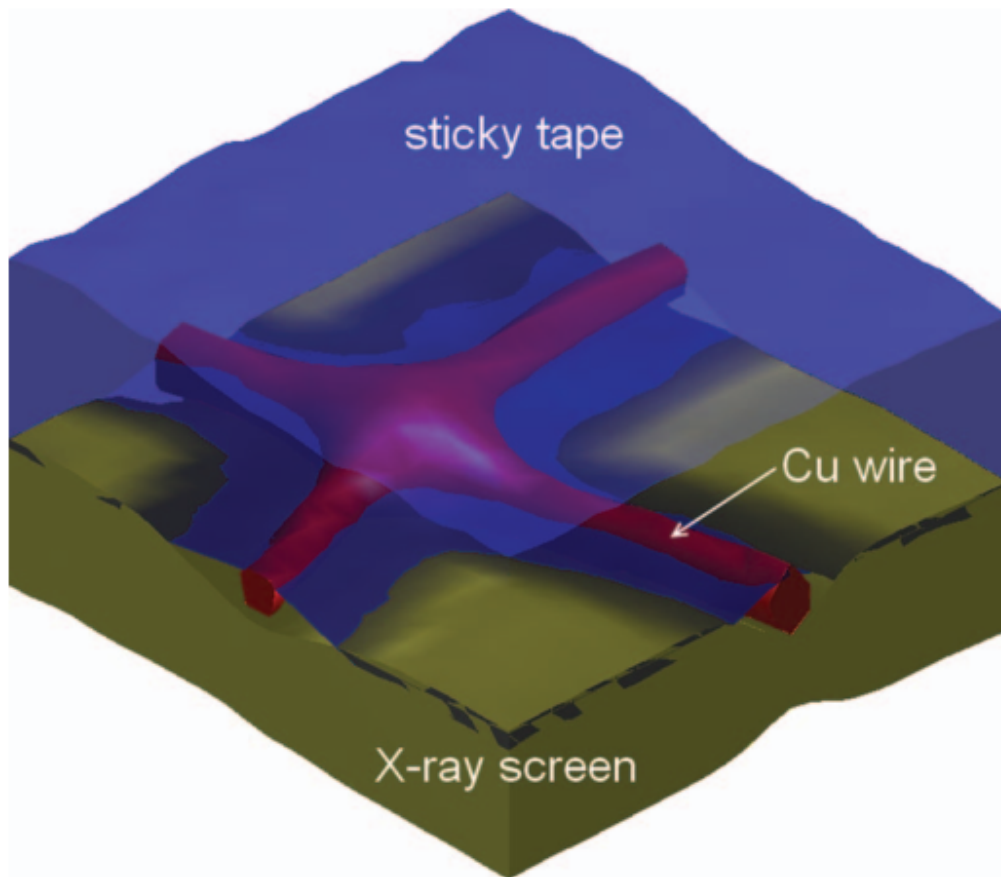


Figure 18: 3D elemental mapping of Cu wire cross (red) fixed to Gd X-ray screen (yellow) using sticky tape (transparent blue), from [3].

4. Experimental Setup & Data Analysis

4.1. Components Of ATI spectrometer

- X-Ray Tube: 20W low power tube with Rh anode (Oxford Apogee), cooled by a fan / X-ray generator XR-505-50-01-OX (Matsusada Precision Inc.). An interlock circuit prevents tube operation without a cover.
- Detector:
 - Laboratory: 30mm² Si(Li) detector with liquid nitrogen cooling with a Saturn MCA (XIA). An ultrathin window is utilized to minimize the absorption of low Z element fluorescence radiation. The detector is mounted on a sled to adjust the detector finger position to the currently employed method.
 - ELETTRA: SDD detector (Ketek) with 25 μm^2 Beryllium window, 80 mm² active area and an energy resolution of 145 eV @ 5900 eV and Ketek MCA.
- Polycapillary optics: Full-lens (XOS) with nominal spot size of 32 μm for Mo-K α in excitation channel. Half-lens (XOS) in detection channel for confocal measuring. Both are mounted on identical XYZ piezo positioner stacks (Attocube).
- Microscope system: Camera (Marlin F-201C, Allied Vision Technologies) attached to objective (Plan Apo infinity corrected with large working distance, Mitutoyo)
- Light-source: Cold-light source (Highlight 3100, Olympus)
- Sample stage positioning: Sample is mounted via magnetic base on motorized XYZ-stage (25 mm travel range)
- Vacuum chamber: The whole setup is situated in a cylindric vacuum chamber (~ 4 mbar). The compact design of the chamber makes the spectrometer portable, with all components being easily removable.
- Software: The ATI μXRF spectrometer is controlled using the in-house software package “microScan” [2]

4.2. Adjustment procedure

This chapter will give a rough outline of the adjustment procedure in the lab and the improvements made to it. For a more detailed description refer to the adjustment manual.

First, the full-lens in the excitation channel has to be adjusted to the tube's focal spot to get as much of the primary radiation through the polycapillary as possible. The next step is determining the exit focus of the polycapillary and then adjusting the microscope focus to coincide with it. Finally, to achieve the confocal setup the polycapillary half-lens is mounted between sample and detector, and then is positioned such that its entry focus overlaps with the full-lens exit focus.

4.2.1. Adjusting Polycapillary Full-Lens

After mounting the polycapillary full-lens in the excitation channel, its position has to be adjusted to the tube's anode focal spot. This is achieved by scanning the polycapillary in the plane perpendicular to the beam axis while measuring on any sample (with known X-ray lines). A first, rough scan with larger step-size ($\sim 200 \mu\text{m}$) will yield the approximate position. Then, the position is optimized with smaller scans to get maximum counts. The distance between polycapillary and tube can be varied quite a bit without affecting the detected counts significantly. This can be used to modulate the position of the half-lens in confocal mode in order to align it with the detector finger.

4.2.2. Adjusting The Microscope Focus

The μXRF spectrometer utilizes a microscope to enable the operator to reliably position the sample surface at the focus of polycapillary optics. The microscope has a very small depth of focus, i.e. only objects that are very close to the microscope focus appear sharp. Once the focal distance of the polycapillary has been determined, the microscope focus is set to this position and can thereafter be used to position any sample at the focus of the optics, simply by moving it to the microscope focus.

At the focal distance the beam's size will be at a minimum. Thus, determining the beam size for varying distances between polycapillary and sample and then looking for the distance where the beamsizes is minimal will yield the focal distance. To define the beamsizes a sharp edge or wire is utilized. During this project a Cu wire ($d_{\text{wire}} = 10 \mu\text{m}$) glued to a Gd-screen was used for all adjustment procedures. The Cu intensities of a linescan across the Cu-wire will yield a Gauss curve. The beam diameter is then given by

$$d_{\text{beam}} = \sqrt{FWHM^2 - d_{\text{wire}}^2} \quad (17)$$

where $FWHM$ is the full width at half maximum of the measured curve. It can be

extracted by fitting each measured line-scan with a Gauss curve. To make this fitting process more convenient, a MATLAB script that automatically fits all curves and plots the resulting *FWHM* values against the polycapillary-sample distance was created. Figure 19 shows the resulting plot from a previous adjustment procedure. Beside the *FWHM*, the gross Cu-K α counts are also plotted. They will show a maximum at the focus position.

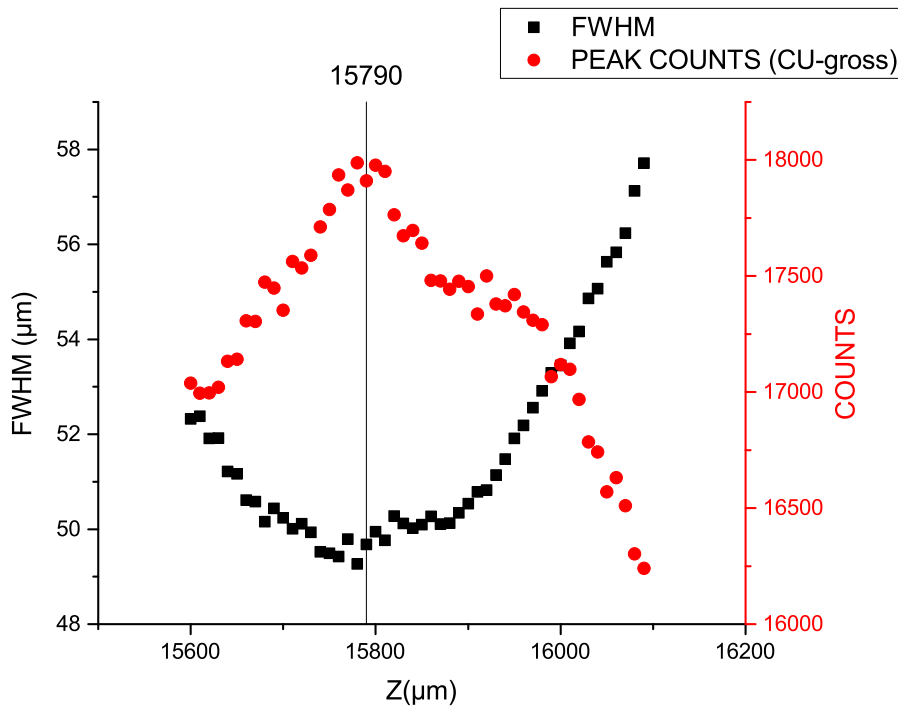


Figure 19: *FWHM and Cu-K α gross counts for linescans across 10 μm Cu wire, as function of the distance of polycapillary and sample.*

Finally, after the sample staged is moved to the determined position where the focussed beam hits the sample surface, the microscope is focussed onto this position.

4.2.3. Adjusting Polycapillary Half-lens

After moving back the detector finger, the half-lens can be installed onto the piezo-positioner stack between sample and detector. The adjustment procedure is similar to the first polycapillary. First, a large scan with larger step-size (~ 100) in the plane

perpendicular to the beam path is performed. If a spectrum can be measured at any position, the position is then optimized by alternating scans in X,Y and Z until the maximum countrate is reached.

4.2.4. Determining The Size The Confocal Volume

As a final step, the dimensions of the confocal volume can be determined. There are several methods to achieve this. The one that was generally used in the course of this thesis consisted of performing cross section scans of a free-standing horizontal (XZ-plane) and a vertical (YZ-plane) 10 μm Cu wire. After fitting the raw data, the column and line containing the maximum for each scan were extracted and Gauss fitted to obtain the confocal volume dimensions (as can be seen in Fig. 33 and 44).

4.3. Data Analysis

The area beneath a characteristic peak in an X-ray spectrum (without the underlying background) is proportional to the amount of that element that is present in the sample. Of course the total counts of an element depend on several other factors as well. The exciting spectrum, the whole geometry of the experiment, the composition of the sample, the detector as well as the energy of the x-ray line itself. So while it is a difficult matter to quantify the amount of a certain element in the sample, as long as all those factors are the same or at least comparable for different measurement positions on a sample, the comparative amounts of an element at different points on the sample can be determined by simply calculating the area beneath the corresponding peaks.

A measured spectrum will consist of the characteristic peaks on top of a continuous background, which is mostly a consequence of the continuous part of the tube-spectrum being diffracted by the sample. To determine the area under a peak, the spectrum is fitted. In general this fit consists of a background function and the fluorescence peaks sitting on top. Additionally, detector artefacts might be present in the spectrum and should be taken into account. Depending on the software, the user can chose from different background models and set a number of parameters. When choosing a fitting model, the goal is to achieve the best possible fit, without the background function cutting into the peaks, peaks getting over- or underestimated, and without element peaks being fitted that are not actually present in the spectrum.

Depending on the type of sample, achieving a good fit can be a challenging task. The AXIL [11] software package has been producing good results for a range of different samples. On the downside, AXIL inconveniently only runs on DOS, therefore the GUI

is outdated and clunky, and fitting a large number of spectra can be time consuming. A possible alternative would be the widely used PyMca software package [12], which has a more modern GUI and a number of other practical features, e.g. multiprocessing batch fitting and the output of individual peak fit results. To get an idea of the viability of using PyMca for fitting bone sample data, all sample measurements in this thesis were fitted with AXIL as well as with PyMca. It was not the goal of this work to quantitatively compare the fitting results of the two software packages, but rather to find out if PyMca can in general be used for such types of samples. Overall, the resulting elemental maps were quite similar in general, with a few exception where one of the two programs was performing better for some elements or some points of a scan. One should note, however, that almost all results presented in this thesis were acquired using a monochromatized synchrotron source, therefore the spectral background was low, which simplified the fitting task. No extensive testing of fitting spectra acquired using an X-ray tube source with PyMca was carried out. Still, it is recommended to use both methods parallel and choose the best results on a case to case basis. Hence, all elemental maps presented in this thesis will be tagged with (A) if they were fitted using AXIL or (P) if they were fitted using PyMca.

4.4. Data Visualization with LP-map

The output of the finished fitting procedure consists of text files corresponding to each measured spectrum, which contain the counts of each element included in the fitting model. This output data is usually plotted in the form of 2D elemental maps, where the color of each pixel represents the measured intensity. For AXIL fits, for each fitted ".SPE" file, the fitting results are outputted into an ".ASR" file with the same name. For PyMca fits, the fit results of the whole batch are written into a single ".DAT" file, which is automatically saved into a subfolder of the chosen output directory called "IMAGES/".

As a part of this thesis, the software "LP-map" was created, to automatically create elemental heatmaps from the output files of the fitting process, both for AXIL and PyMca (see 4.4.1). The program offers a number of features aiming to make the assessment of the fitting results easier, and the data analysis in general more convenient. The utilization of tabs allow for several maps to be opened at the same time. Additionally, it is possible to open and calibrate spectra in the form of ".SPE" files (see 4.4.2), including a number of features: e.g. KLM-markers, comparison of several spectra, setting ROIs and creating ROI maps. "LP-map" is also designed to allow the user to conveniently

create customizable plots for presentations and publications.

“LP-map” was coded in Python 2.7, the GUI was created using the PyQt4 library and for plotting the matplotlib library was used.

4.4.1. Plotting Elemental Maps

The main function of “LP-map” is the automatic creation of elemental maps of fitted 2D scans. Either “.ASR” files created by AXIL or a “.dat” file created by PYMCA are possible as input. To load a map, click “File”, then choose either “Open AXIL Map” or “Open PyMca Map” and choose a valid folder. For AXIL maps, the folder needs to contain the corresponding “.ASR” files and optionally “.DMP” files, containing the spectrum data. For PyMca fits, the chosen folder needs to contain a “.dat” file and optionally “.fit” files, containing spectrum data. Since real- and livetime data is not included in the PyMca output, LP-map will also try to find “.SPE” files in the selected folder to extract this information as well as the scan dimensions.

After choosing a valid scan folder, the scan parameters dialog (Fig. 20) will pop up. Here, the user has to enter a tab name, set the scan starting point and direction and chose between real- or livetime. If realtime is selected, the count rates at all points for every element will be multiplied by $\frac{\text{realtime}}{\text{livetime}}$ (dead time correction). Additionally, it is possible to modify the aspect ratio of the elemental map pixels, in case of different step sizes in X and Y direction. LP-map will try to extract the scan dimensions (number of X and Y Pixels) from “.ASR” or “.SPE” files in the scan folder, if unavailable, the dimensions have to be entered manually.

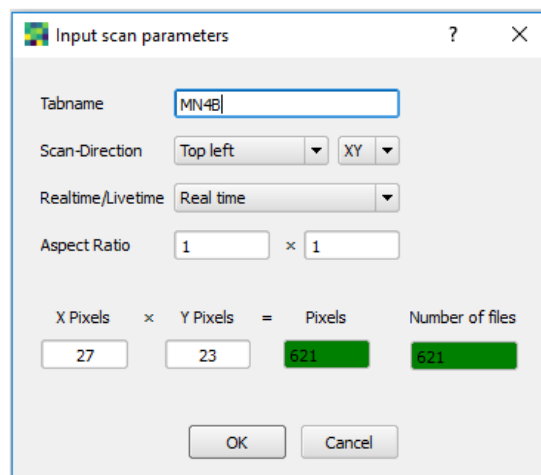


Figure 20: “Input scan parameters” dialog window

Once the parameters are accepted, the elemental maps be loaded (Figure 22). On the right side of the windows, the three tabs “Colormap”, “MapMatrix” and “Info” are used to navigate the software (Fig. 21).

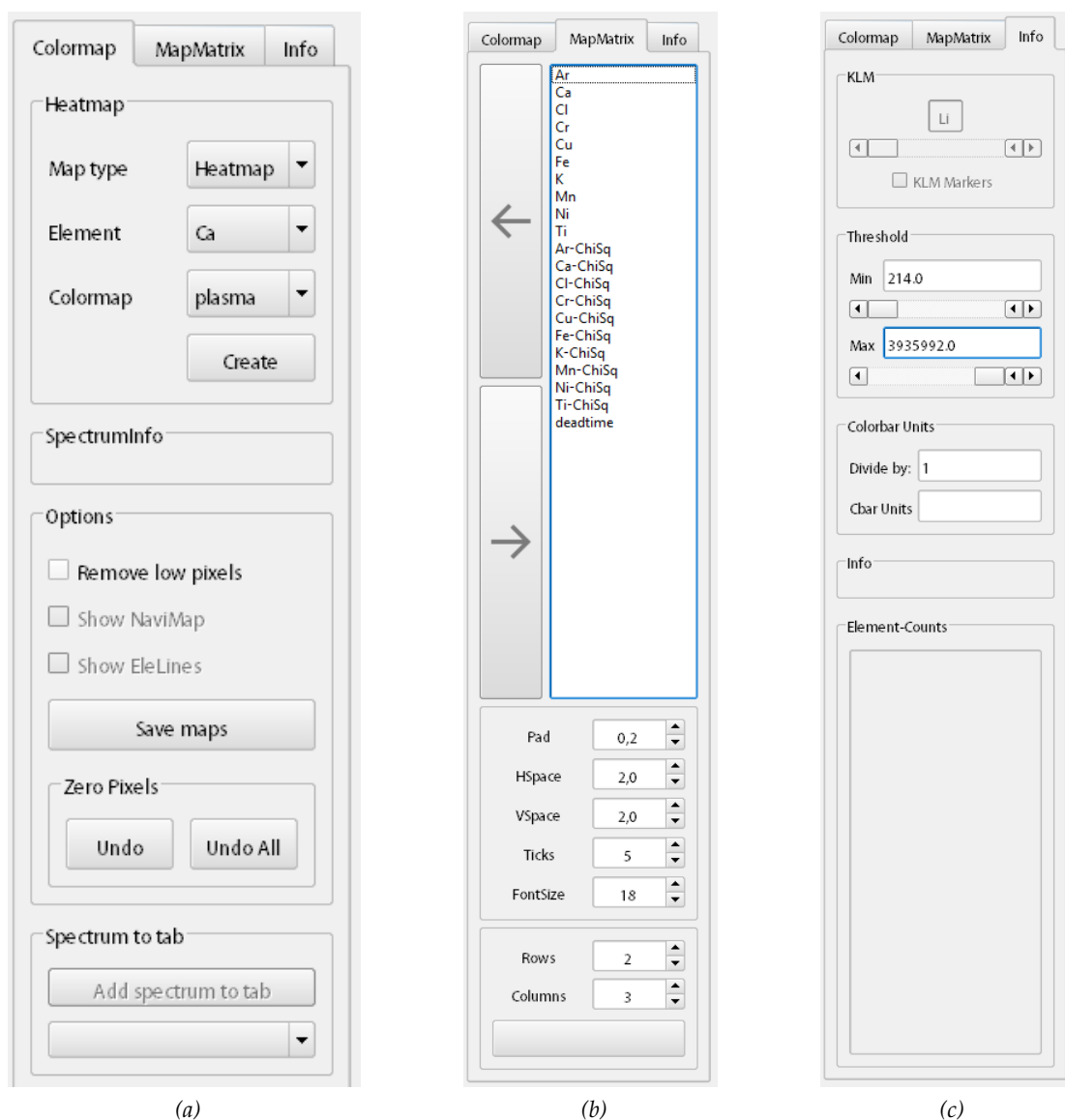


Figure 21: Zoomed in screenshot of the three navigation tabs “Colormap” (a), “MapMatrix” (b) and “Info” (c).

4.4.1.1. Colormap Tab In the “Heatmap” Box the user can switch map types between the normal “Heatmap” mode and “RGB-Map” mode, where up to 3 different

elements can be plotted in one elemental map, with the content of each element being represented in shades of either red, green or blue. In “Heatmap” mode, the user can choose the currently viewed element and the utilized colormap. To switch between the two modes or to confirm changes to the RGB-map, the “Create” button is clicked. Activating the “Remove low pixels” option, will set all pixels for all elements to zero, where $peakarea < 3 \times stdev$ (see AXIL manual [11]). Furthermore, pixels can be manually set to zero by holding down “CTRL” and the left mouse button while moving over any pixel. Such manual changes to the maps can be undone, by clicking “Undo” or “Undo All” in “Options → Zero Pixels”. The former will only revert changes to the currently viewed map, while the latter will revert changes to any map of that particular scan. Pressing “Save map” will automatically create a new subfolder “maps/”, where all loaded elemental maps will be saved as “.PNG” images and as “.TXT” files. Any changes made to the maps, i.e. by “Remove low pixels”, manually zeroing pixels or thresholding, (ch. 4.4.1.3) will still be applied in the saved maps.

If there are “.DMP” (AXIL fits) or “.FIT” (PyMca fits) files in the scan folder, heatmaps will be clickable. By clicking on a pixel, the corresponding spectrum, including fit results, can be viewed. Activating the “Show NaviMap” checkbox in the “Options” box will add a small version of the currently selected elemental map to the top of the spectrum plot. The NaviMap can be moved to the left or right by clicking on it with the left or right mouse button. The current position is marked on the NaviMap by a grey pixel. Using the arrow keys, it is possible to change the current position and move around the map. Activating the “Show EleLines” option, will either add markers showing the positions of all fitted elements to the spectrum plot (for AXIL fits) or add the actual fit curves for all fitted elements to the plot (for PyMca fits). The visibility of all lines in the spectrum plot can be toggled by left-clicking on the corresponding line in the plot legend. To toggle the total fit (plotted as green area), right-click on any line in the legend (but not on the fit line itself). Finally, “KLM Markers” can be activated or deactivated using the shortcut “K” or in the “Info” tab. To cycle through the currently viewed element marker, use “CTRL” + “Left/Right” arrow keys. With the shortcut “CTRL” + “Up/Down” arrow keys, sum and escape peak positions of the currently selected element are marked. If there are any open spectrum tabs (ref!), the currently viewed spectrum can be transferred to any open spectrum tabs, by choosing the desired tab and then clicking on “Add spectrum to tab”. In order to return to the heatmap view, one needs to click “Create” in the “Heatmap” box.

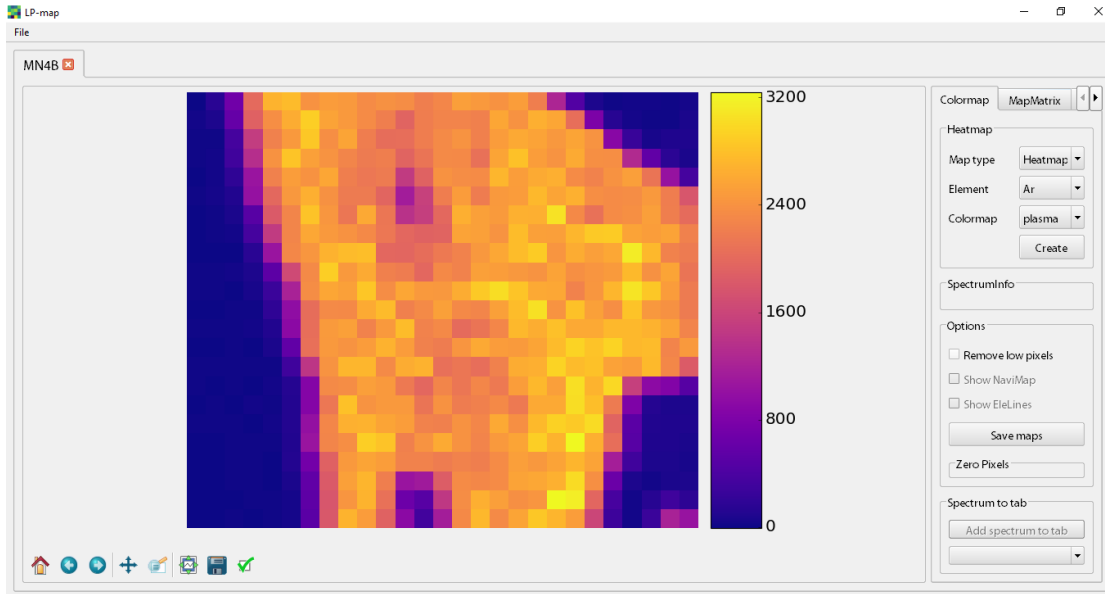


Figure 22: Heatmap Tab of the LP-map software

4.4.1.2. MapMatrix Tab For presentation purposes, the “MapMatrix” feature enables the user to create a labeled grid of available maps, similar to the old “MatrixMapJob” software [2] (Fig. 23). To create a map matrix, one needs to first set the number of rows and columns of the grid, then click on the “Create” button below to create the matrix. To add elemental maps to the matrix, the element is selected in the list, then pressing the “Add” button will add it to the matrix. By left-clicking on a map in the grid, it is highlighted by a red border, pressing “Remove” will remove the highlighted map from the matrix. Changing the values of “Pad”, “HSpace” and “VSpace” will change the spacings of the map matrix. The “Ticks” value changes the number of ticks on the colorbar and “FontSize” changes the font size of the title as well as the colorbar descriptions. Any changes to these parameters will also apply to the single colormap mode.

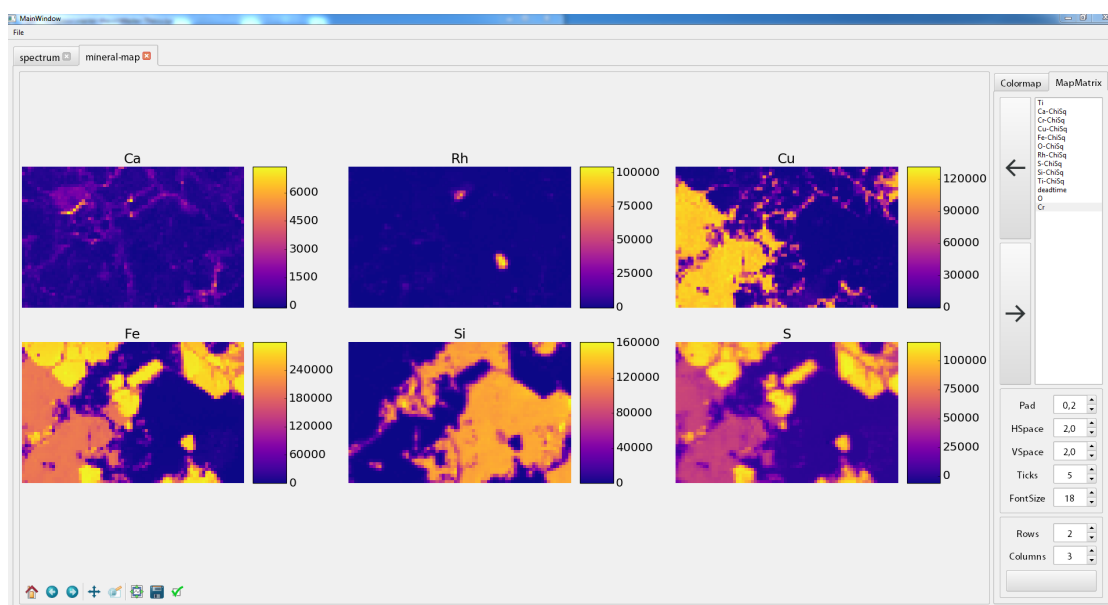


Figure 23: MapMatrix in LP-map software

4.4.1.3. Info Tab The “Info” tab contains the previously discussed “KLM-markers”. Moving the sliders in the “Threshold” box will set the minimum and maximum values for the currently selected elemental map. Values lying outside of this range are set to zero. In the “Colorbar Units” box, a positive number can be entered, by which all maps will be divided and a unit description for the colorbars can be applied. These changes will be visible after pressing “Create”, either in the “Colormap” or “MapMatrix” tab.

4.4.2. Plotting Spectra

Apart from creating elemental maps, LP-map is also capable of plotting spectra from raw “.SPE” data. Clicking “File” → “Add Spectrum Tab” will open up a new canvas for spectrum plotting. Clicking “Add Spe” will open up a file browser, prompting the user to select a “.SPE” file to plot. After adding a spectrum to the plot, it needs to be energy calibrated. This is achieved by clicking on a known peak, entering the corresponding energy in the “Calibration” box, and clicking “Add”. With “Del”, “Load” and “Save”, calibration points can be deleted, loaded and saved. Several spectra can be added to the same plot, while each can be calibrated separately. In the “Info” tab, to help identify elements, KLM markers can be activated. The “Timescaling” option scales all plotted spectra to the spectrum with the highest live time, i.e. each spectrum is multiplied by the maximum live time divided by its own live time.

In the ROI tab, ROIs can be created and labeled. A set of ROI's can be loaded or saved from/to ".cal" text files. Clicking the "Create ROI map" button will prompt the user to chose a scan, then a heatmap tab will be created with ROI heatmaps for all currently set ROIs. Figure 24 shows a plotted spectrum with labeled ROIs.

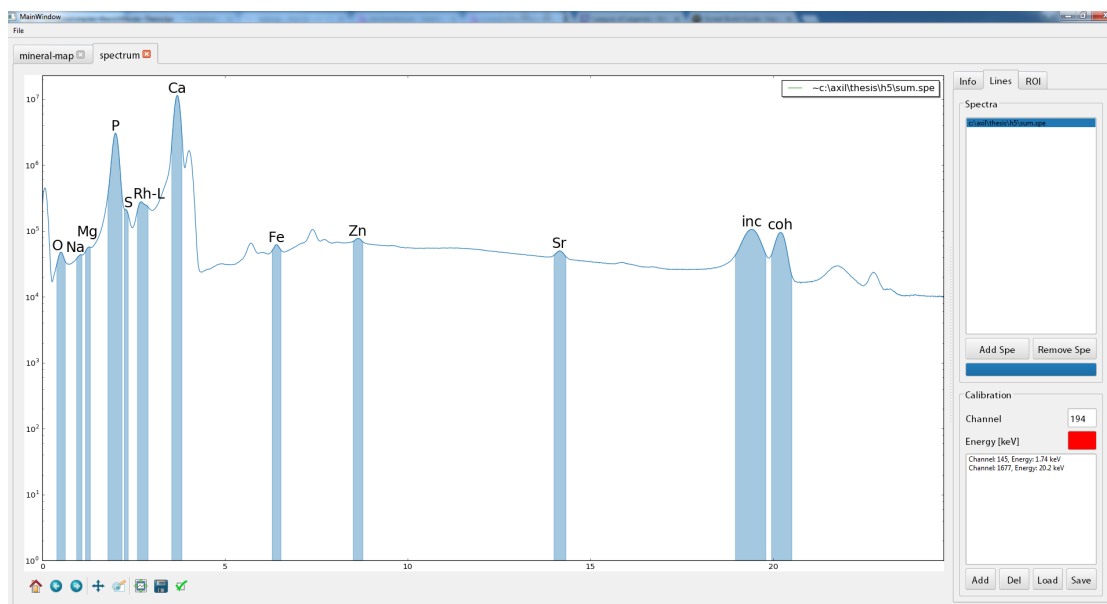


Figure 24: SpectrumTab in LP-map software

The toolbar below every plot can be used to pan or zoom, save the current plot as an image, or change plot parameters such as axis properties, line or marker styles and legend labeling.

5. Implementation Of The ATI μ XRF Spectrometer At The ELETTRA Synchrotron

The main goal of this thesis was to prepare ATI's μ XRF spectrometer for measuring at the XRF beamline of the synchrotron facility ELETTRA in Basovizza, Italy. In the following chapters, the preparations leading up to the experiments as well as the adjustment procedure on site will be discussed. Some chosen results will be presented and compared a previous measurement in the lab.

5.1. Beamline specifications

Table 1 shows the specifications of the XRF beamline at ELETTRA. The ELETTRA storage ring operates in top-up mode (310 mA at 2.0 GeV or 160 mA at 2.4 GeV). The light source is a bending magnet and the available energy range is 3.7 - 14 keV. Users can chose between single crystal (Si(111)) and multilayer (RuB₄C, NiC Coating) monochromators, though the latter are not yet approved for standard operation. Figure 25 displays the layout of the beamline. At the end of the beamline an UHVC end station (IAEA project [13]) is situated. The μ XRF spectrometer was installed directly downstream after this end station, the beam size upon exiting the UHVC chamber was $\sim 300 \times 200 \mu\text{m}^2$. In figure 26 the complete experimental setup is illustrated schematically.

Light Source	Bending Magnet
Energy Range	3.7 - 14 keV
Monochromators	Si(111), InSb, Multilayers (RuB ₄ C, NiC Coating)
Flux (Si(111) single crystal)	$1 \cdot 10^{10} \text{ ph/s @ 5 keV (2 GeV) or @ 10 keV (2.4 GeV)}$
Flux (RuB ₄ C multilayer)	$\sim 3 \cdot 10^{11} \text{ ph/s}$
Beam Size (after UHVC endstation)	$300 \times 200 \mu\text{m}^2$
Beam Exit Height (after UHVC endstation)	1425 mm
Beam Angle to horizontal plane	0.5°
Beam divergence	0.15 mrad

Table 1: Beamline specifications [14]

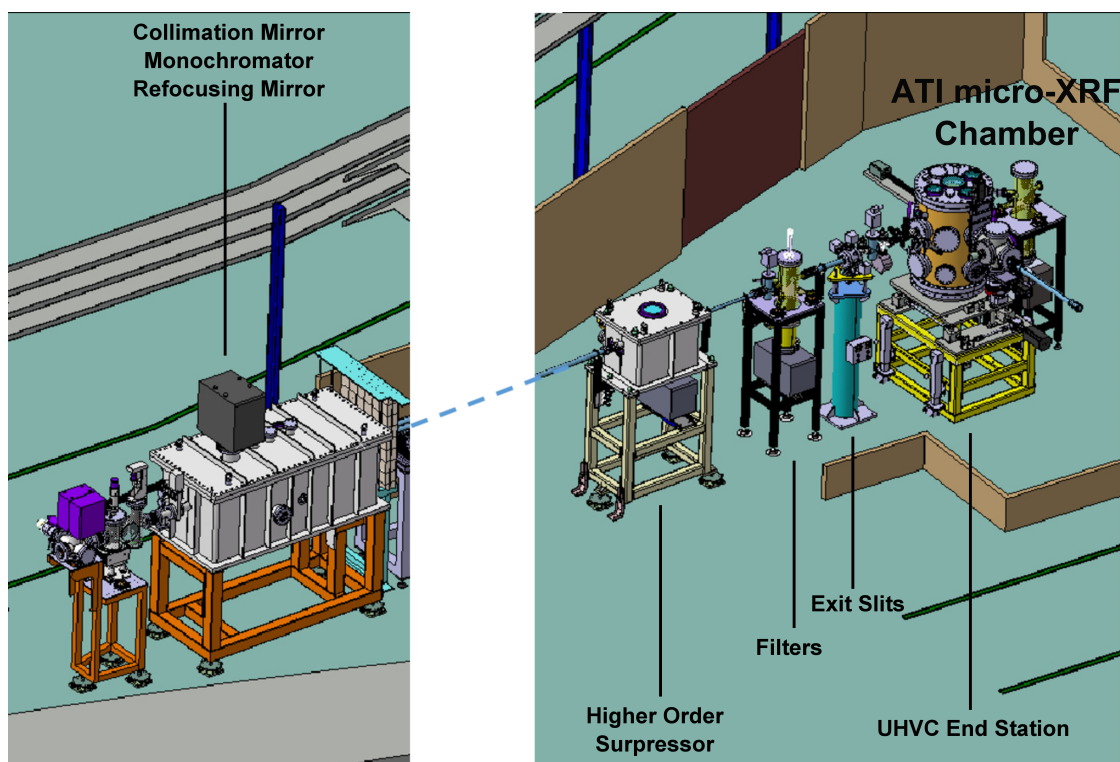


Figure 25: ELETTRA XRF beamline layout, including ATI μ XRF chamber (kindly provided by ELETTRA).

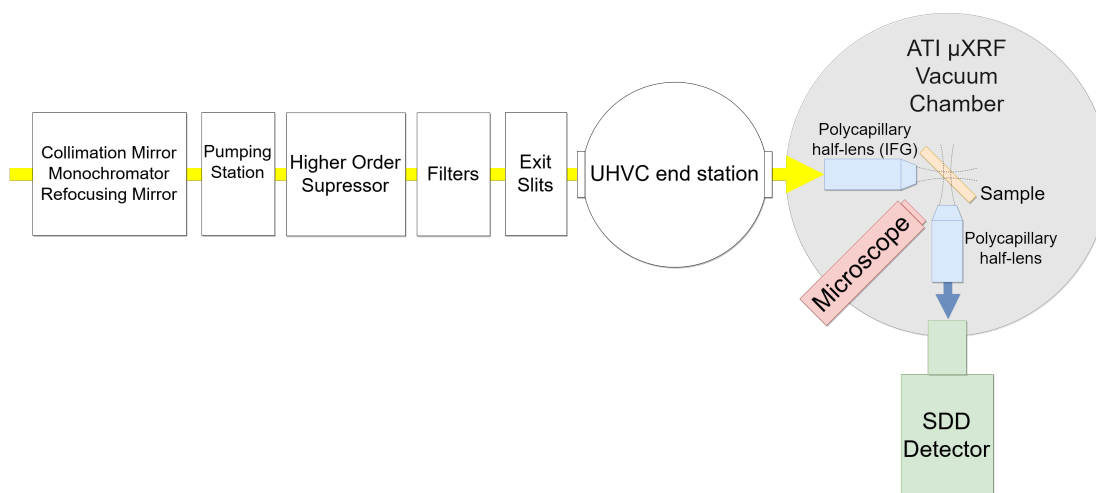


Figure 26: Schematic drawing of the experimental setup at ELETTRA - Sincrotrone

5.2. 1st Beamtime

The first experiment at ELETTRA was performed from 03/05/16 - 08/05/16. A polycapillary half-lens for the excitation channel was kindly provided by G. Pepponi.

5.2.1. Preparations

Chamber Modifications

With the tube being removed from the setup, a vacuum seal for the beam entrance hole had to be constructed in order to make measuring in vacuum conditions possible. However with a length of 60 mm and a focal length of 44 mm, the polycapillary half-lens would not fit entirely in the chamber. Therefore, a seal in the form of an aluminum cup with Kapton window, protruding from the outside wall of the chamber, was constructed (Fig. 27c). Furthermore, a new plexi-glas holder for the half-lens was constructed. A V-shaped indentation served as a support for the polycapillary, while two aluminum hooks screwed on top ensured that it was securely held in position. This simple design allowed for possible coarse adjustments of the working distance. For the half-lens to fit through the chamber hole and to still leave some space for adjustment, the outer diameter of the casing would have to be 12 mm or smaller. For testing purposes, a cylindrical aluminium dummy with a length of 60 mm and a diameter of 12 mm was constructed. Figure 27 displays the new holder with the dummy mounted, viewed from inside as well as outside of the chamber, and the mounted vacuum seal cup.

Because of its heavy weight and large size, the Si(Li) detector was not suited for transportation, so it was replaced by an SDD detector (Ketec) with 25 μm beryllium window, 80 mm² active area and an energy resolution of 145 eV @ 5900 eV. The detector finger of this SDD had a larger diameter (25 mm) than the Si(Li) detector (16 mm). Therefore, the detector hole of the chamber was widened (to 26 mm) by grinding off some material. New flange parts to fit the new detector had to be constructed as well. To make it possible to view the sample even while the shutter was open, a webcam was purchased to be mounted on top of the microscope cup. Because of the limited time, it was not possible to construct a proper mounting for the webcam, therefore a makeshift fixture using metal wires and tape had to be used.

Software Changes & Computer Setup

The SDD detector was implemented into the μXRF software package ("X-Spect" [2]), including a settings menu to set gain, threshold and shaping time ("ketek.cs"). Since the X-ray tube would be replaced by the synchrotron beam, the "TubeTune" soft-

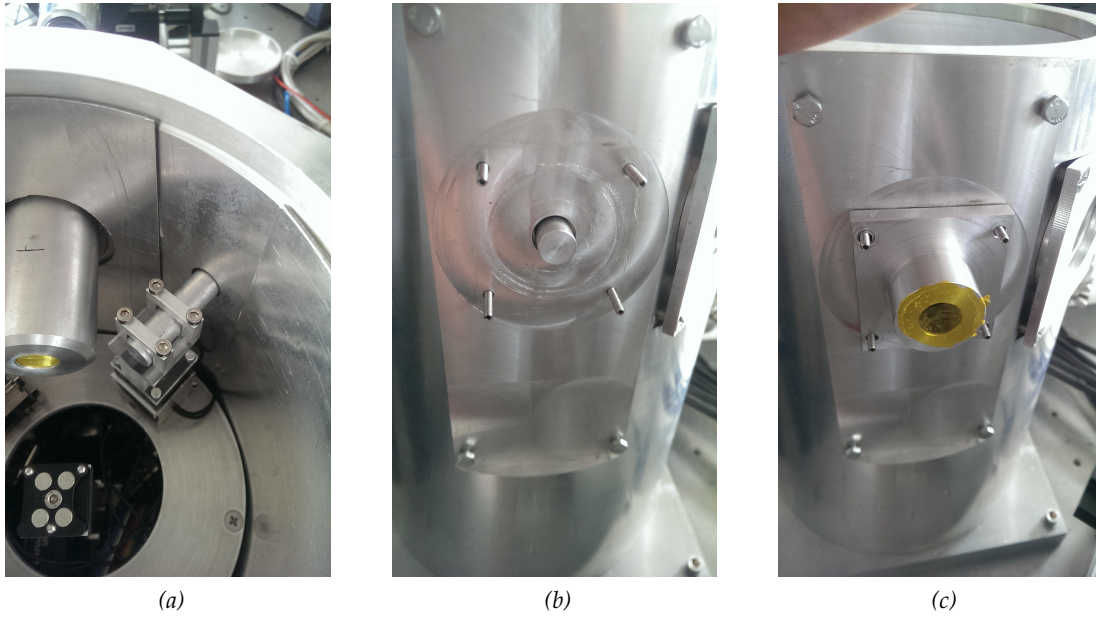


Figure 27: New plexiglas polycapillary holder with dummy (a) and aluminium cup with Kapton window replacing the tube (c) to retain possibility of vacuum environment, since polycapillary is protruding from chamber (b).

ware was commented out from the microScan software package as well as all parts of the program code that prevent the execution of scans without the powered tube. TeamViewer was installed on the μ XRF computer as well as a second computer, in order to be able to control the spectrometer from the beamline's control room whenever the hutch was closed. A long ethernet cable, guided over the wall between control room and hutch, was used to connect the two computers.

5.2.2. Setup Procedure

As a base for the spectrometer, a heavy table with adjustable feet was used. In order to reach the height of the beam exit, an optical board was mounted on top of the table and fixed with clamps. The UHVC chamber was installed in an unchangeable position. After passing through the chamber, the beam could be used for our experiment. However, due to the geometry of the UHVC chamber, it was not possible to move the μ XRF spectrometer close enough to the beam exit, i.e. there was an air gap of several cm between both chambers. A new, longer cup was constructed by the ELETTRA workshop (Fig. 28a). Figure 28b shows the finished setup after connecting the computer and all

controllers, ready for starting with the adjustment procedure.

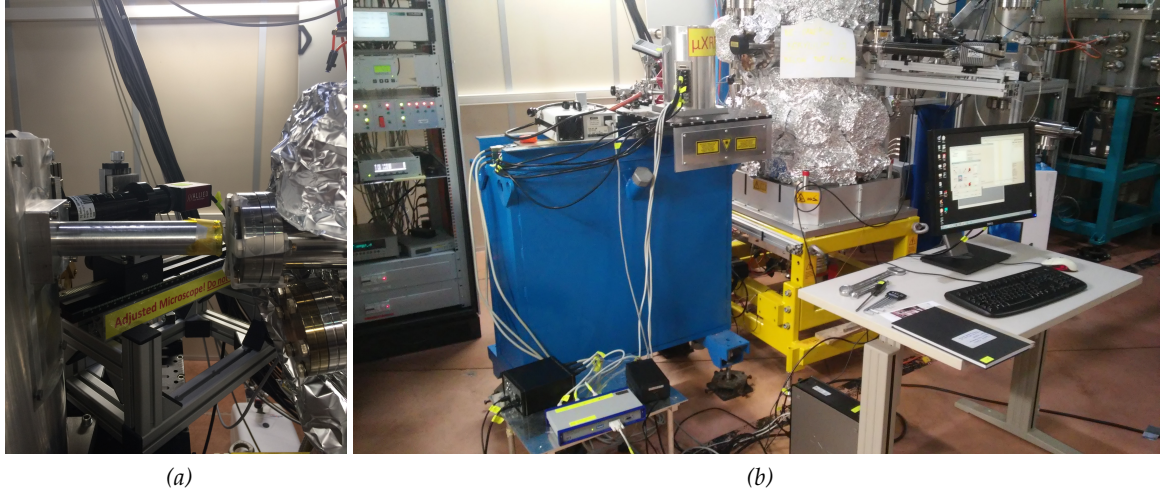


Figure 28: (a): New beam entrance cup (provided by ELETTRA workshop) to minimize beam path in air, (b): Completed ELETTRA Setup

Unfortunately the outer diameter of the polycapillary half-lens casing was not 12 mm as expected, but 15 mm. With the entrance hole of the chamber having a diameter of 14 mm, the casing was not suited for this experiment. Thus, the polycapillary half-lens had to be removed from its casing (Fig. 29a). At first, foam material was used to fit the uncased polycap into the holder (Fig. 29b). However, without a casing, it was difficult to be sure that the polycapillary was aligned parallel to the beam.

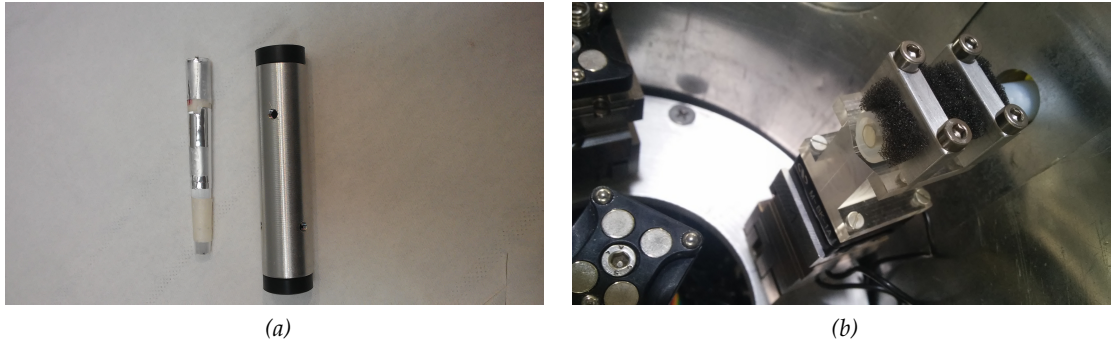


Figure 29: (a) Removed Polycapillary lens (left) and casing. (b) Unencased polycapillary in holder with foam material.

To improve stability, a dummy that had been used for preliminary tests, was utilized

to create a new casing for the PC (Fig. 29b). However, the beam was still not passing through the polycapillary optic. The reason was found to be an inclination of the incoming beam by 0.5° , given by the prealignment of the optics of the XRF beamline, that had not been communicated before. So the whole setup had to be adjusted not only in height, but also in angle. This proved to be a difficult task, since the acceptance angle of a polycapillary is of the order of mrad (e.g. 3 mrad for the critical angle at 9 keV [15]). What made it even more difficult, was the fact that no real positioning mechanism was available for adjusting the table horizontally (this includes the angle between incoming beam and chamber axis in the horizontal plane) other than manually moving the table by hand. As for the vertical positioning (and vertical angle) the adjustable table feet were utilized, although they were clearly not suited for performing such fine adjustments.

To get a rough idea of the beam path through the chamber, one piece of x-ray film was fixed to the beam entrance opening of the chamber and another piece of film was fixed at the opposite side, where the beamstopper had been removed. The shutter was then opened for a few seconds. The exposed spots on the pieces of film that were hit by the beam when entering and leaving the chamber gave information about the beam path through the chamber. Then, the table setup was moved accordingly. This procedure was repeated until the beam entered and exited the chamber centrally. Figures 30a and 30b show the pieces of x-ray film fixed to the chamber's entrance and exit and the exposed black spots after several adjustment steps.

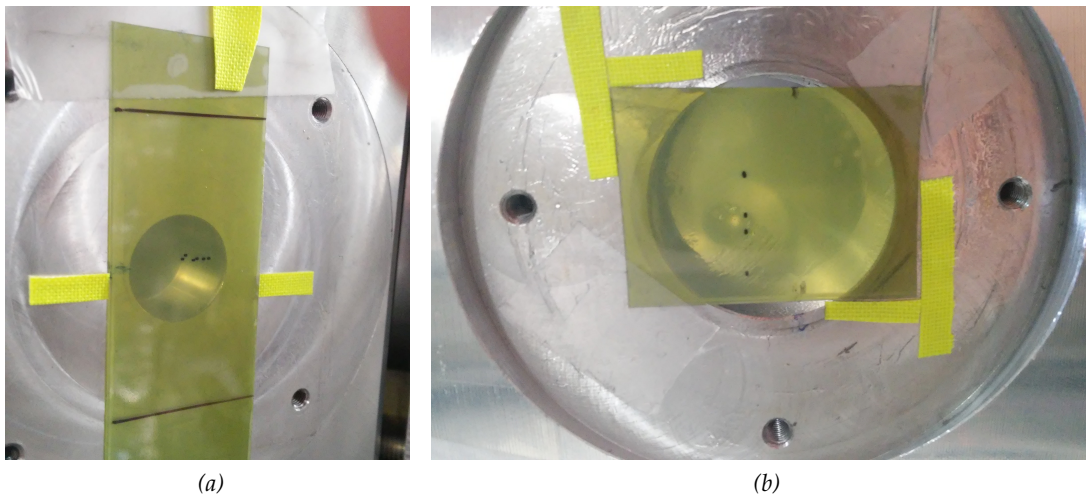


Figure 30: X-Ray Film, fixed to chamber entrance and exit, used to make beam path through chamber visible.

The polycapillary half lens was mounted in the excitation channel and the Gd screen with Cu-wire cross was mounted on the sample stage as a test sample for the adjustment procedure. However, still no signal was reaching the detector. Finally, it was concluded that it would not be possible to adjust the angle precisely enough with this manual adjustment procedure.

The piezo positioners allowed for very precise positioning, but unfortunately only translational. However, the idea was born to use them in an unconventional way: First, the polycapillary was only loosely mounted on the holder - this was achieved by removing one of the holding hooks and only loosely screwing in the second hook. Secondly, the polycapillary's end was wrapped in a soft material in order to fixate it inside the chamber entrance hole. This way, the capillary would pivot around the fixed end when moving the piezo positioners, thus it would be possible to do fine adjustments to the angle, and even do angle scans (Fig. 31).

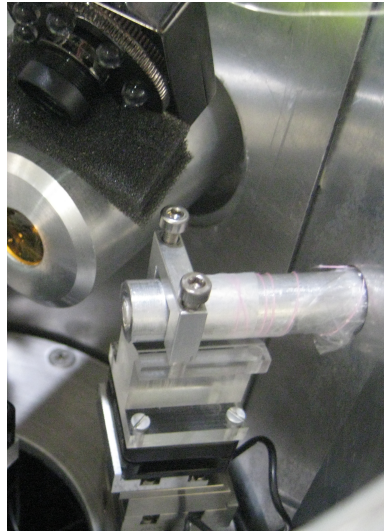


Figure 31: Makeshift mechanism for angular adjustment of excitation channel polycapillary.

Figure 32 shows the Gd-L α gross (a Gd screen was mounted on the sample stage) intensity of the successful angle scan. The step-size was roughly estimated to be 0.5 mrad, which would make the total acceptance angle of the polycapillary optics ~ 5 mrad (for Gd-L α). Note that this was a very rough estimation, since it was difficult to precisely measure the distance between pivot point and the support point on the positioner stack. The maximum intensity was 23191 Cts. in 3 seconds real time. Line-scans across a 10 μm Cu-wire were utilized to determine the beamsize after the first polycapillary. They were ~ 170 μm for X (horizontal) and ~ 120 μm for Y (vertical).

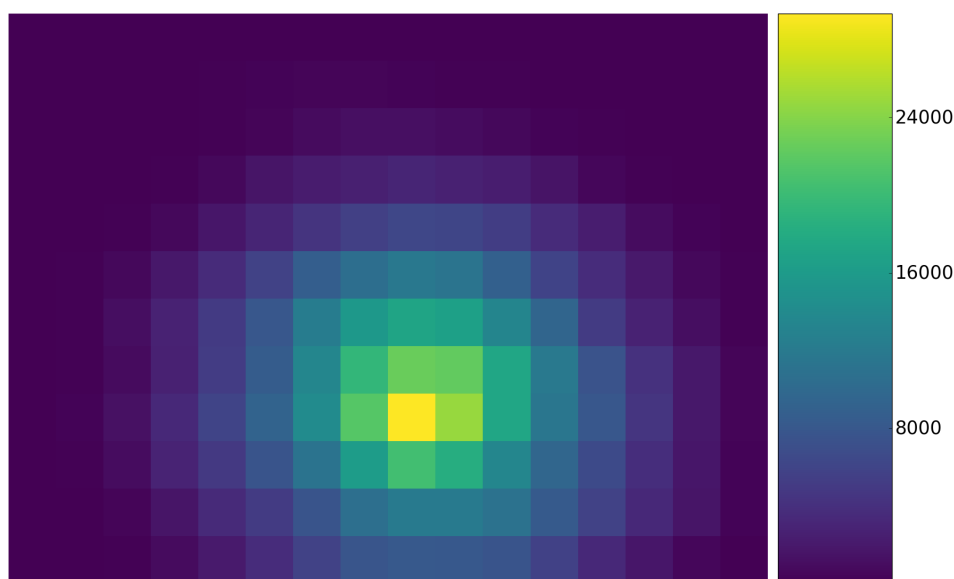


Figure 32: Gd gross map of Poly1 Angle Scan

Since the beamsize of this half-lens was quite large compared to the focal size of the half-lens in the detection channel, it was not deemed necessary to find its focal spot. While it might have been possible to minimize the beamsize, it would still have been quite large, leaving the resulting overlap with the focal spot of the second lens significantly unsymmetrical and tube-shaped. Therefore, the adjustment of the microscope focus to the polycapillary focus (section 4.2.2) was skipped and the microscope was focussed to the current sample position.

After mounting the polycapillary full-lens in the detection channel the normal adjustment procedure for confocal measuring was followed (section 4.2). To determine the shape and size of the confocal volume the cross-sections of a horizontal and vertical Cu-wire were scanned. The resulting Cu maps are presented in Figure 33.

Note, that the size of the confocal volume is quite a lot larger than in the lab system - $\sim 140 \times 40 \times 140 \mu\text{m}^3$, compared to $48 \times 35 \times 49 \mu\text{m}^3$. Furthermore these wire-scans illustrate the tube shape of the confocal volume, which was a result of the different sizes of the focal spots of the polycapillary optics.

5.2.3. Summary

Even though there were some difficulties, almost all minimal goals were achieved. The tilted beam and the small beam diameter made it difficult to adjust the chamber to the

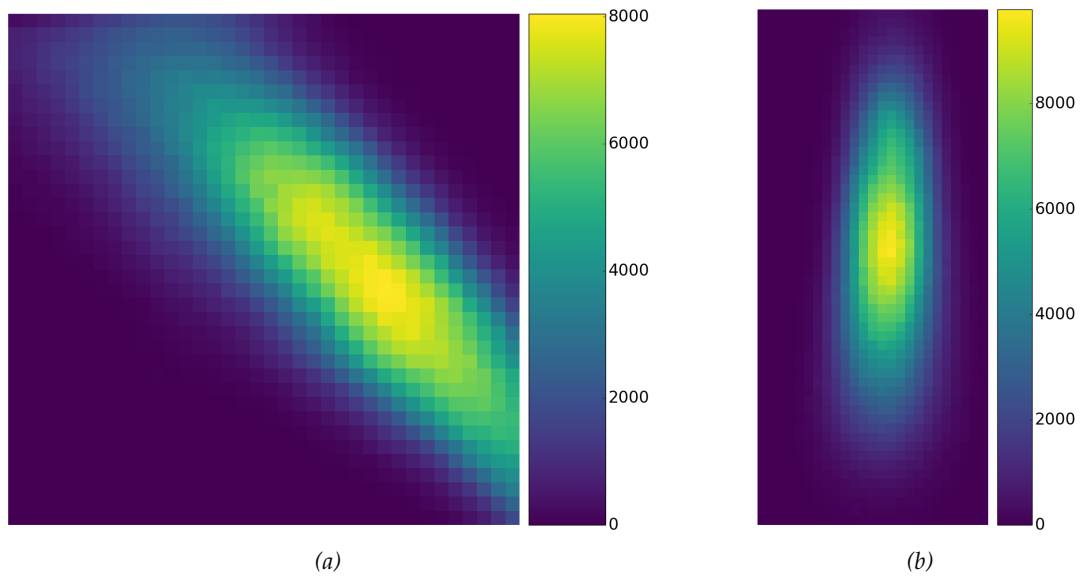


Figure 33: Cu-K α gross maps of cross-section scans of free standing Cu wire scans for horizontal (a) and vertical wire (b).

incoming beam, even more so because the possibilities for fine adjustment were limited. Still, with some improvisation a working confocal setup was achieved. Due to the large focal spot of the polycapillary half-lens in the excitation channel, the resolution was worse than for the lab system. With the multilayer monochromator not being available, the single crystal monochromator was used. Therefore, the measured intensities were comparable to the lab measurements. Because of an unresolvable technical failure of the sample stage controller, only one bone sample was measured and no vacuum measurement was done.

5.3. Second Beamtime

5.3.1. Preparations & Improvements

5.3.1.1. Polycapillary Half Lens For The Excitation Channel

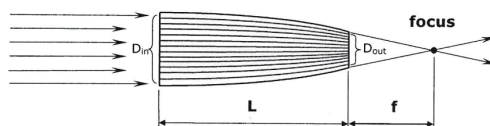
IFG kindly supplied a polycapillary half-lens for the excitation channel. In figure 34, its datasheet is presented. It can be seen that the parameters were much better suited for this experiment. With a focal size of $\sim 35 \mu\text{m}$ at the most relevant lower energies it is comparable to the detection channel half-lens (section 4.1). This would result in a clear improvement of resolution compared to the first beamtime. Besides

that, the length (36.7 mm) and working distance (~ 6.6 mm) of the polycapillary optic was perfectly suited for the limited space of the μ XRF chamber.

Polycapillary Semi-lens 179mkl36

GEOMETRICAL PARAMETERS

polycapillary optic

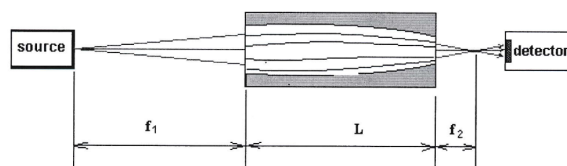


f , mm	6.6
L , mm	36.7
D_{in} , mm	4.3
D_{out} , mm	1.45

Source: Rh, $50\mu\text{m}$ - Warrickhoff

$U_a=50\text{kV}$, $I_a=600\mu\text{A}$

Detector – SDD, Bruker 30mm^2



PARAMETERS OF FOCUS

E , keV	5-7.5	7.5-10	10-15	15-20	20-25	25-30
Focus size *, μm	35	30	29	25	19	19
Intensity gain**	80	235	270	200	120	20

* - FWHM, scanning by $5\mu\text{m}$ pinhole

** - Intensity gain = Intensity through $5\mu\text{m}$ pinhole at lens focus/ Intensity of direct beam through $5\mu\text{m}$ pinhole

Figure 34: IFG polycapillary half lens data sheet

5.3.1.2. Multilayer monochromator For the second beamtime, ELETTRA was able to provide a RuB_4C multilayer monochromator, with $n = 150$ periods with spacing $d=2.51$. As explained in section 3.2.2.2, multilayer monochromators have a higher integral reflecting power, leading to a higher flux. Table 1 (section 5.1) shows that the flux is roughly two orders of magnitude higher than for the silicon single crystal.

5.3.1.3. Chamber Adjustment

A self-built system for transversal adjustment of the chamber in the plane normal to the beam-axis was designed and built. It consisted of three layers of $40 \times 60\text{cm}$ alu-

minium plates with a thickness of ~ 5 mm. To adjust the horizontal position, base and middle plate were connected with a 1D translation stage. To make fine adjustments to height as well as the angle to the horizontal plane, the top plate was connected to the middle plate with a 3-point mounting, utilizing 3 micrometer screws. With the Al plates having a thickness of only 5 mm this setup was not as stable as we would have wanted it to be, i.e. under the weight of the chamber the plates would slightly bend. However, the table provided by ELETTRA for this beamtime was not height adjustable and the range of the micrometer screws was only several millimetres. Therefore, it was necessary to design the adjustment system accordingly, to make sure that it would be possible to reach the height of the beam. To make it at least a bit more stable, three cuboid aluminium blocks were positioned between base and middle layer. Figure 35 shows a schematic drawing of the planned setup. Note that the minimal height of 1422,7 mm is barely below the nominal height of the beam with 1425 mm. To further optimize the chamber adjustment, a laser level was acquired.

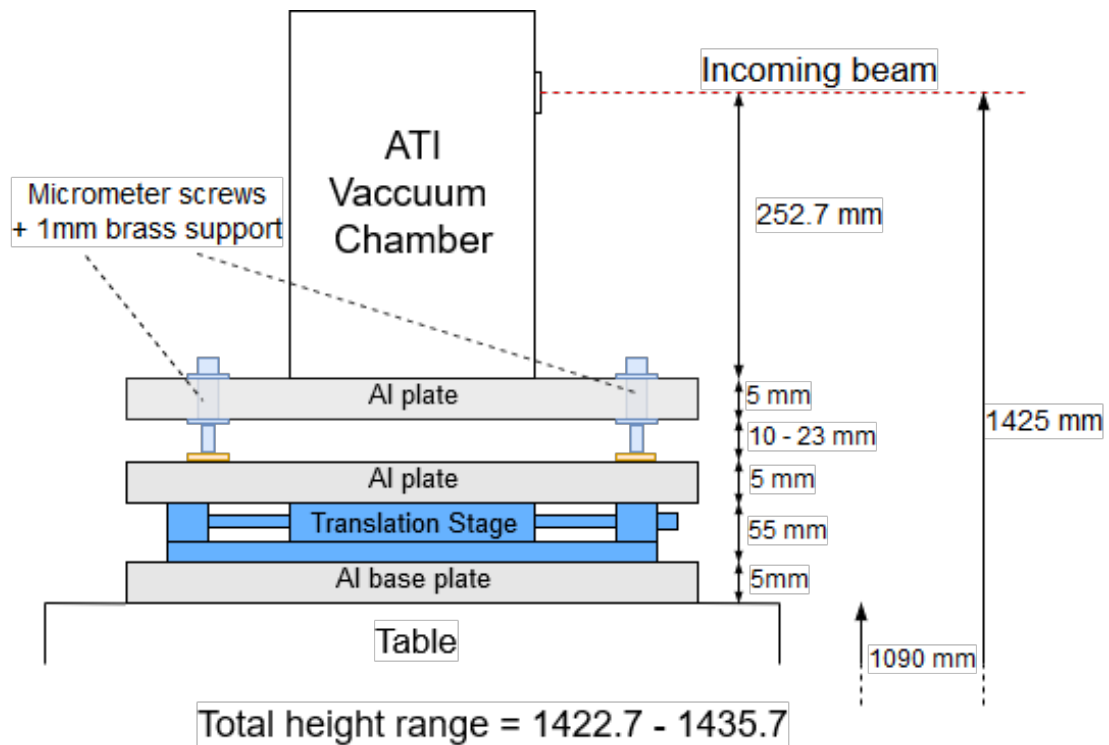


Figure 35: Schematic drawing of height fine-adjustment setup.

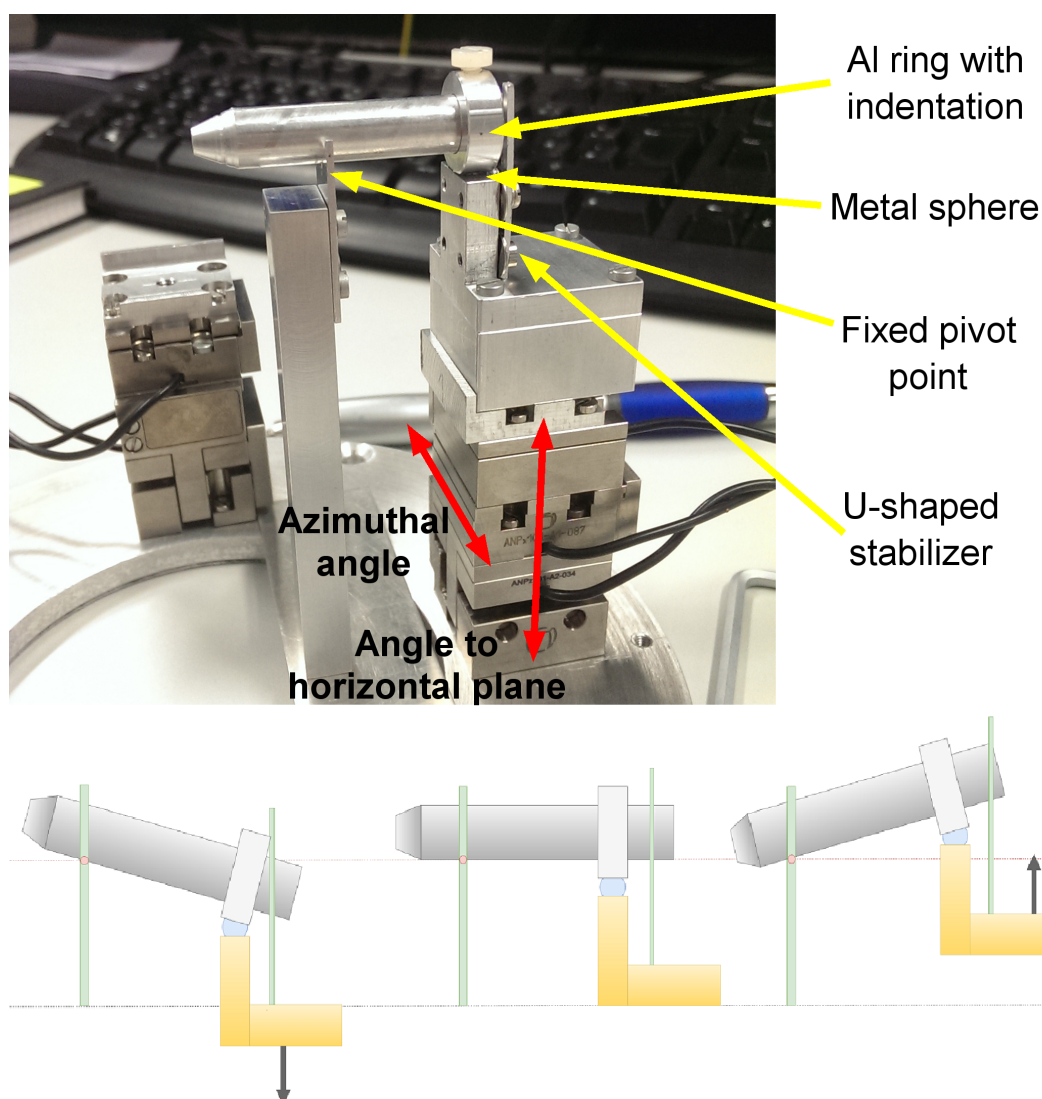


Figure 36: Above: Test arrangement of the new holder mechanism for the angle adjustment of the polycapillary half-lens in the excitation channel. Below: Drawing of the functioning principle of the mechanism.

5.3.1.4. Adjustment Of The Polycapillary In The Excitation Channel

During the previous beamtime, the biggest difficulty in adjusting the polycapillary in the excitation channel to the incoming beam had been the angle adjustment. Utilizing the same principle as during the previous experiment, i.e. combining a fixed pivot point and the translational movement of the piezo positioner stack, a more elaborate and stable mechanism was designed. Figure 36 displays the new holder mechanism.

A small V-shaped aluminium plate, mounted on an aluminium column in front of the positioner stack, served as the pivot point of the polycapillary. An aluminium holder was mounted on the piezo-positioner stack, with a small metal sphere attached to the top of it. This metal sphere served as the hinge of the mechanism. An aluminium ring, with an indentation fitting for the metal sphere, was fixed to the capillary casing with a plastic screw. A U-shaped aluminium plate screwed to the back of the holder ensured that the polycapillary does not collapse to either side. With this setup, moving the piezo-positioner in the plane perpendicular to the beam direction, would result in small angular changes of the polycapillary. This is illustrated in a drawing at the bottom of Figure 36, where up or down movements result in a change of the angle to the horizontal plane.

However, it is important to note that by using this mechanism the back of polycapillary would move, therefore the entrance position of the beam would also change slightly. This means that after finding the right angle, it might be necessary to readjust the translational position of the setup in order to hit the polycapillary in the centre.

5.3.1.5. Webcam Holder

Another difficulty had been the improvised mounting of the webcam on top of the microscope cup. Therefore, a plastic holder that could be slipped over the microscope cup was built to make for an easier and more stable adjustment (Fig. 37).

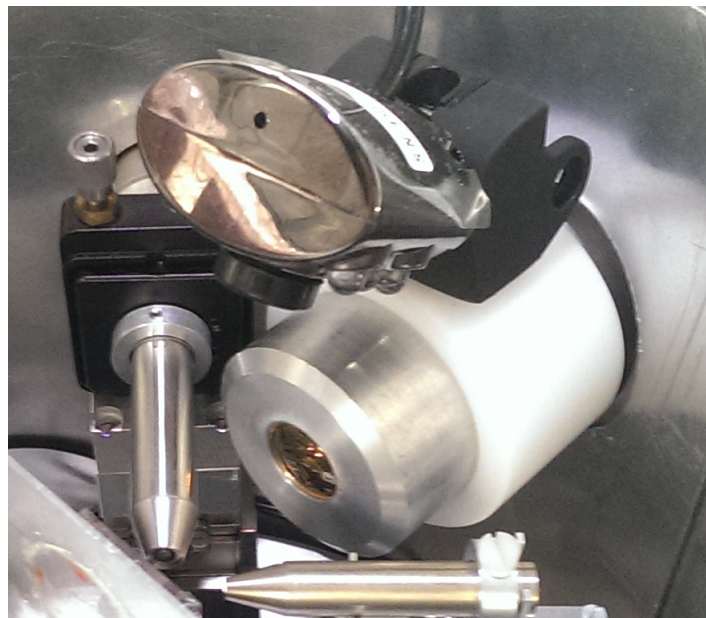


Figure 37: Webcam Holder

5.3.2. Setup Procedure

As mentioned in the previous chapter, for the second beam-time, a different non-adjustable table, and a self-built adjustable base setup was used. Figure 38 shows this base structure before starting with the setup procedure, while illustrating the first step of the adjustment procedure utilizing a laser level: First, a piece of film was attached to the UHVC chamber's beam exit as well as to the laser level across the room. In compliance with radiation safety, a lead shielding was positioned on a cabinet behind the laser level, stopping the beam before the hutch walls. After opening the shutter for a few seconds, the exposed spots on the film showed the positions of the beam. Then, the laser level was positioned in such a way, that its laser beam would intersect with both exposed spots. This meant, that the laser beam was approximately taking the same path as the x-ray beam and could be utilized as a substitute, making it possible to do a first adjustment without having to open the shutter.

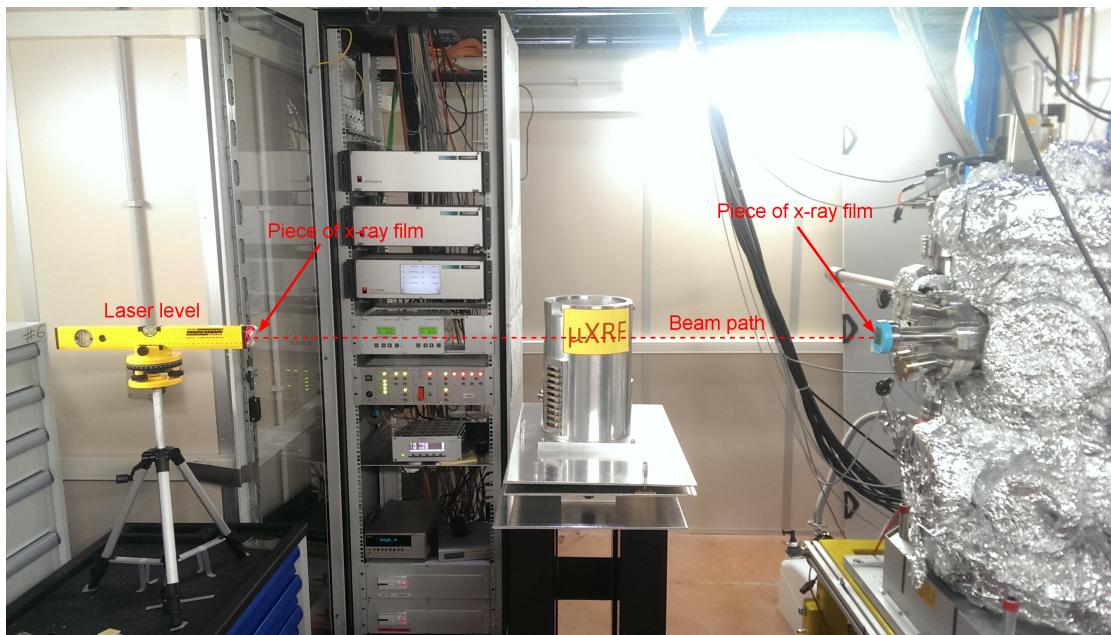


Figure 38: Illustration of the course adjustment procedure utilizing a laser level.

However, it was soon discovered that the beam was exiting the UHVC chamber at a lower height than expected (how high exactly), thus it was not possible to go low enough with the current setup. This issue was resolved by removing the bottom Al plate and screwing the translation stage directly to the table, lowering the chamber by 5 mm. Figure 39 shows this modified setup.

Finally, the chamber was roughly adjusted such, that the laser beam position when entering and exiting the chamber was as central as possible. Afterwards the lead shielding was repositioned to the back-side of the μ XRF chamber.

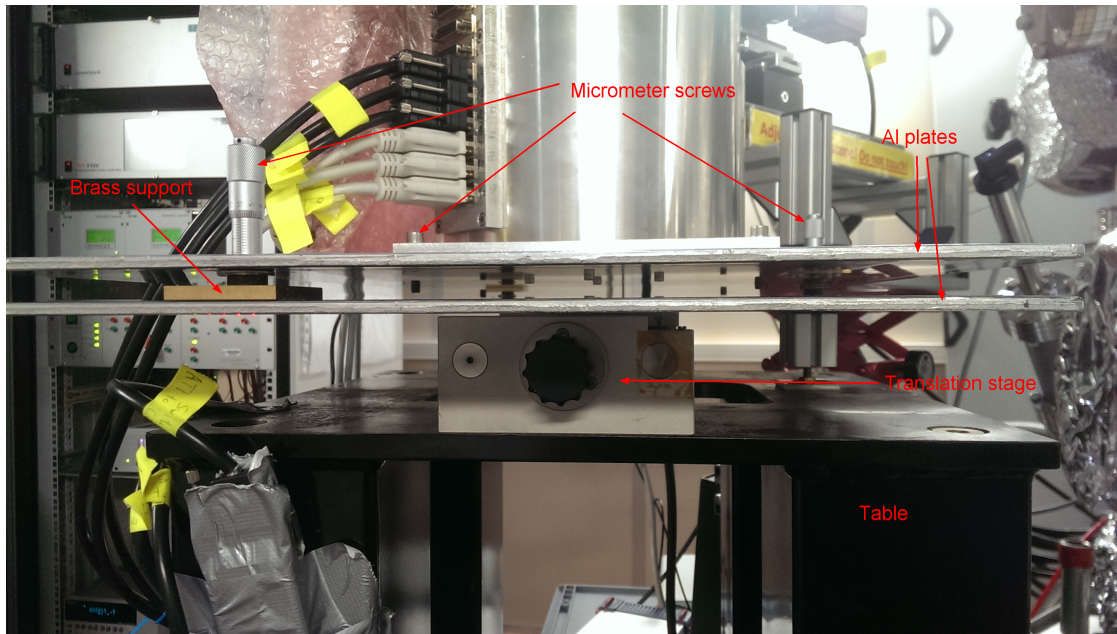


Figure 39: Base structure with bottom aluminium plate removed in order to reduce total height of the setup.

As a next step, the first polycapillary half-lens was installed in the excitation channel and the Gd screen with Cu cross sample was mounted to the sample holder. According to the plan, the next step would have been to perform angle scans, utilizing the new holder mechanism, in order to find the right angle for the beam to pass through the optics. Unfortunately, after a first preliminary scan, one of the piezo positioners malfunctioned, more precisely the positioner responsible for moving the stack up and down. This meant, that it would be possible to adjust the azimuthal angle of the polycapillary using the positioner stack, but not the angle to the horizontal plane. Fortunately, the new base construction provided the possibility to manually adjust the elevation of the whole setup, namely by either adjusting the micrometer screw at the front-side or by equally adjusting the 2 micrometers at the back-side of the base.

The new resulting adjustment procedure consisted of alternately adjusting the angle to the horizontal plane manually utilizing the micrometer screws, then scanning over the possible range of azimuthal angles using the still functioning piezo positioner. To get an idea of the necessary change of the elevation angle, small pieces of x-ray film

were fixed to the entrance of the polycapillary optics and to the exit opening of the μ XRF chamber (Fig. 40). After opening the beamline shutter for a few seconds, the visible dots, where the film had been exposed to the beam, were giving information about the beam's path through the optic. The goal was of course to get the beam to enter and exit the polycapillary optics as centrally as possible.

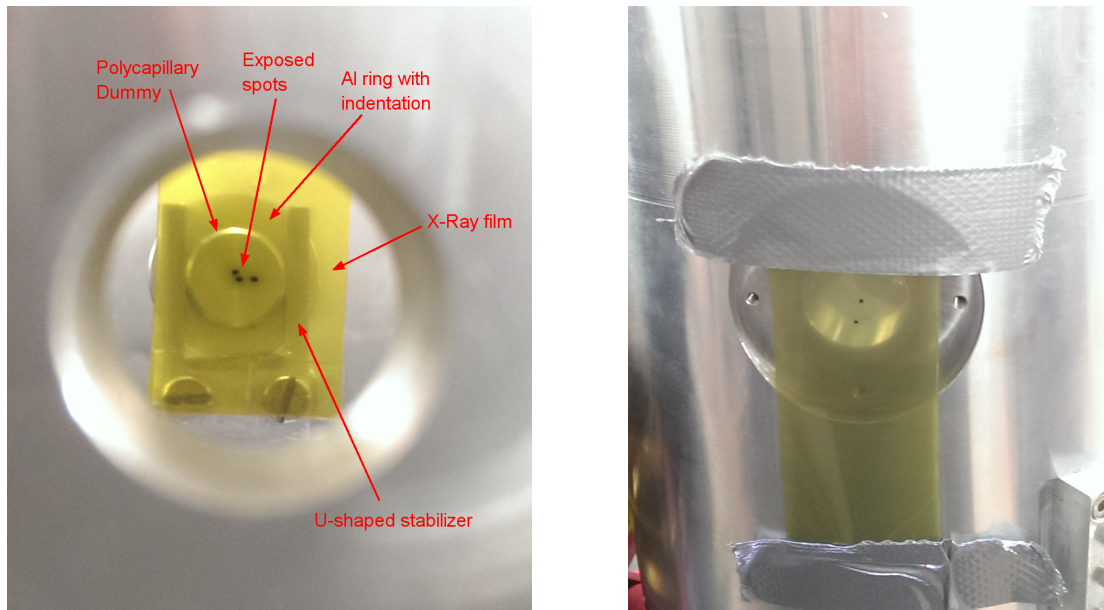


Figure 40: X-ray film on dummy and chamber to visualize beam path.

After a prolonged adjustment procedure, we finally succeeded in measuring a Gd signal. In order to not overstrain the detector, a 240 μm sheet of Al was fixed to beam-exit of the UHVC chamber to attenuate the incoming beam. After optimizing the polycapillary position to the maximum countrate, the lead shielding was removed and the beam-stopper was re-installed in anticipation of potential vacuum measurements. Unexpectedly, after this was done, again no fluorescence radiation was reaching the detector. First we tried to adjust micrometer screws to get back beam, but we couldn't reach it with our range. Apparently, the weight of the lead shielding was necessary to shift the angle just a little bit, and since we were so close to the edge of the possible range of the micrometer screws, it was not possible to achieve the same result with just the micrometer screws. An attempt to clamp the two aluminium plates together on one side, in order to obtain the necessary angle change, was unsuccessful. Hence, the setup was reverted back to its previous state, with the beam stopper removed and with the lead shielding resting on the side of the chamber. Then, the adjustment procedure was

repeated. Finally, we succeeded in measuring a signal again. After further optimizing the chamber position, ~ 9400 cps (Gd-L α gross) were reached.

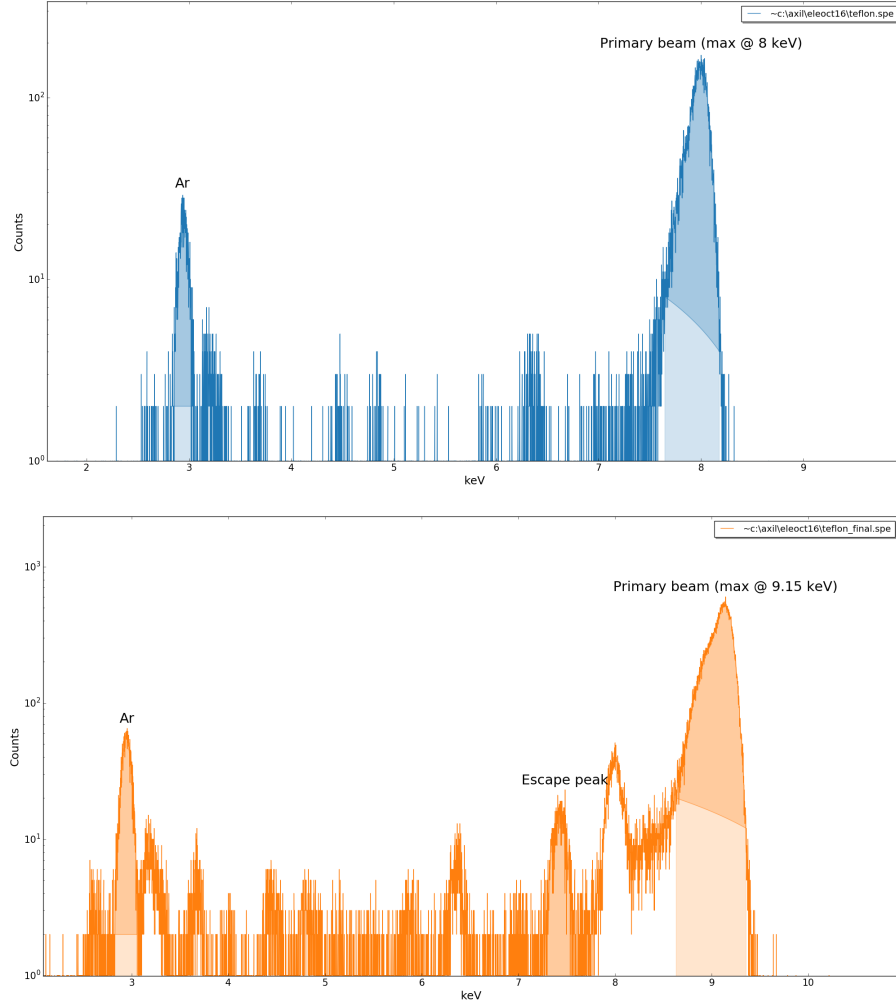


Figure 41: Measurement of teflon disc with nominal primary beam energy of (a) 8 keV and (b) 9.2 keV

We suspected that the primary energy might not be 9.2 keV, hence a test measurement was carried out on teflon as scatterer, to determine the energy of the elastically scattered radiation (Fig. 41a). The measurement showed, that the beam energy was actually around 8 keV. Another measurement was performed after the beam energy was changed to 9.2 keV (Fig. 41b). The higher primary beam energy resulted in a higher flux, a repetition of the measurement on the Gd screen showed a count-rate of ~ 16000 cps with 100 % dead-time. To reduce the dead-time, the 240 μ m Al filter

mounted in front of the chamber was replaced by a 1 mm Al filter, resulting in a count-rate of only ~ 100 cps Cu-K α gross measured on the Cu cross. The filter was then exchanged for a 480 μm Al foil. Measuring again on the Cu cross gave a count-rate of ~ 20000 cps Cu-K α gross, with a dead-time of $\sim 39\%$

A linescan across a horizontal as well as a vertical free standing Cu-wire ($d = 10 \mu\text{m}$) was performed to estimate the beam dimensions after the first polycapillary optic. Figure 42 shows the Gauss fitted count-rates along the line-scans. The FWHM was 57 μm for X (horizontal) and 36 μm for Y (vertical). The beam-size is then given by $d_{\text{beam}} = \sqrt{\text{FWHM}^2 - d_{\text{wire}}^2}$ (see 4.2.2). The resulting beam-dimensions were $56 \times 35 \mu\text{m}^2$ (h x v). The beam is elongated in X on the sample because of the 45° geometry, if we account for this we get the actual beam size of $\sim 40 \times 35 \mu\text{m}^2$ (h x v).

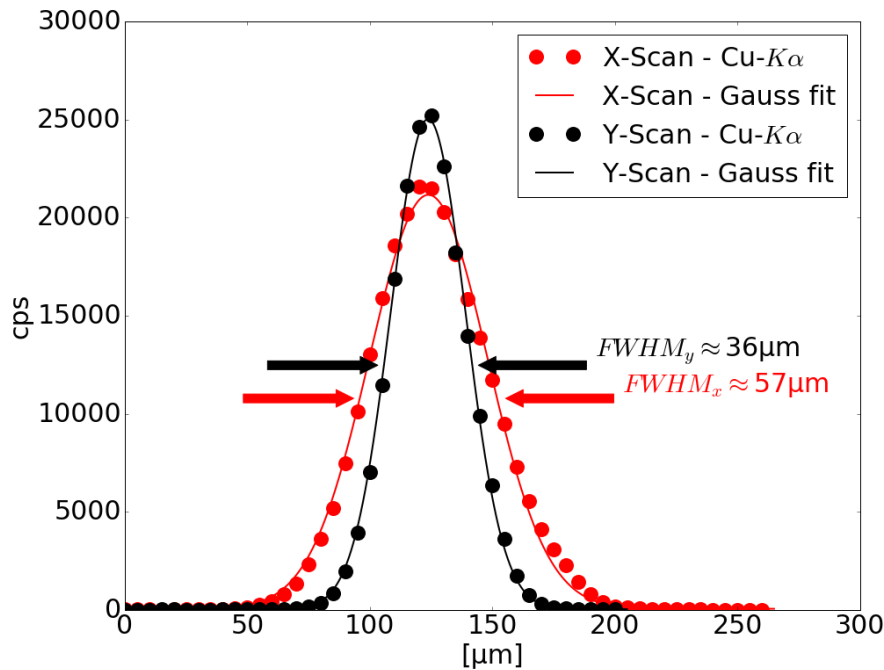


Figure 42: Cu-K α count-rate for line-scan across horizontal (red dots) and vertical (black dots) free-standing Cu-wire ($d=10\mu\text{m}$) in non-confocal mode. The data was Gauss-fitted (red/black line) to extract the FWHM in both dimensions.

Normally the focus position of the first polycap would be determined, and then the microscope focus would be adjusted to the focal plane. However, since the beam diameter was already sufficiently small for our purposes, this step was skipped in order to save time. Thus, the microscope focus was adjusted to the current sample position. Still, we performed two more horizontal linescans (X-scan) after varying the distance

between polycapillary and sample, in order to observe the change to the focussed beam. The first scan was performed after increasing the distance by 1 mm, the second one after decreasing it by 1 mm. The Cu-K α gross values of the linescans are compared in Figure 43. Increasing the distance between polycapillary and sample resulted in a broader beam with a FWHM of 84 μm , while decreasing it led to an even smaller beam than before, with FWHM = 45 μm . Since time was a critical factor, only a rough estimation of the beam diameter was carried out at the time, therefore this small improvement was not observed and the current Z value was used.

Next, the second polycapillary half-lens was installed in the detection channel. The usual adjustment procedure (Ch. 4.2.3) was performed on the Cu cross on Gd screen sample. A maximum of ~ 13300 cps Cu-K α gross was reached. In order to determine the dimensions of the confocal volume, area-scans over the cross-sections of the horizontal and vertical Cu wires were carried out. The resulting fitted maps are presented in figure 44. The column and line containing the maximum of each scan were Gauss fitted to obtain the confocal volume dimensions. The obtained dimensions were $41 \times 24 \times 34 \mu\text{m}^3$ (h x w x d).

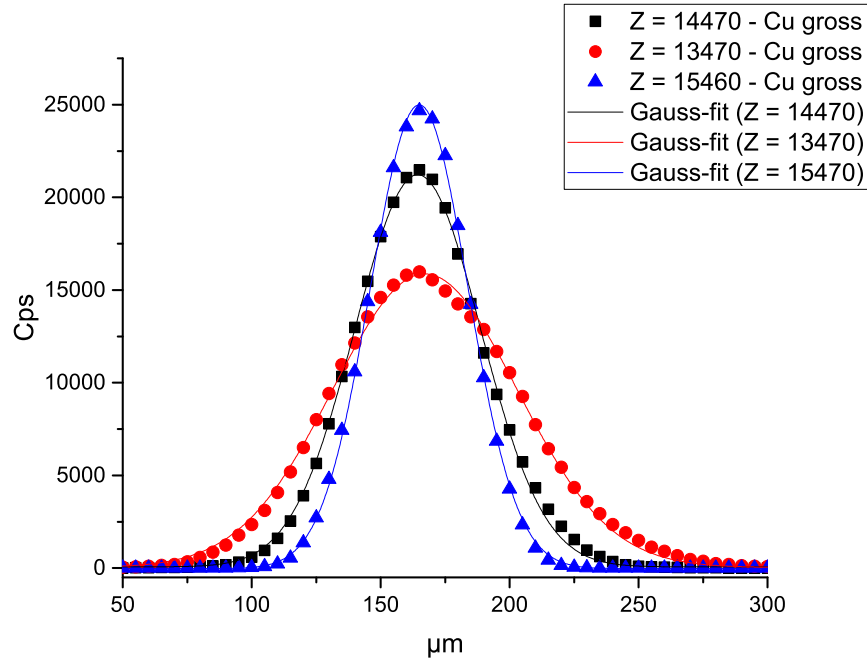


Figure 43: Gauss fitted Cu-K α gross data for linescans across Cu wire while varying distance between polycapillary and sample.

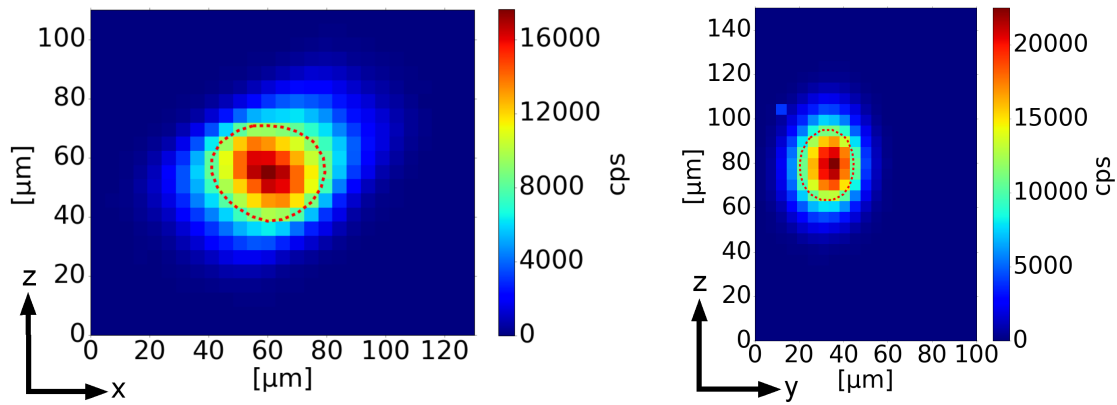


Figure 44: Cross-section area scan of horizontal (left) / vertical (right) Cu-wire to determine confocal volume size for Cu-K α . The dashed red line marks the FWHM of the distribution. Obtained dimensions: 41 x 24 x 34 μm^3 ($w \times h \times d$).

Figure 45 shows images of the completed confocal setup and the μXRF after the successful adjustment.

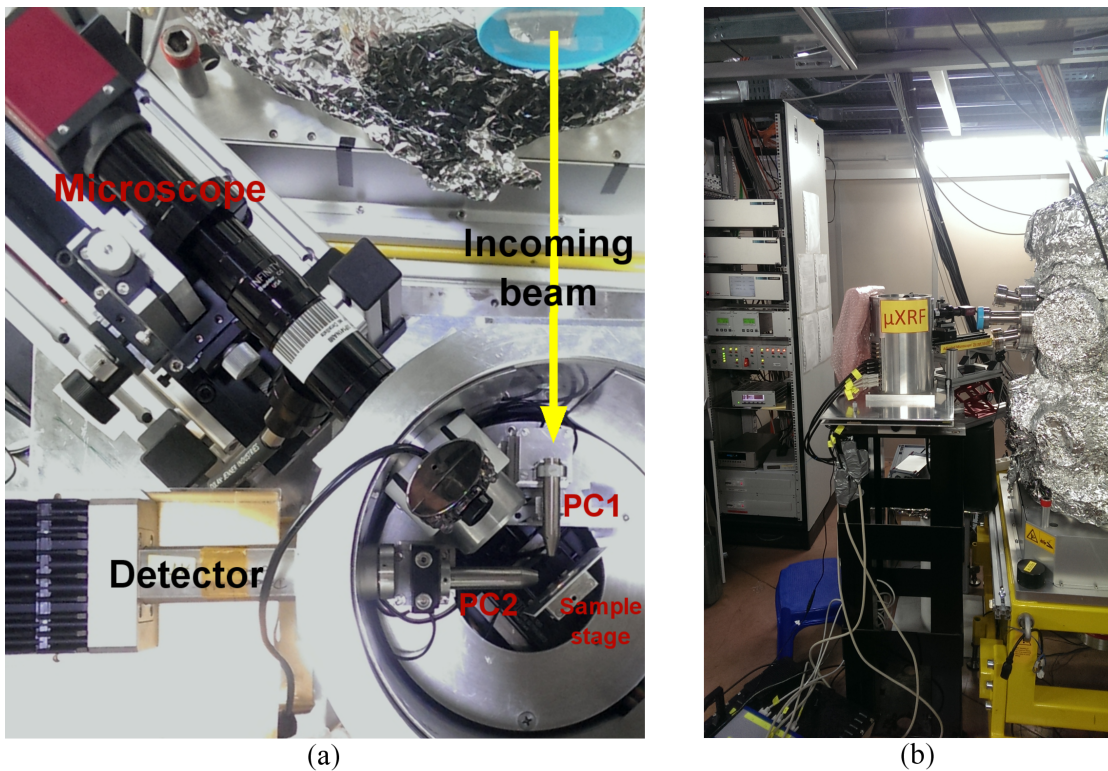


Figure 45: Completed setup: Top-view of confocal setup (a) and side-view of the ATI μXRF chamber besides the UHVC end station.

With the second polycapillary optics reducing the total number of photons reaching the detector, the 480 μm Al filter was removed from the beam-exit. In order to attenuate the dominating Ca peaks, and especially the Ca sum escape peaks in the bone sample spectra, and therefore improve the measurability of overlapping elements (e.g. Mn), a 20 μm Al filter was fixed onto the exit of the detection channel polycapillary. The transmission of Ca for 20 μm Al was calculated to be $\sim 10\%$. However, the comparison of a single measurement on the bone sample MN4 before and after the filter was introduced to the system, showed a drop of the measured Ca intensity to $\sim 4\%$. It was concluded that the polycapillary optics was probably slightly moved when attaching the filter. Therefore, the adjustment procedure of the detection channel optics was repeated, this time on the sample MN4, using Ca countrates. On the maximum position, a countrate of ~ 30000 cps for Ca gross was achieved.

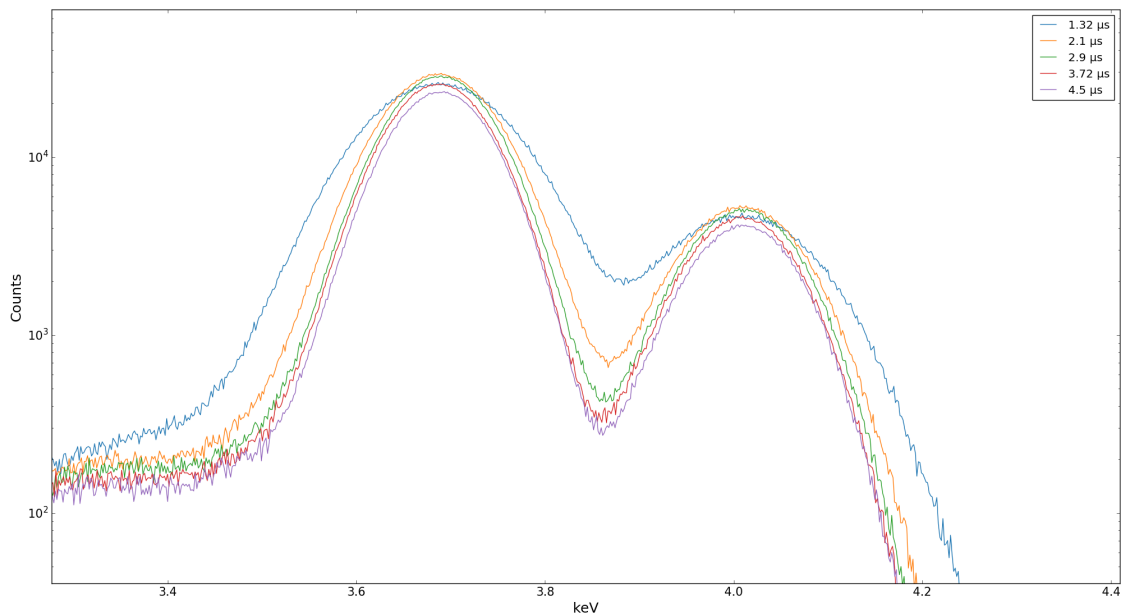


Figure 46: Comparison of Ca peaks for varying values of the shaping time.

With filters removed from the excitation channel as well as the detection channel, the detector dead time reached values as high as 50 %. In an effort to reduce the dead-time, the shaping-time of the detector was optimized. While reducing the shaping-time will lead to a reduction of the dead-time, it will also negatively affect the energy resolution. In order to find the best value, a single spectrum was measured for each possible shaping-time setting (again on the sample MN4) and the spectra were compared. Figure 46 shows a close-up of the Ca $K\alpha$ and $K\beta$ peaks for the different shaping-times. For

shaping-times of 2.9 μs and longer the peak shape is relatively unchanged. For 2.1 μs the peaks are only slightly broadened while at 1.32 μs a clear broadening of the peaks is visible. Using a shaping-time of 2.9 μs , the dead-time was still at 35 %. Since the broadening of the Ca peaks for 2.1 μs shaping-time was still relatively small, we decided to use this setting for our measurements. For this setting, the count-rate was ~ 42000 cps Ca-K α gross and the dead time was ~ 25 %.

5.3.3. Summary

Thanks to a superior polycapillary half lens in the excitation channel and an improved adjustment procedure, the ATI μXRF chamber was successfully installed and adjusted to the synchrotron beam in confocal mode, taking ~ 3 days. The confocal volume size was determined as $41 \times 24 \times 34 \mu\text{m}^3$ (h x w x d), which was a significant improvement to the first beamtime. In order to test the setup, five test measurements on bone samples were performed. Due to the utilization of a multilayer monochromator, measured intensities were $\sim 200 - 300$ times higher than for the first beamtime, leading to a considerable improvement of the results.

5.4. Measurements

In this chapter, all results obtained from the sample measurements that were performed during the two synchrotron experiments will be presented, with the addition of one reference measurement that was conducted in the lab. The samples are all human bone samples that are part of different ongoing projects. Since the focus of this thesis is on the technical side of the experiments, no precise information about the samples and the associated research questions will be given. Rather, in the upcoming chapters, detailed information on the data acquisition parameters as well as all parameters used for fitting will be given, while discussing any potential difficulties and issues, and finally the resulting analyzed data will be presented.

5.4.1. MN4 - Area B

The sample MN4B was the only sample that could be successfully measured during the first beamtime, since a technical failure prohibited additional measurements. The same area was also measured during the second beamtime as well as in the lab, in order to directly compare the capabilities of the three different setups. For all three

measurements, the Ketek SDD detector was utilized. Table 2 shows an overview of all scan and fit parameters of those three measurements.

Sample	MN4B - Lab
Tube settings	50 kV, 0.4 mA
Stepsize	$x = y = 50 \mu\text{m}$
Map-Size	$18 \times 14 \text{ pixel} = 252 \text{ points} = 900 \times 700 \mu\text{m}^2$
Measuring time	200 s/point (real time)
Total measuring time	50400 s \sim 14 h
Mean dead-time	$\sim 0.5 \%$
Fitted elements	Ar, Ca, Cl, Cu, Fe, Gd, K, Mn, Cr, Ni
AXIL model	Ortpol: P=6, R=1.5
PyMca model	Hypermet, No Continuum, SNIP: width =67, smoothing = 19 Include: Stripping, Esc peaks, Pile-up, Short tail

Sample	MN4B - 1st beamtime
Excitation energy	9.2 keV
Stepsize	$x = 60 \mu\text{m}, y = 35 \mu\text{m}$
Map-Size	$12 \times 15 \text{ pixel} = 180 \text{ points} = 720 \times 525 \mu\text{m}^2$
Measuring time	250 s/point (real time)
Total measuring time	45000 s \sim 12.5 h
Mean dead-time	$\sim 0.6 \%$
Fitted elements	Ar, Ca, Cl, Cu, Fe, Gd, K, Mn, Cr, Ni
AXIL model	Ortpol: P=6, R=1.5
PyMca model	Hypermet, No Continuum, SNIP: width =67, smoothing = 19 Include: Stripping, Esc peaks, Pile-up, Short tail

Sample	MN4B - 2nd beamtime
Excitation energy	9.2 keV
Stepsize	$x = y = 25 \mu\text{m}$
Map-Size	$29 \times 25 \text{ pixel} = 725 \text{ points} = 700 \times 600 \mu\text{m}^2$
Measuring time	60 s/point (real time)
Total measuring time	43500 s \sim 12 h
Mean dead-time	$\sim 22 \%$
Fitted elements	Ar, Ca, Cl, Cu, Fe, Gd, K, Mn, Cr, Ni
AXIL model	Ortpol: P=6, R=1.5
PyMca model	Hypermet, No Continuum, SNIP: width =67, smoothing = 19 Include: Stripping, Esc peaks, Pile-up, Short tail

Table 2: MN4B - Scan & fitting parameters

Figure 47 compares the sum spectra of the three measurements. As can be seen from table 2, the total measurement for all scans is the range of ~ 40000 to 50000 seconds. The same element peaks are visible in all three spectra, with the exception of Zn (absorption edge: $K_{ab} = 9.660$ keV) and Pb (lowest absorption edge: $L_{IIIab} = 13.044$ keV), which were only detected in the lab, since they could not be excited with the beam energy set to 9.2 keV at ELETTRA. Furthermore, the much higher intensity for the second beamtime (see section 5.3.1.2) lead to high Ca sum and escape peaks, which are overlapping with trace elements of interest, e.g. Mn.

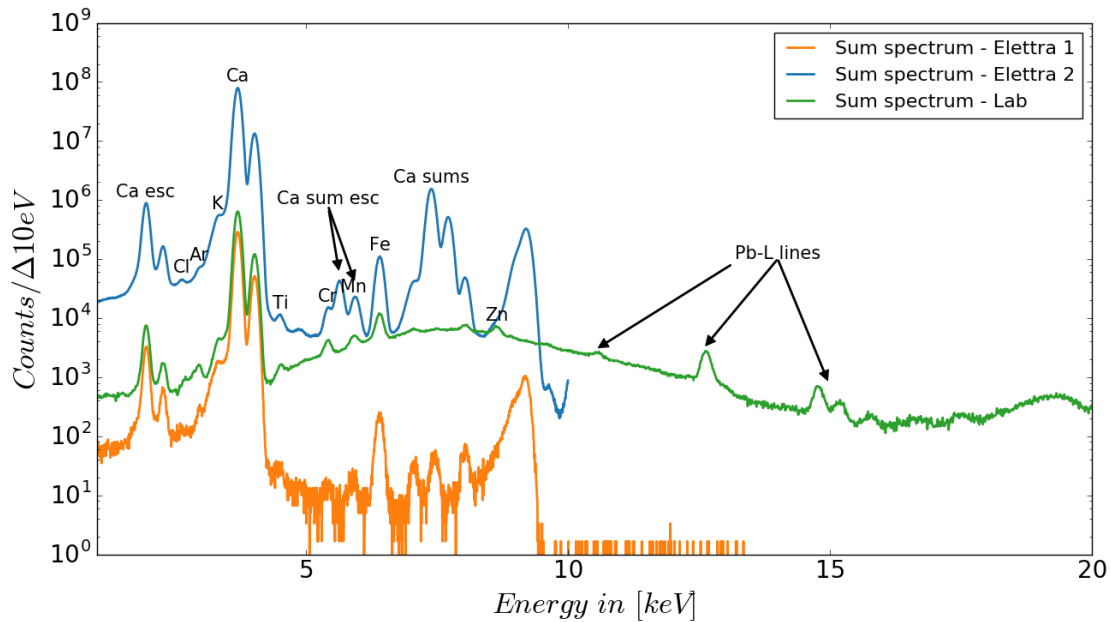


Figure 47: MN4B Sum Spectra - comparison.

Figure 48 compares single spectra obtained at similar positions at the different experiments. While the Ca intensities for the lab measurement and the first beamtime are comparable, the Ca peak for the second ELETTRA beamtime is $\sim 200 - 300$ times higher. This rise in intensity is due to the high integral reflecting power of the multi-layer monochromator (section 3.2.2.2), compared to the single crystal monochromator that was in operation during the first beamtime. In the lab spectrum, Mn and Fe peaks on top the background can be recognized, while for the first ELETTRA measurement there is barely anything visible other than Ca and K.

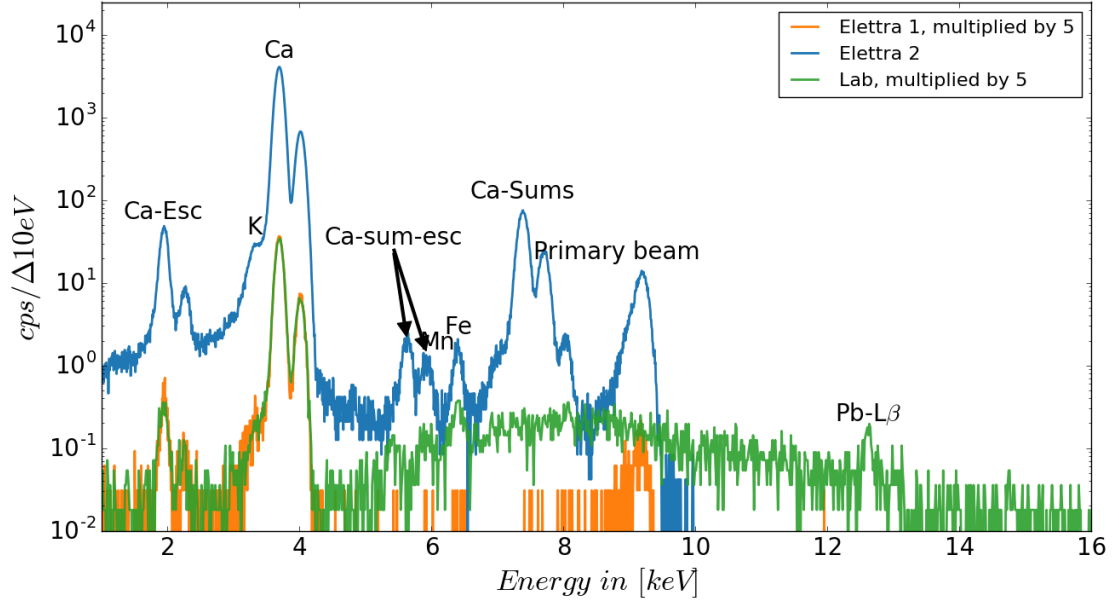


Figure 48: MN4B - single spectra comparison

In Figure 49, all elemental maps of the MN4B sample, produced from the data acquired during the three experiments, are presented. For a complete comparison, all elemental maps that could be produced for the second ELETTRA measurement are also shown for the lab and first ELETTRA measurements. Due to the low intensities, most elements were only detectable for the second ELETTRA measurement.

For the lab measurement, only the Ca map shows the correct structure. The K map has a similar structure, but since the K peak lies on the shoulder of the high Ca-K α peak, it is generally difficult to fit correctly. All other maps show almost no structure and are mainly peaks that were incorrectly fitted into the background.

For the first ELETTRA measurement, the Ca map shows the expected structure. All other maps do not contain meaningful information, but are presented for comparison.

For the second ELETTRA beamtime, for all elements that were identified in the spectra, reasonable maps could be produced. In the bottom right corner of the scan area, a small area containing Cu, Ni, Mn, Fe and Cr was identified as contamination, most likely originating from the sample preparation procedure. To improve the contrast on the Fe, Mn and Cr maps, the pixels containing the contamination were set to zero on those maps. Figure 50a shows the elemental maps with contamination and 50b shows a single spectrum from the contaminated region.

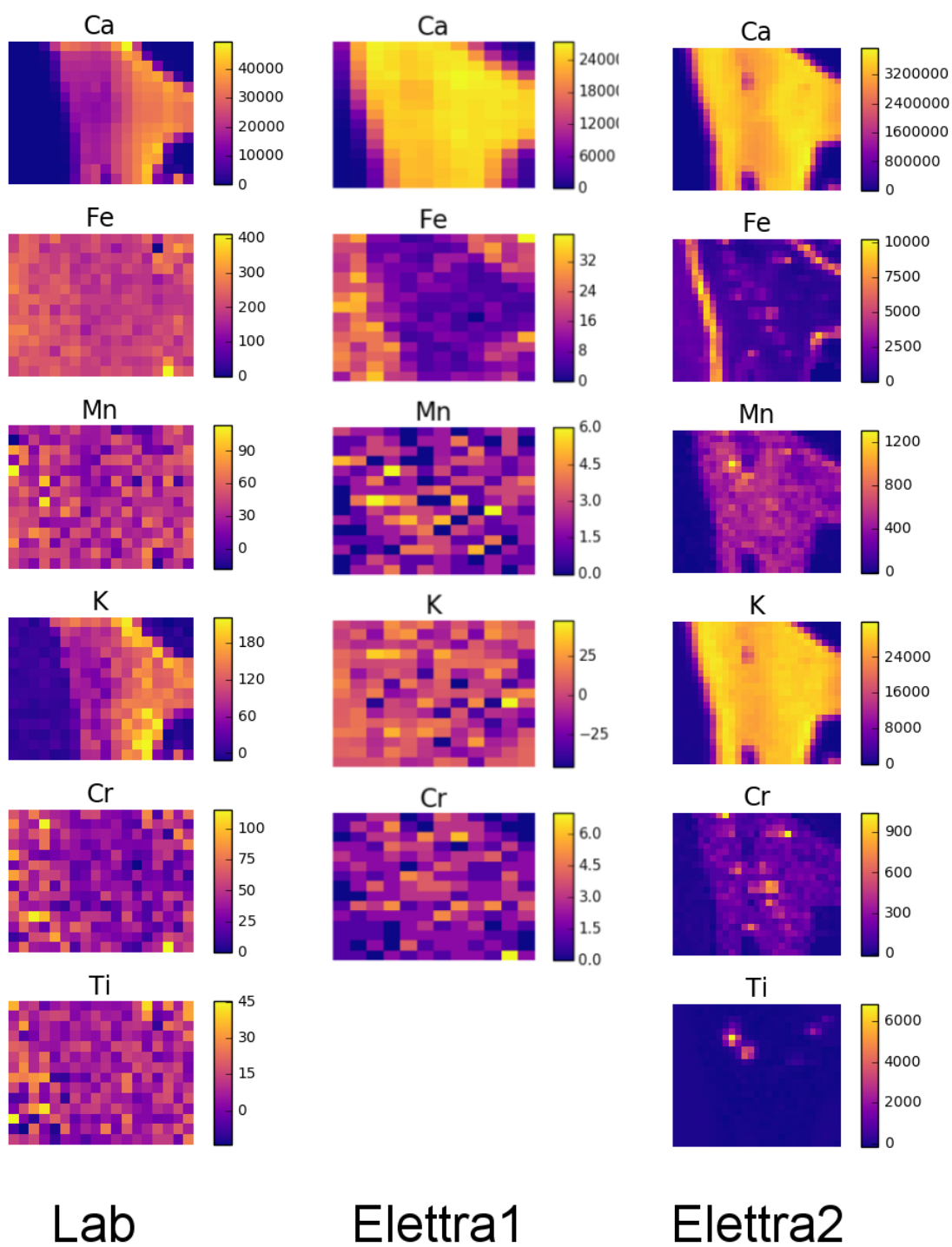
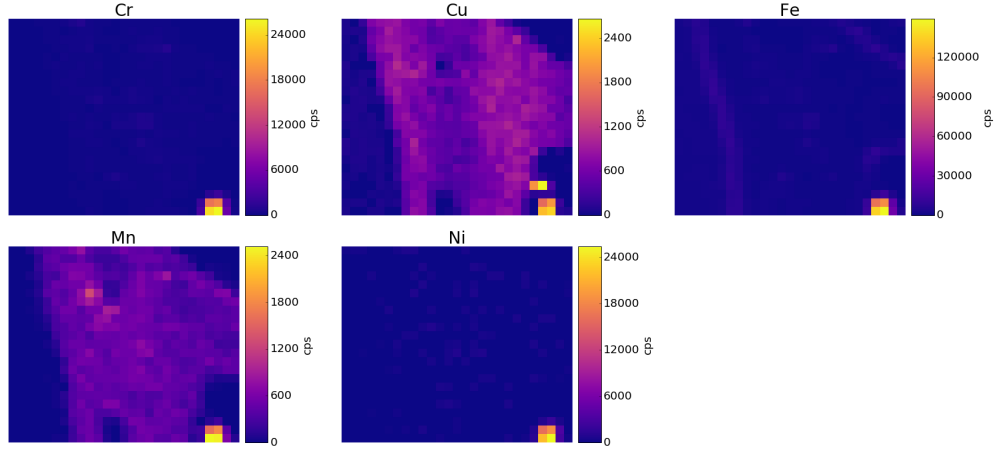
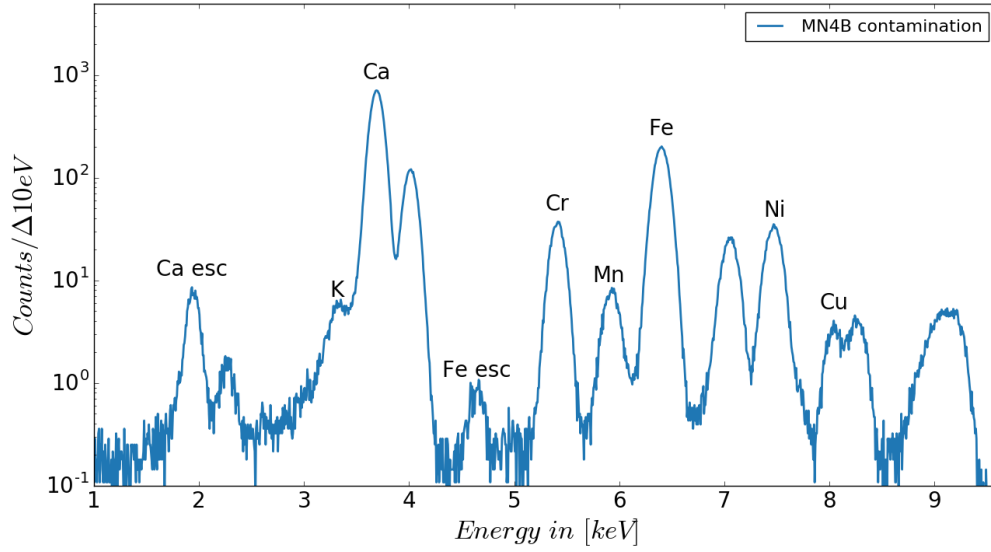


Figure 49: MN4B - Comparison of elemental maps.

Cu, Ni and Mn are not visible in the sum spectrum, because the corresponding peaks are overlapping with either Ca sum or Ca sum esc peaks. Even though Cl and Ar are visible in sum spectrum, the peaks in single spectra were not high enough to be fitted consistently. Additionally, the utilization of a confocal setup reduces the excitation of Ar significantly.



(a)



(b)

Figure 50: MN4B - Contamination: Elemental maps (a) and single spectrum from contaminated region (b).

Because of the high Ca concentration, it is a difficult task to fit Mn. In Figure 51 this

problematic part of the spectrum is illustrated. The dashed lines show the fitting results from a single spectrum for Mn-K α and the Ca sum esc pileup. A possible improvement to this situation could be accomplished by the application of a filter between the second optic and the fluorescence detector, with the goal of achieving a higher attenuation of Ca compared to Mn. As mentioned in section 5.3.2, this approach was attempted prior to this measurement - a 20 μm Al filter was installed - however, the remaining radiation was not sufficient to give reasonable results. There is a possibility that the polycapillary in the detection channel was slightly moved when attaching the filter, since the Ca peak was attenuated to $\sim 4\%$ instead of the expected $\sim 10\%$. Still, all things considered, it was concluded that the flux through the polycapillary was not sufficient to utilize a detector filter.

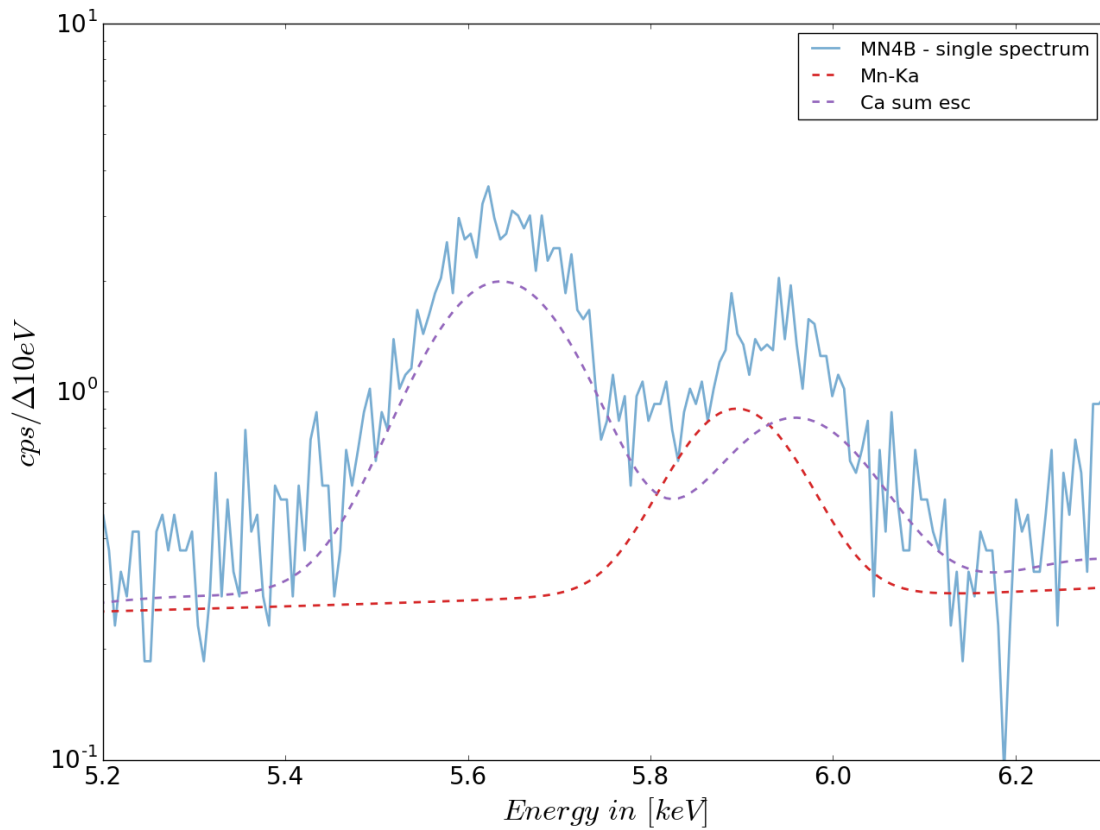


Figure 51: MN4B: Overlap of Mn-K α with Ca sum esc

5.4.2. MN8 - Area B

Sample	MN8 - Area B
Excitation energy	9.2 keV
Stepsize	$x = y = 25 \mu\text{m}$
Map-Size	$24 \times 25 \text{ pixel} = 600 \text{ points} = 575 \times 600 \mu\text{m}^2$
Measuring time	60 s/point (real time)
Total measuring time	35940 s $\sim 10 \text{ h}$
Mean dead-time	$\sim 28 \%$

Fitted elements	Ar, Ca, Cl, Cu, Fe, Gd, K, Mn
AXIL model	Ortpol: P=6, R=1.5
PyMca model	Hypermet, No Continuum, Strip: width =2, smoothing = 11 Include: Stripping, Esc peaks, Pile-up, Short tail

Table 3: MN8B - Scan & fitting parameters

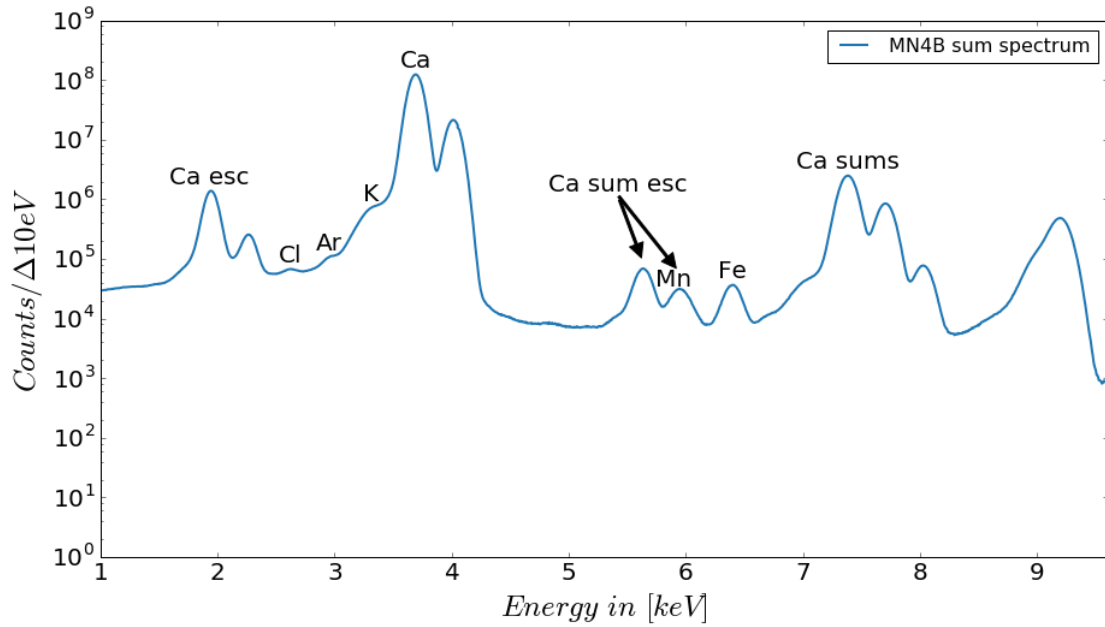


Figure 52: MN8B - Sum spectrum

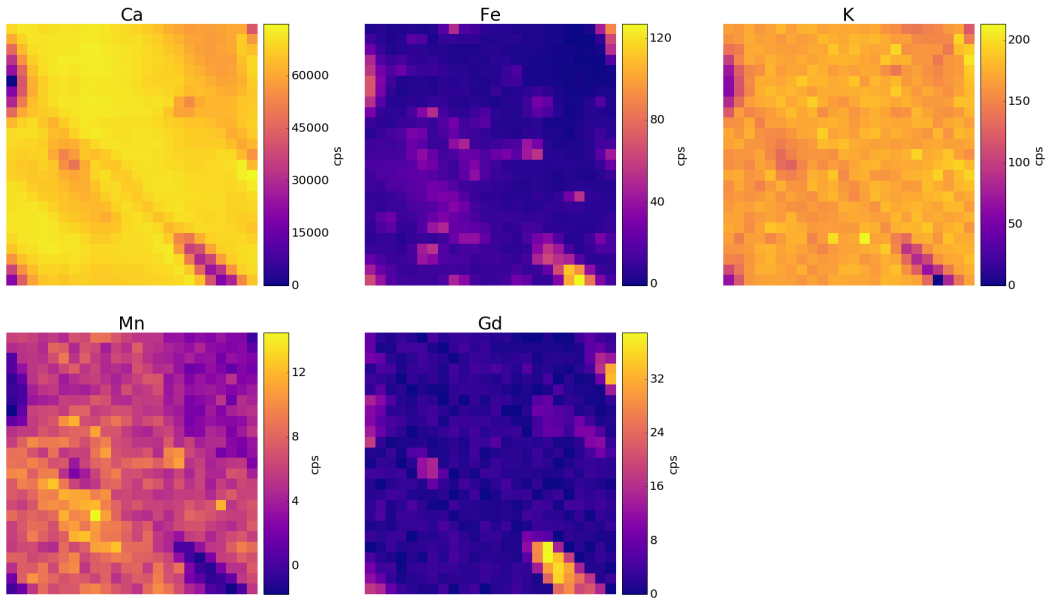


Figure 53: MN8B - Elemental maps of Ca (A), Fe (A), K (P), Mn (A) and Gd (P), where (A) := Axil-fitted and (P) := PyMca-fitted.

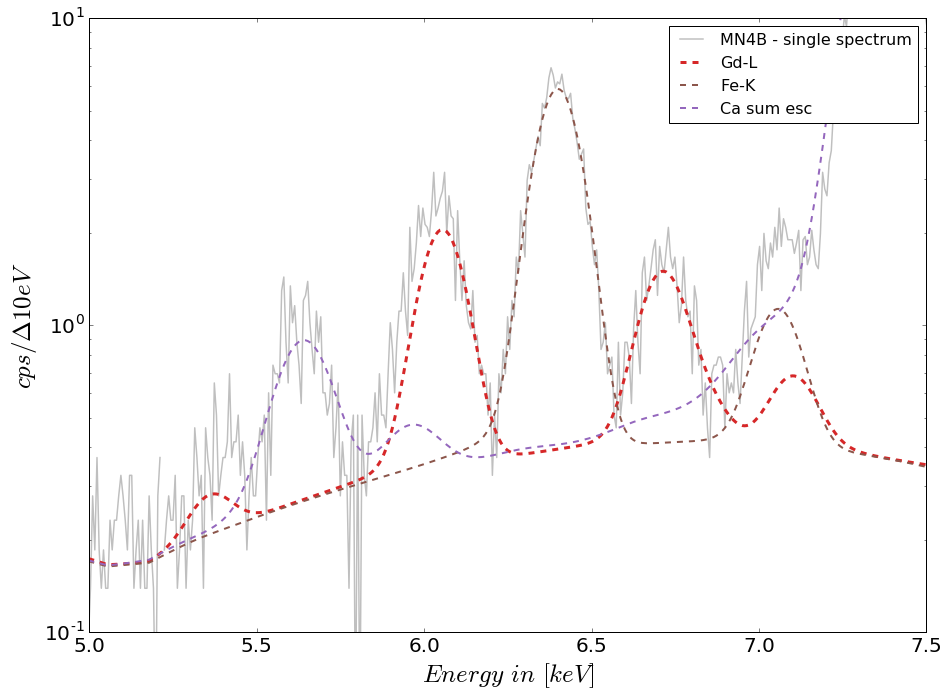


Figure 54: MN8B - Gd hotspot

Table 3 displays the scanning and fitting parameters. In Figure 52, the sum spectrum is presented. As for the previous sample (MN4B), Cl and Ar are visible in the sum spectrum, but not in the single spectra. Again, Mn is overlapping with the Ca-K α sum escape peak.

Figure 53 displays the obtained elemental maps. Even though they are difficult to fit, K and Mn were included.

As evidence that the sample does contain Gd, in Figure 54 a zoomed in part of the spectrum at the Gd hotspot (=highest count rate) on the sample is presented.

5.4.3. MN8 - Area C

Sample	MN8 - Area C
Excitation energy	9.2 keV
Stepsize	x = y = 25 μ m
Map-Size	29 x 25 pixel = 725 points = 700 x 600 μ m ²
Measuring time	60 s/point (real time)
Total measuring time	43500 s ~ 12 h
Mean dead-time	~22 %

Fitted elements	Ar, Ca, Cl, Cu, Fe, Gd, K, Mn, Cr, Ni
AXIL model	Ortpol: P=6, R=1.5
PyMca model	Hypermet, No Continuum, SNIP: width =67, smoothing = 19 Include: Stripping, Esc peaks, Pile-up, Short tail

Table 4: MN8C - Scan & fitting parameters

The scan and fitting parameters are presented in table 4. Figure 55 shows the obtained elemental maps. As before, there was a small contamination in the bottom right corner, containing Fe, Cr, Cu, Mn and Ni. Figure 56 shows a single spectrum at the Gd hotspot.

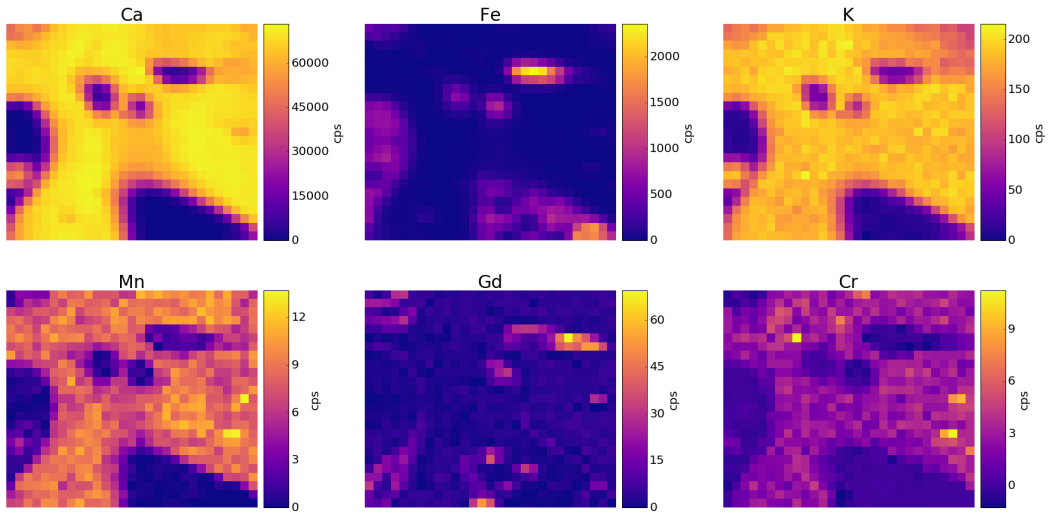


Figure 55: MN8C - Elemental maps of Ca (A), Fe (A), K (P), Mn (P), Gd (P), Cr (A), where (A) := Axil-fitted and (P) := PyMca-fitted.

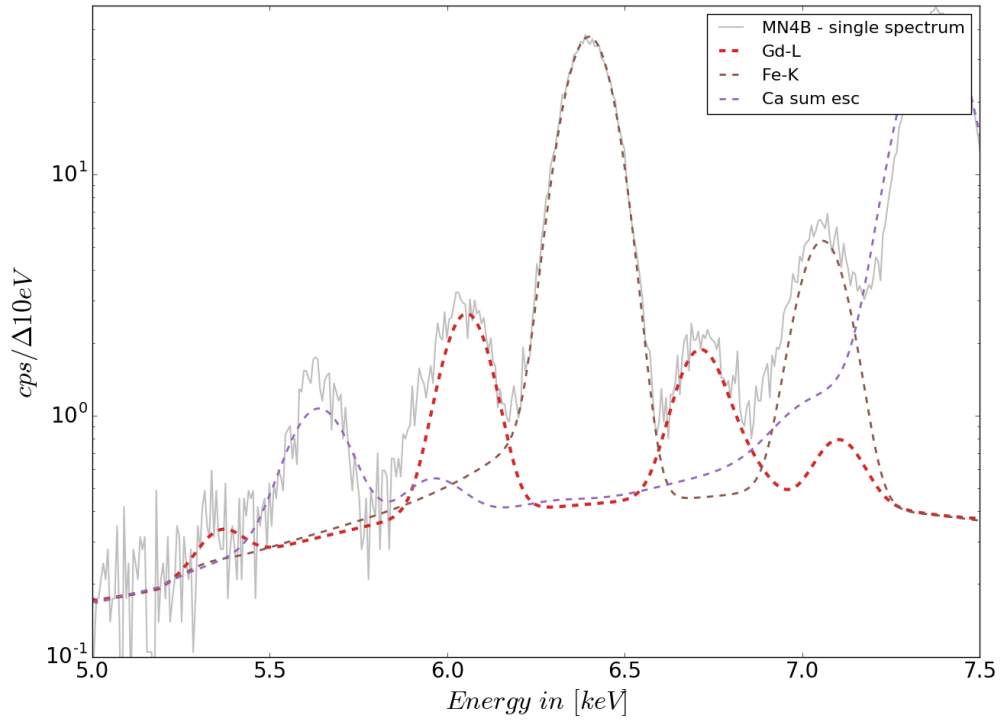


Figure 56: MN8C - Gd hotspot

5.4.4. TU14

Sample	TU14
Excitation energy	9.2 keV
Stepsize	$x = y = 30 \mu\text{m}$
Map-Size	$14 \times 63 \text{ pixel} = 882 \text{ points} = 390 \times 1860 \mu\text{m}^2$
Measuring time	60 s/point (real time)
Total measuring time	52920 s ~ 15 h
Mean dead-time	~8.6 %

Fitted elements	Ar, Ca, Cl, Cu, Fe, Gd, K, Mn, Cr, Ni, S
AXIL model	Ortpol: P=6, R=1.5
PyMca model	Hypermet, No Continuum, SNIP: width =63, smoothing = 19 Include: Stripping, Esc peaks, Pile-up, Short tail

Table 5: TU14 - Scan & fitting parameters

This sample is a tumorous bone sample (osteosarcoma tissue of proximal tibia, more information in [16]). Table 5 shows the scan and fitting parameters for this measurement. As before, some pixels with high concentrations of Cr, Fe, Mn and Ni were present. Thresholds were set for Cr (1000 counts), Fe (51500 counts), Mn (5100 counts) and Ni (17200 counts) to improve the contrast of other regions. Since S is overlapping with the Ca escape peak, S can not be fitted reliably in Ca high regions, therefore, the S counts are set to zero for points where the Ca countrate is above a threshold of 8300 cps. Figure 57 shows the resulting elemental maps. Even in air S is detectable, but vacuum conditions would be preferable, since ~90 % of the S radiation is absorbed in air. The Ni and Mn distributions show some similarity and there is some Cr in the same region, which suggests that this might be some kind of contamination from the sample preparations as well.

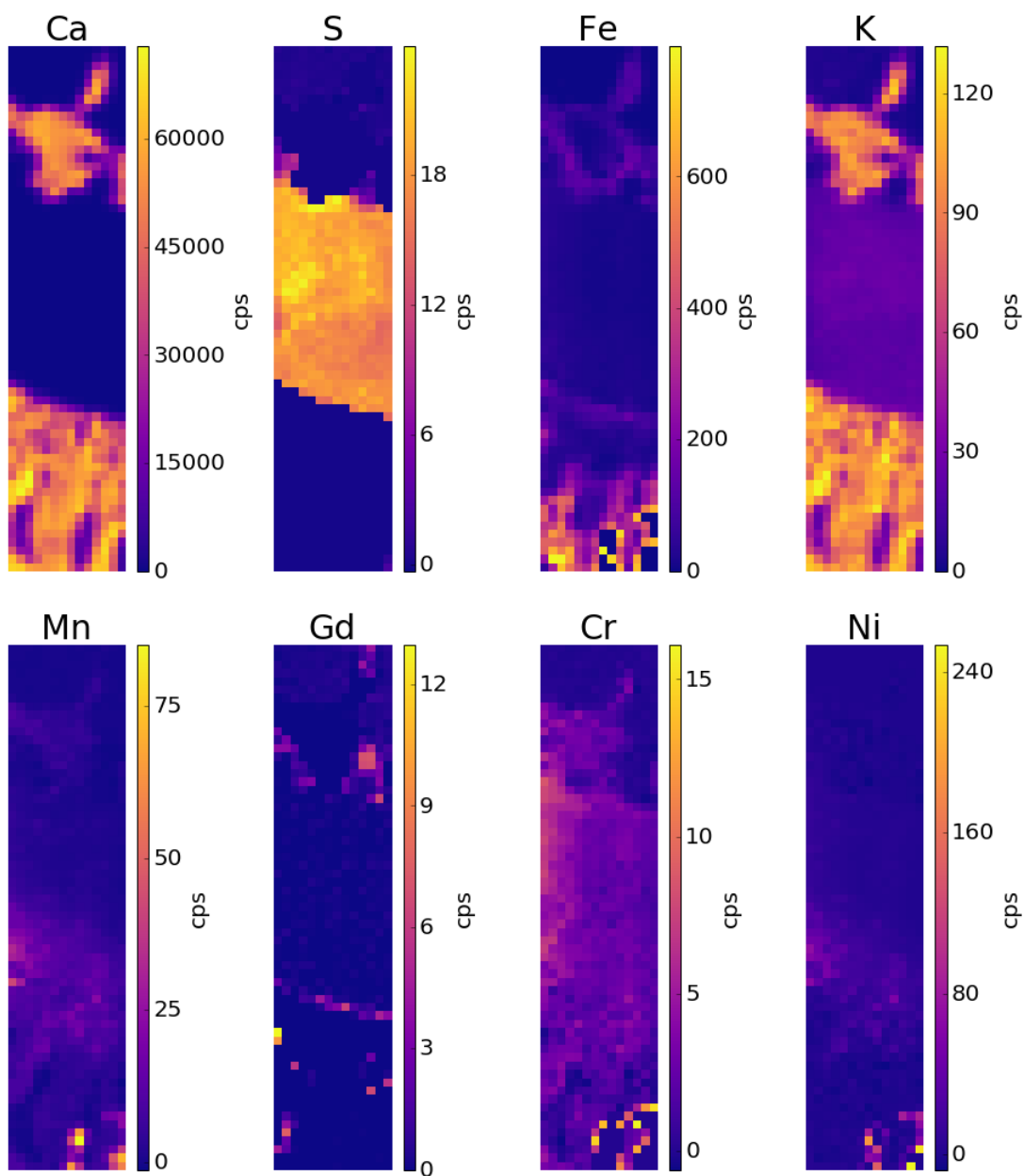


Figure 57: TU14 - Elemental maps of Ca (A), S (A), Fe (A), K (P), Mn (A), Gd (P), Cr (A), Ni (A), where (A) := Axil-fitted and (P) := PyMca-fitted.

Figure 58 displays single spectra acquired at two different points on the sample, one on a non-mineralized and the other on a mineralized region.

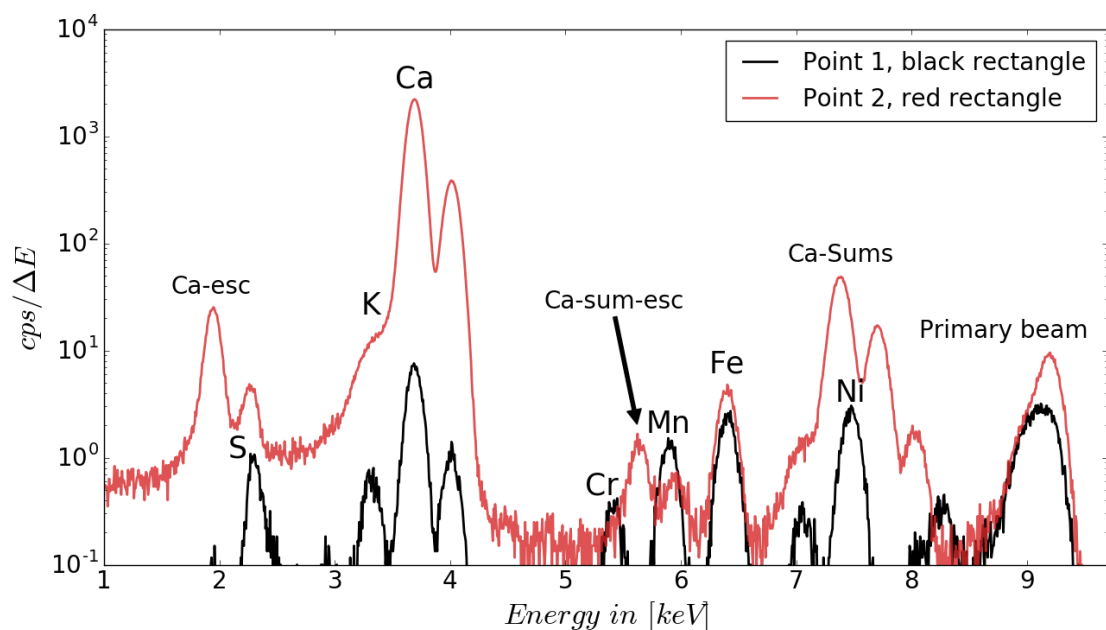


Figure 58: TU14 - Single spectra, acquired at two different positions in non-mineralized (Point 1, black) and mineralized (Point 2, red) region.

5.4.5. TUx1A

Sample	TUx1A
Excitation energy	9.2 keV
Stepsize	x = y = 25 μ m
Map-Size	27 x 23 pixel = 621 points = 650 x 550 μ m ²
Measuring time	60 s/point (real time)
Total measuring time	37260 s ~ 10 h
Mean dead-time	~27.4 %

Fitted elements	Ar, Ca, Cl, Cu, Fe, Gd, K, Mn, Cr
AXIL model	Ortpol: P=6, R=1.5
PyMca model	Hypermet, No Continuum, SNIP: width =63, smoothing = 19 Include: Stripping, Esc peaks, Pile-up, Short tail

Table 6: TUx1A - Scan & fitting parameters

In table 6, the scan and fitting parameters are presented. Figure 59 displays the resulting elemental maps. As before, a threshold was set for Cr (14 cps), Fe (123 cps) and

Mn (12.5 cps), in order to enhance the contrast of the rest of the maps. Figure 60 shows a single spectrum of the Gd hotspot.

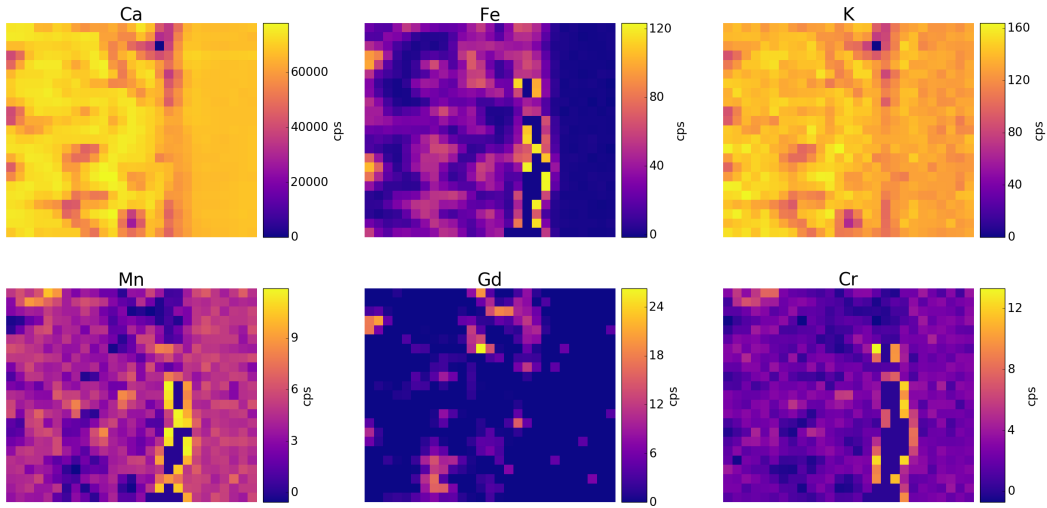


Figure 59: TUx1A - Elemental maps of Ca (A), Fe (A), K (P), Mn (A), Gd (P), Cr (A), where (A) := Axil-fitted and (P) := PyMca-fitted.

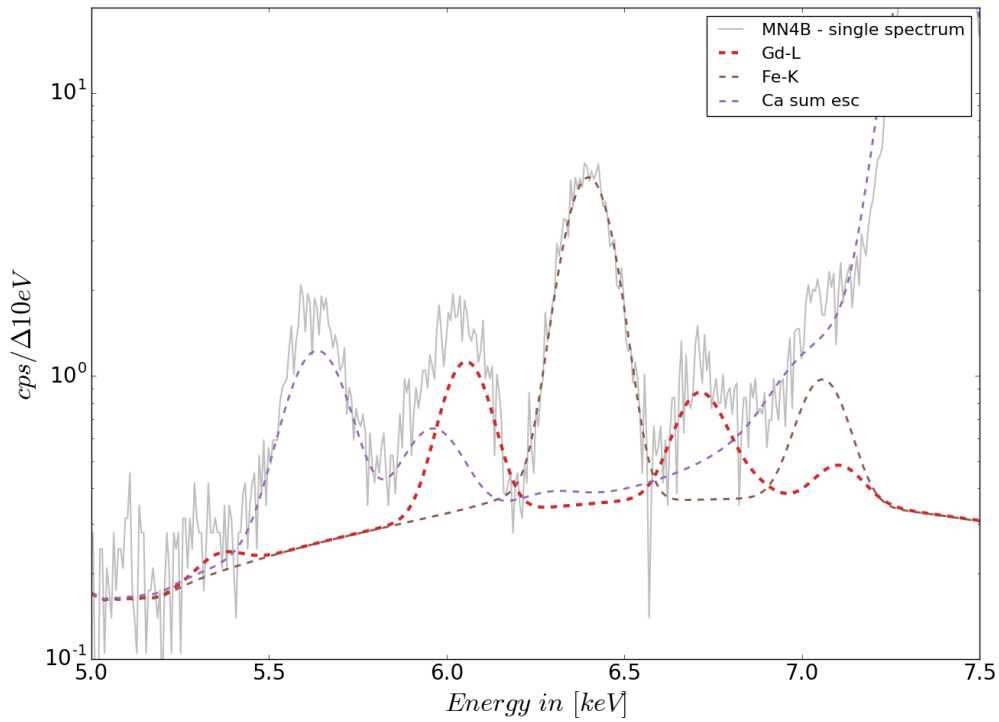


Figure 60: TUx1A - Gd hotspot

6. Conclusion

The main objectives of this thesis was to adapt and prepare the ATI μ XRF spectrometer for two beamtimes at the synchrotron facility ELETTRA and perform test measurements on different bone samples, in order to test the capabilities of the setup. While the μ XRF chamber was successfully set up during the first beamtime, some issues of this proposal were revealed. It proved to be more difficult than expected to adjust the half lens optic to the parallel beam, and the only available monochromator at the time was a silicon crystal monochromator, which is not the optimal choice for XRF experiments, hence, the synchrotron setup showed no improvement over the lab setup. Consequently, for the second beamtime, improved mechanisms for the precise adjustment of both the polycapillary optic and the whole chamber were designed, built and thoroughly tested. A superior polycapillary optic for the excitation channel was provided by IFG, and the crystal monochromator was replaced by a multilayer monochromator. As a result, the time frame for the adjustment procedure was shortened and the acquired data was superior to both the lab and the first beamtime experiments. Surface scans on five different bone samples were performed, analyzed and presented [17].

Additionally, the new data analysis and visualization software “LP-map” was developed. The software allows to interactively look at 2D scans, examine fitting results and easily create plots of acquired spectra and elemental maps. It also opens up the possibility to use PyMca for fitting, which has been tested on the measurements in this thesis, with results comparable to AXIL. “LP-map” can also be used to create elemental maps from data acquired with different XRF scanning instruments, e.g. ATI’s MAXI spectrometer or μ XRF data from synchrotron measurements.

As a future outlook, it would be interesting to test the capabilities of the new in-house fitting software “MKFIT” [18] for μ XRF spectra, and implement the processing of the fitted data in “LP-map”. Additionally, the extension to the visualization of 1D or maybe even 3D scans would be a natural next step.

References

- [1] A. Svirikova, A. Turyanskaya, L. Perneczky, C. Streli, and M. Marchetti-Deschmann. Multimodal imaging by MALDI MS and μ XRF. *submitted to Analyst*, 2018.
- [2] S. Smolek. Entwicklung eines energiedispersiven Mikro-Röntgenfluoreszenzspektrometers zur Analyse leichter Elemente. Master's thesis, TU Wien, 2014.
- [3] S. Smolek, B. Pemmer, M. Fölser, C. Streli, and P. Wobrauschek. Confocal micro-x-ray fluorescence spectrometer for light element analysis. *Review of Scientific Instruments*, 83(8):083703, 2012.
- [4] A. Turyanskaya, M. Rauwolf, T.A. Grünewald, M. Meischel, S. Stanzl-Tschegg, J.F. Löffler, P. Wobrauschek, A.M. Weinberg, H.C. Lichtenegger, and C. Streli. μ XRF Elemental Mapping of Bioresorbable Magnesium-Based Implants in Bone. *Materials*, 9(10):811, 2016.
- [5] Werner Jark, Diane Eichert, Lars Luehl, and Alessandro Gambitta. Optimisation of a compact optical system for the beamtransport at the x-ray Fluorescence beamline at Elettra for experiments with small spots. In *Advances in X-Ray/EUV Optics and Components IX*, volume 9207, page 92070G. International Society for Optics and Photonics, 2014.
- [6] M. Haschke. *Laboratory Micro-X-Ray Fluorescence Spectroscopy*. Springer, 2014.
- [7] R. Klockenkämper and A. von Bohlen. *Total-Reflection X-Ray Fluorescence Analysis and Related Methods*. Chemical Analysis: A Series of Monographs on Analytical Chemistry and Its Applications. Wiley, 2015.
- [8] C. Streli. Lecture notes for X-Ray Analytical Methods, 2016.
- [9] B. Beckhoff, B. Kanngießer, N. Langhoff, R. Wedell, and H. Wolff. *Handbook of Practical X-Ray Fluorescence Analysis*. 2006.
- [10] A. von Bohlen and M. Tolan. Editorial for Synchrotron Radiation. *J. Anal. At. Spectrom.*, 23:790–791, 2008.
- [11] International Atomic Energy Agency. *Quantitative X Ray Analysis System*. Number 21 in Computer Manual Series. International Atomic Energy Agency, Vienna, 2009.

- [12] V.A. Solé, E. Papillon, M. Cotte, Ph. Walter, and J. Susini. A multiplatform code for the analysis of energy-dispersive X-ray fluorescence spectra. *Spectrochimica Acta Part B: Atomic Spectroscopy*, 62(1):63 – 68, 2007.
- [13] J. Lubeck, M. Bogovac, B. Boyer, B. Detlefs, D. Eichert, R. Fliegauf, D. Grötzsch, I. Holfelder, P. Hönicke, W. Jark, R. B. Kaiser, B. Kanngießer, A. G. Karydas, J. J. Leani, M. C. Lépy, L. Lühl, Y. Ménesguen, A. Migliori, M. Müller, B. Pollakowski, M. Spanier, H. Sghaier, G. Ulm, J. Weser, and B. Beckhoff. A new generation of x-ray spectrometry UHV instruments at the SR facilities BESSY II, ELETTRA and SOLEIL. *AIP Conference Proceedings*, 1741(1):030011, 2016.
- [14] Elettra XRF beamline specifications. <https://www.elettra.trieste.it/lightsources/elettra/elettra-beamlines/microfluorescence/specifications.html>.
- [15] P. Wobrauschek. Total reflection X-ray fluorescence analysis - a review. *X-Ray Spectrometry*, 36(5):289–300, 2007.
- [16] Mirjam Rauwolf, Bernhard Pemmer, Andreas Roschger, Anna Turyanskaya, Stephan Smolek, Angelika Maderitsch, Peter Hischenhuber, Martin Foelser, Rolf Simon, Susanna Lang, et al. Increased zinc accumulation in mineralized osteosarcoma tissue measured by confocal synchrotron radiation micro X-ray fluorescence analysis. *X-Ray Spectrometry*, 46(1):56–62, 2017.
- [17] L. Perneczky, M. Rauwolf, D. Ingerle, D. Eichert, F. Brigidi, W. Jark, S. Bjeoumikhova, G. Pepponi, P. Wobrauschek, C. Streli, and A. Turyanskaya. Temporary implementation and testing of a confocal SR- μ XRF system for bone analysis at the X-Ray Fluorescence beamline at Elettra. *submitted to Nuclear Instruments & Methods in Physics Research A*, 2018.
- [18] M. Kraihamer. Optimization of a low power spectrometer for total reflection X-ray fluorescence analysis. Master’s thesis, TU Wien, 2017.

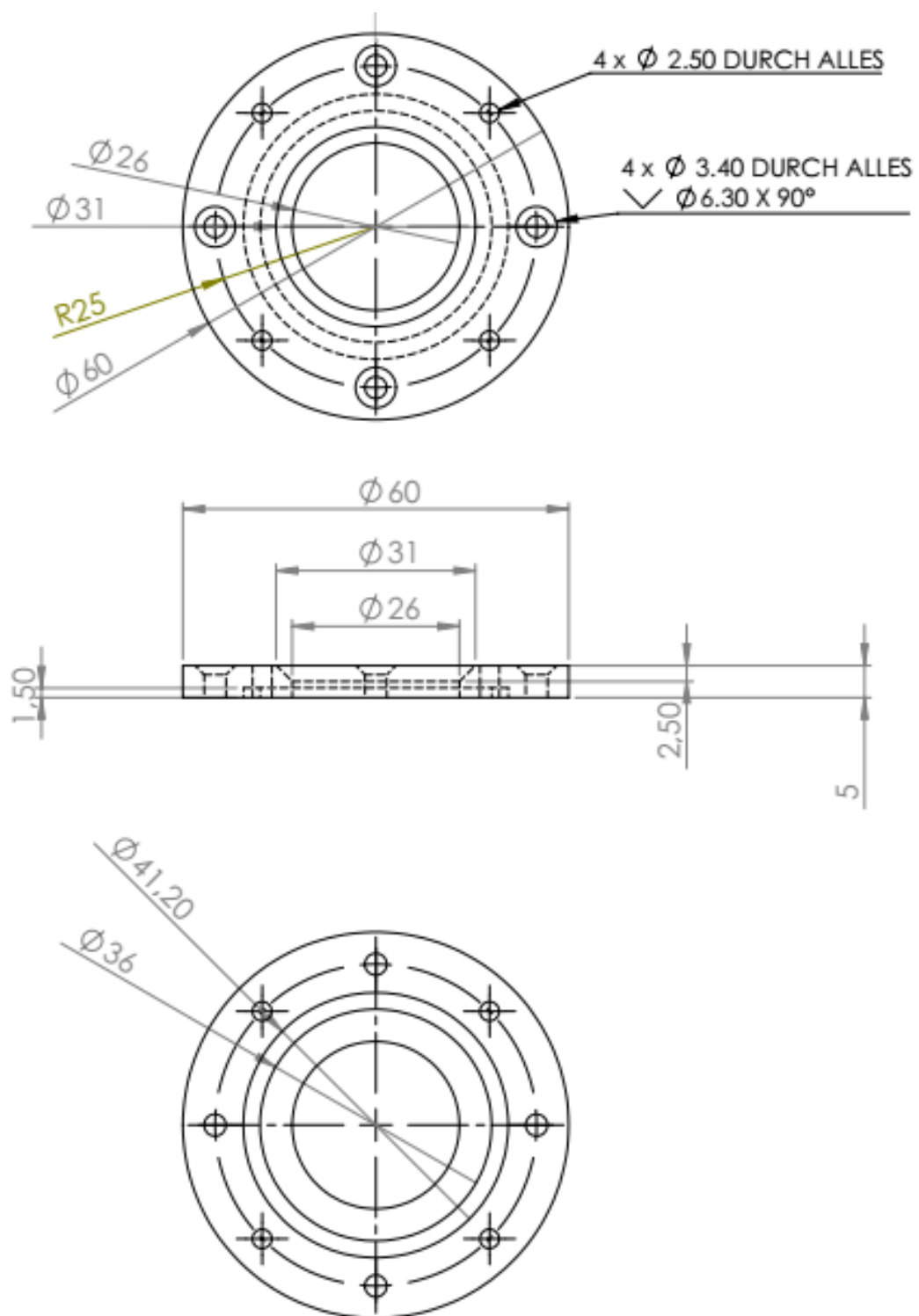


Figure 62: Ketek detector - plexiglas ring.

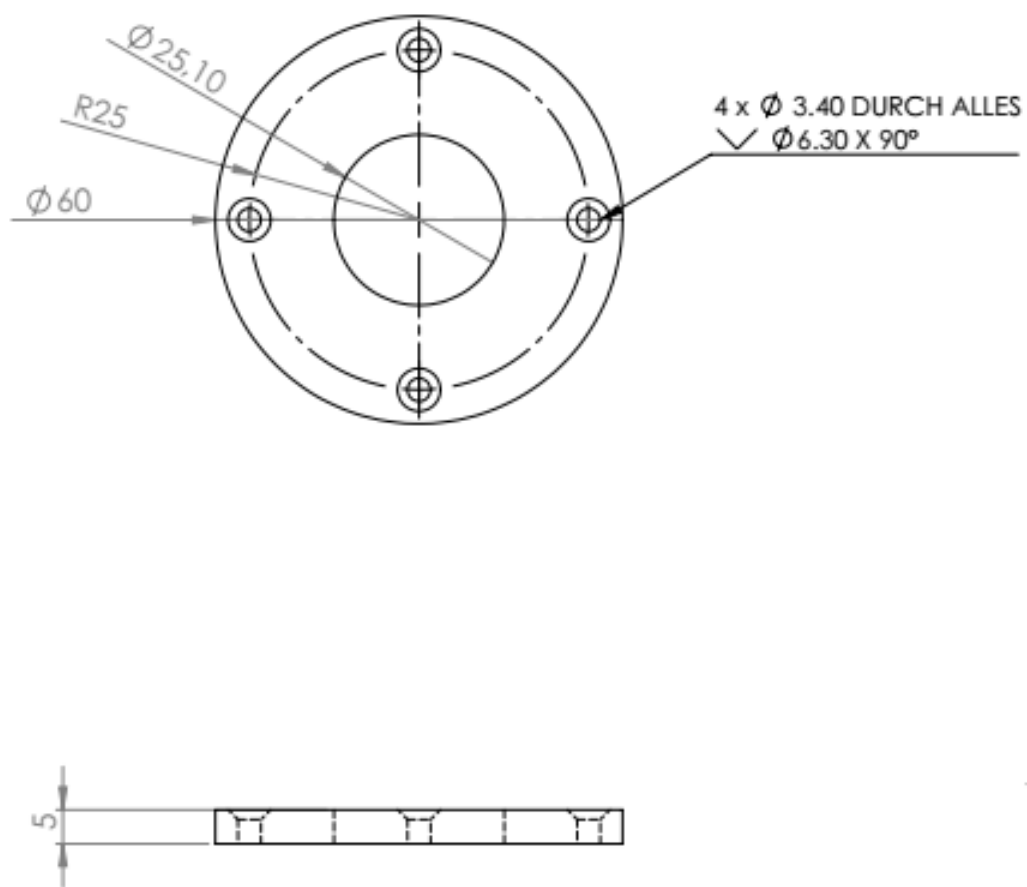


Figure 63: Ketek detector - aluminium counterpiece.

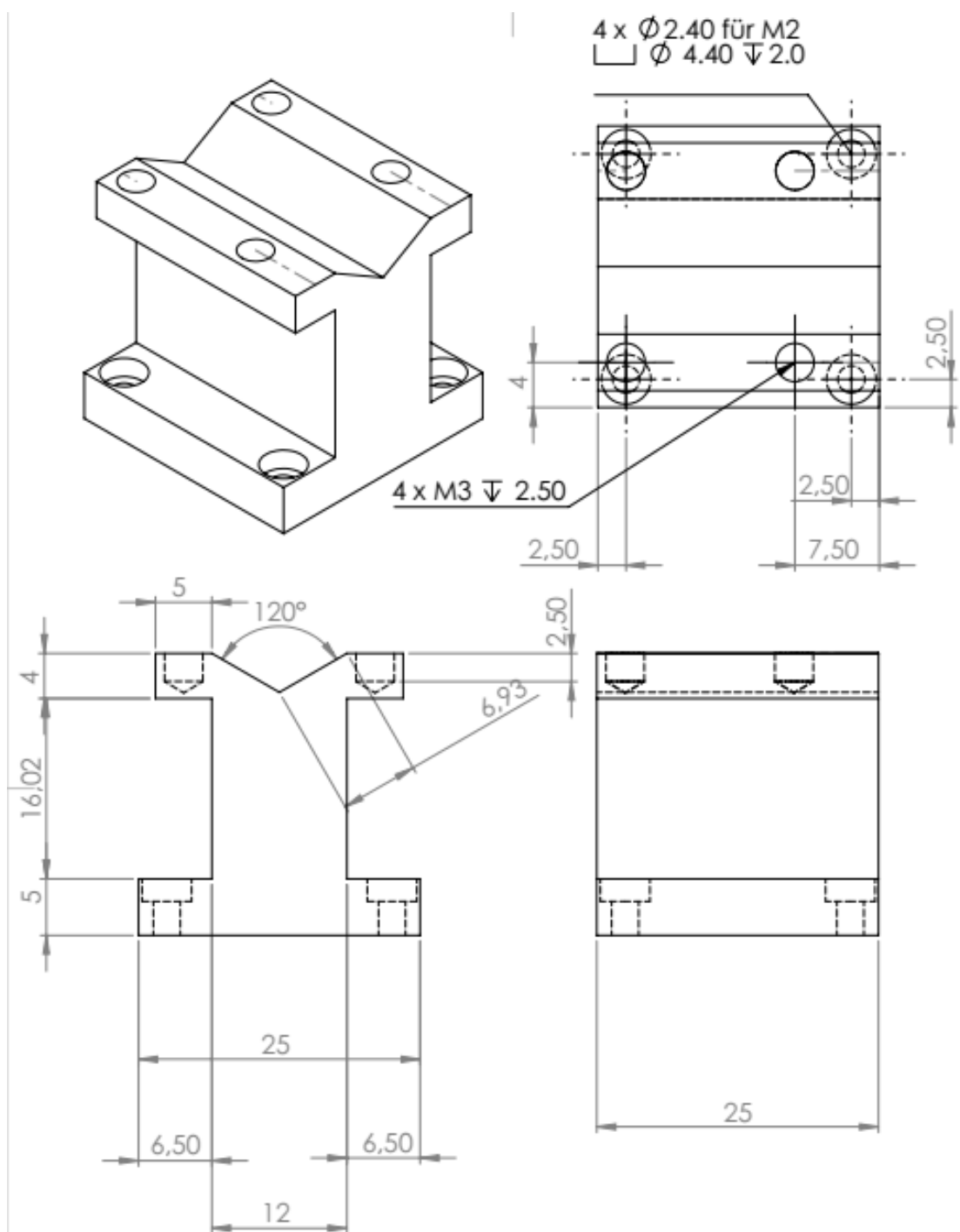


Figure 64: Plexiglas polycapillary holder.

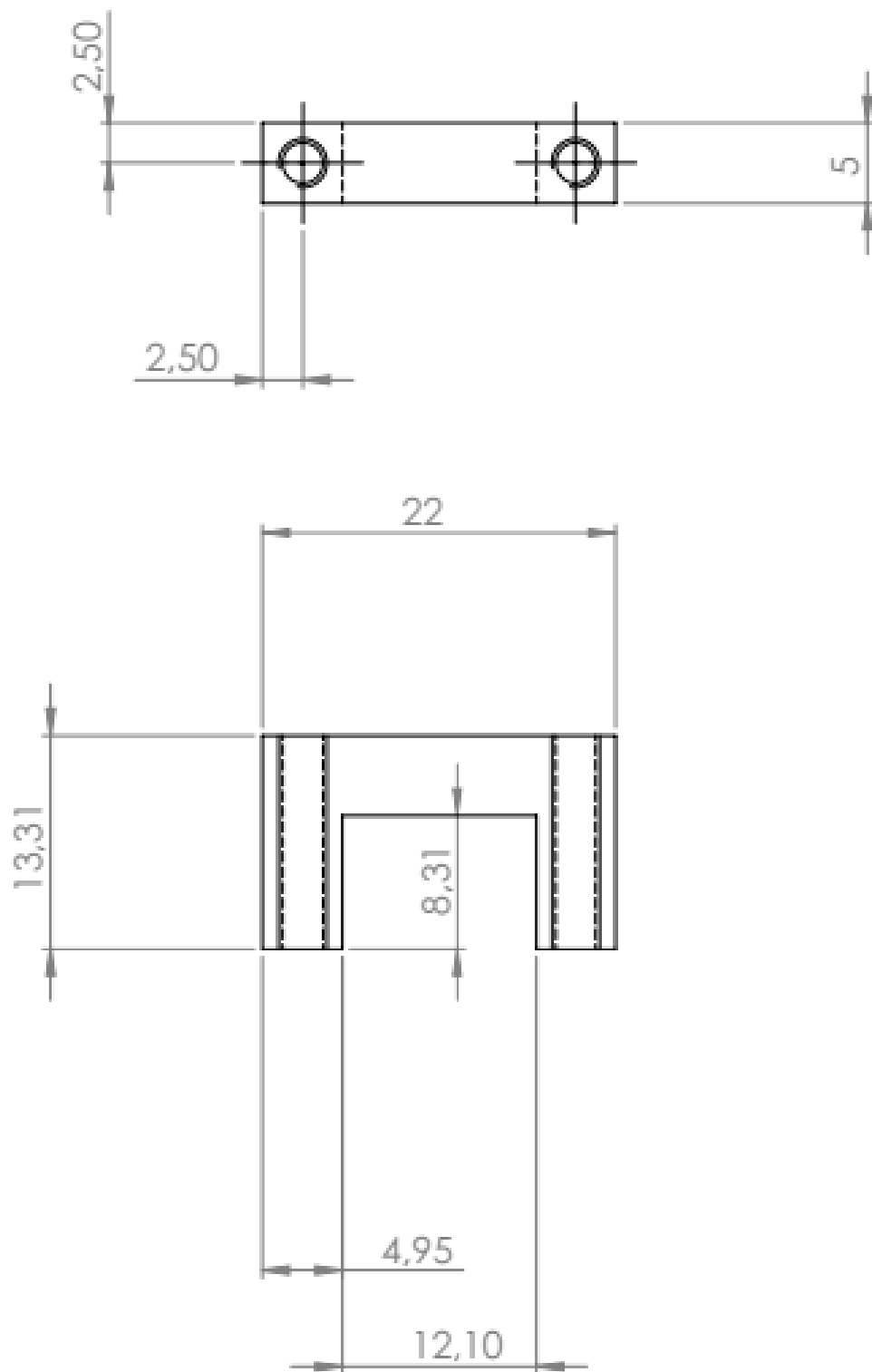


Figure 65: Aluminium hooks for polycapillary holder.

A.2. Second beamtime

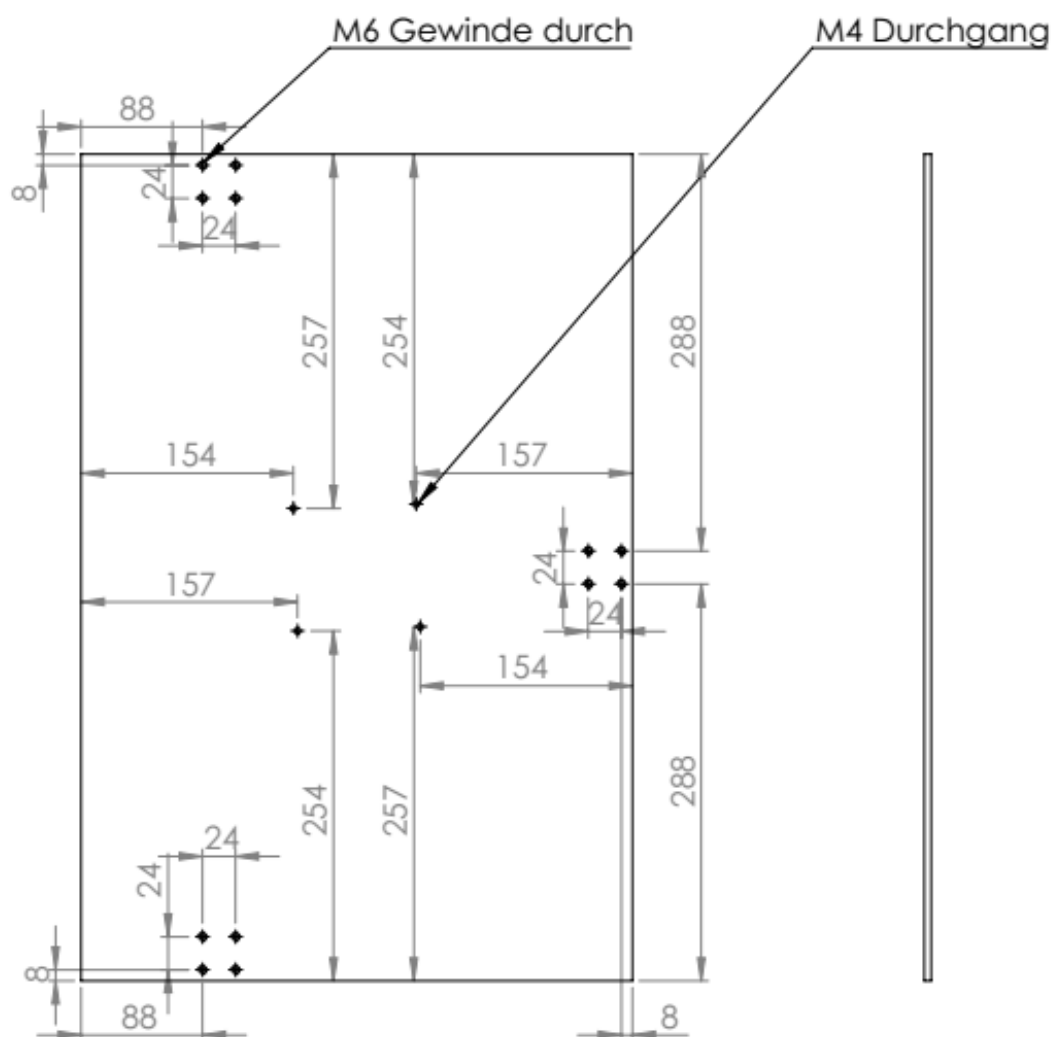


Figure 66: Base construction, middle plate.

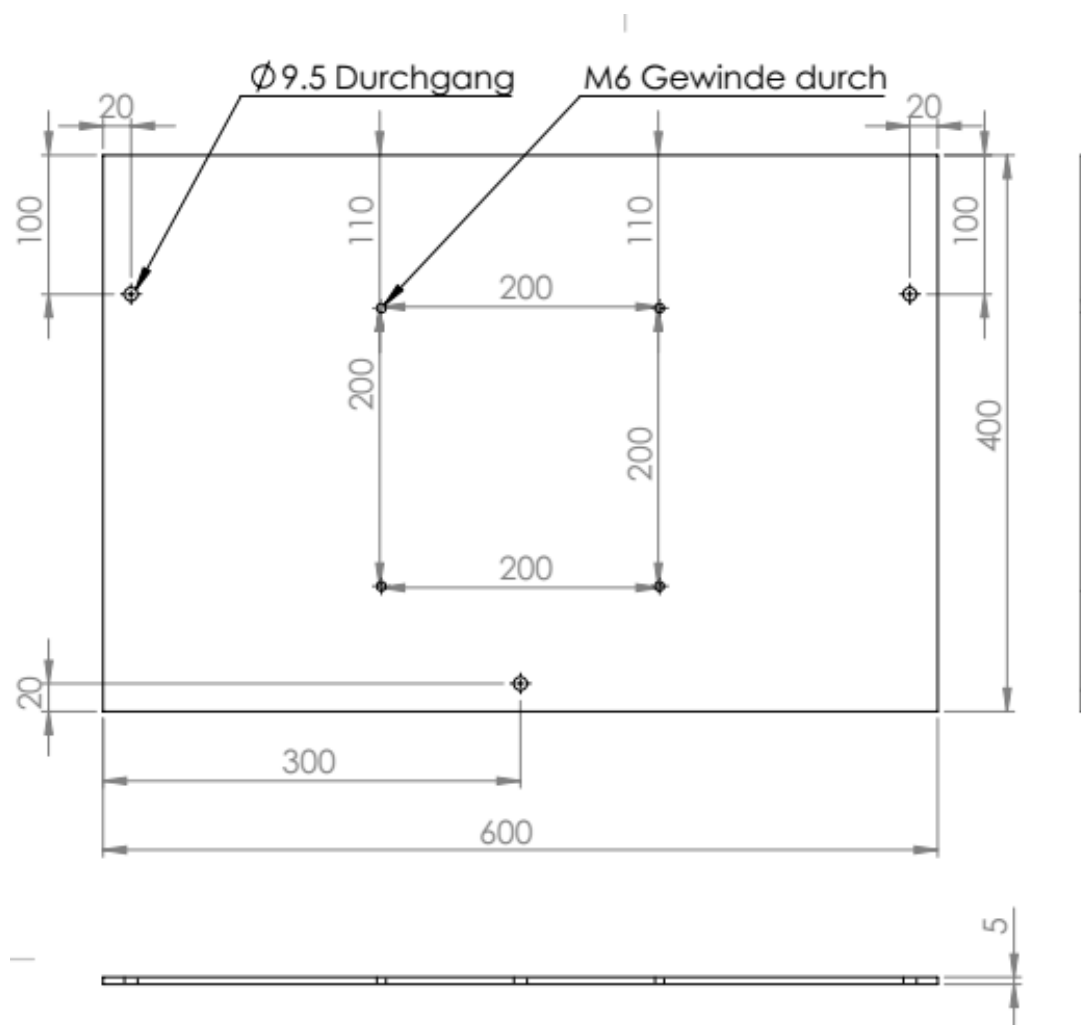


Figure 67: Base construction, top plate.

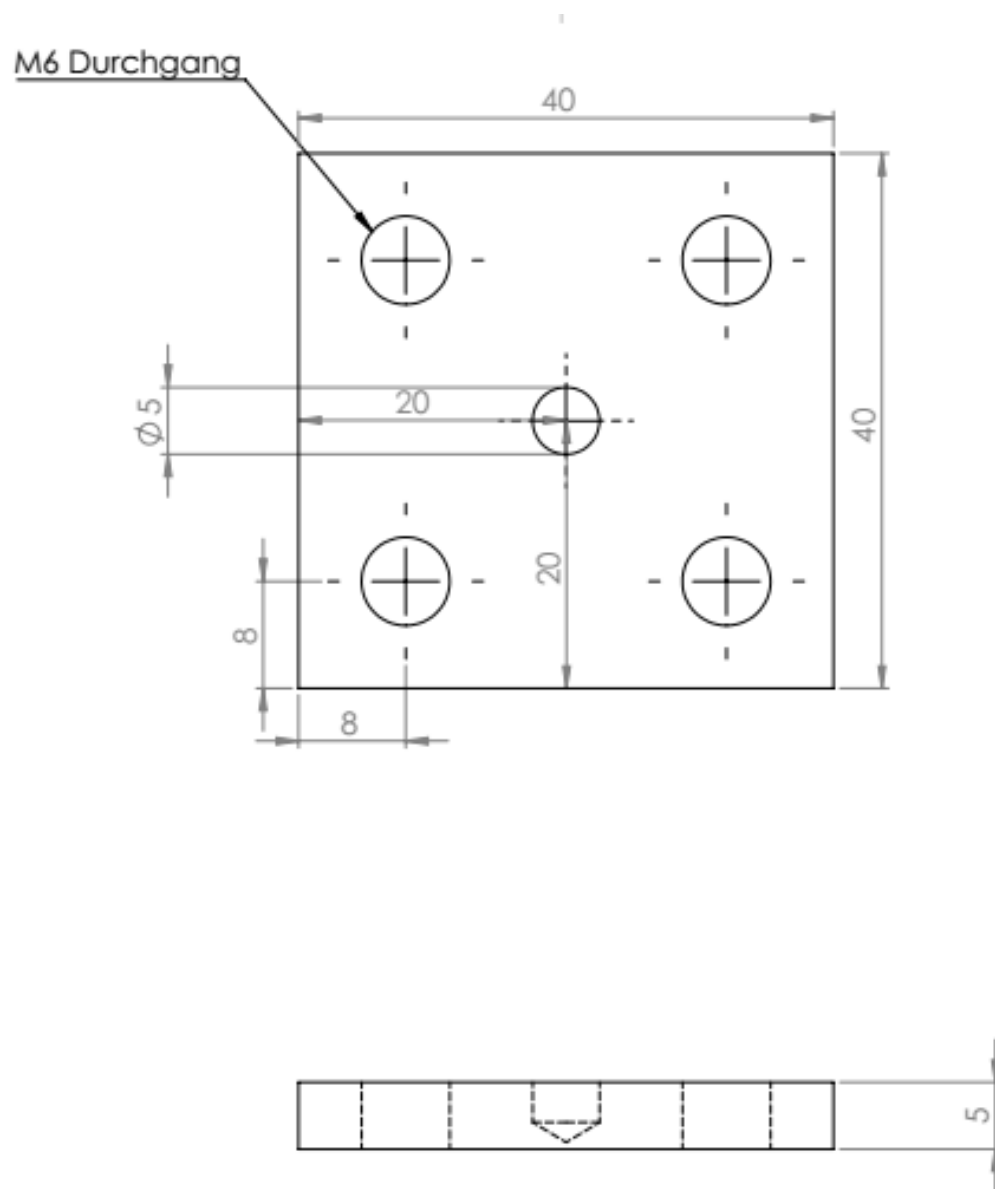


Figure 68: Brass support for micrometer screws.

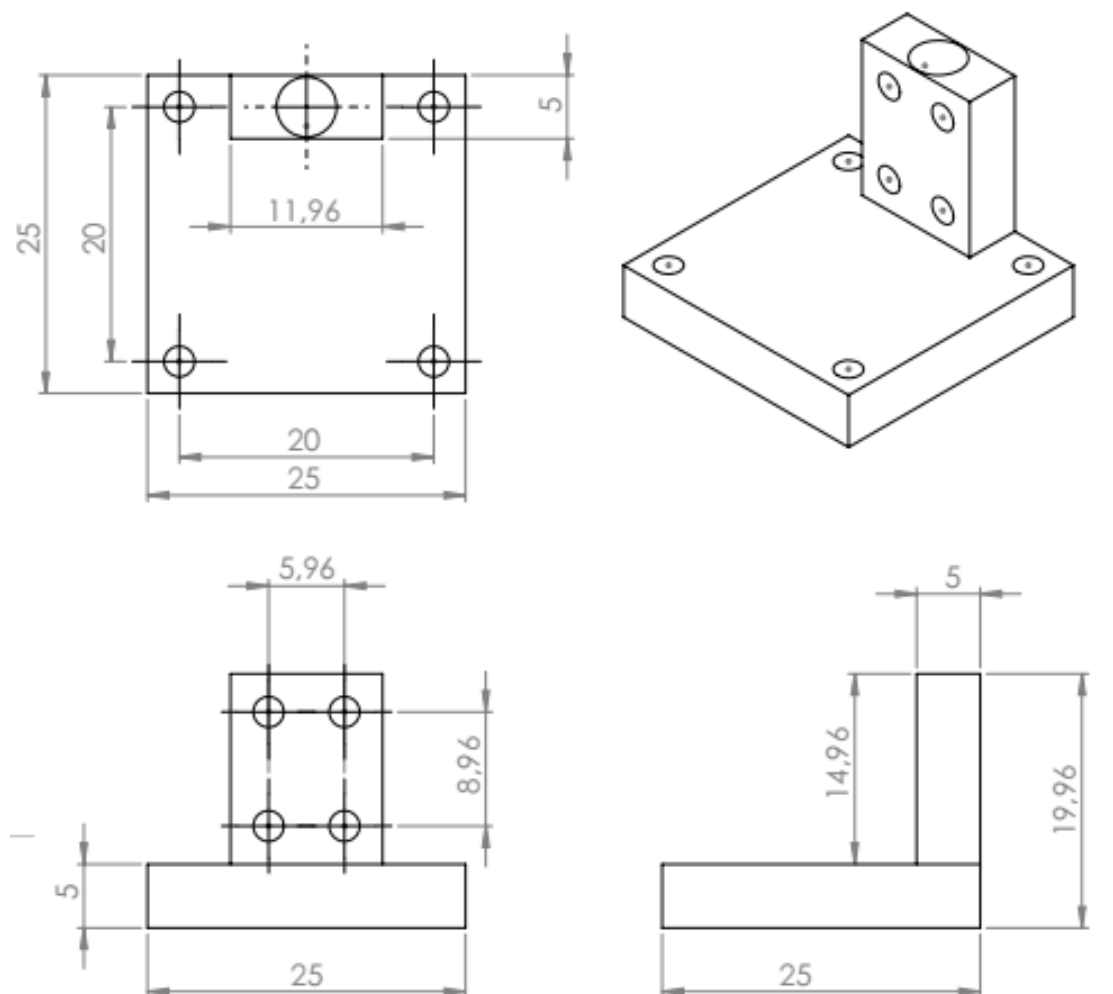


Figure 69: Polycapillary holder.

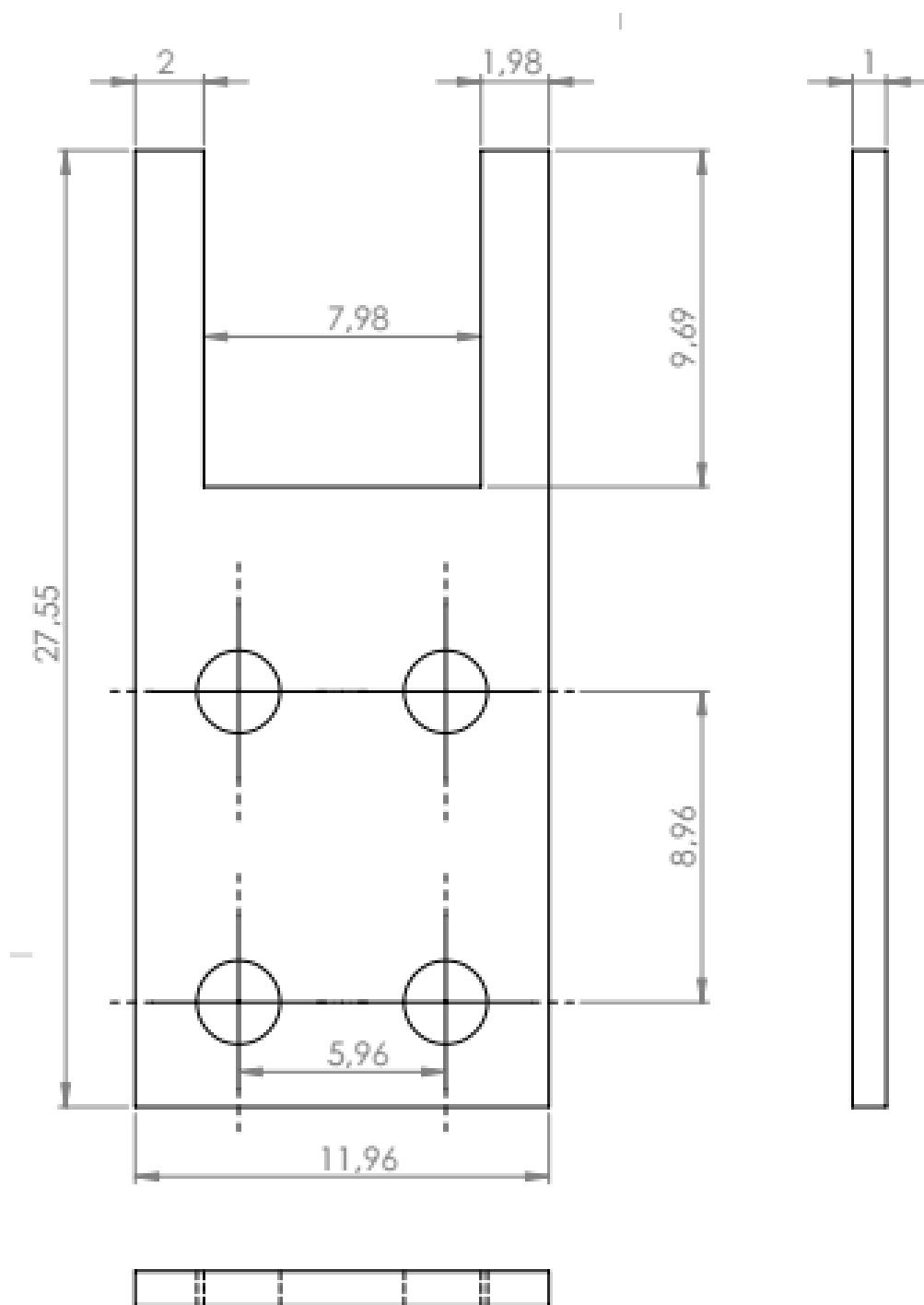


Figure 70: Polycapillary U-Stabilizer.

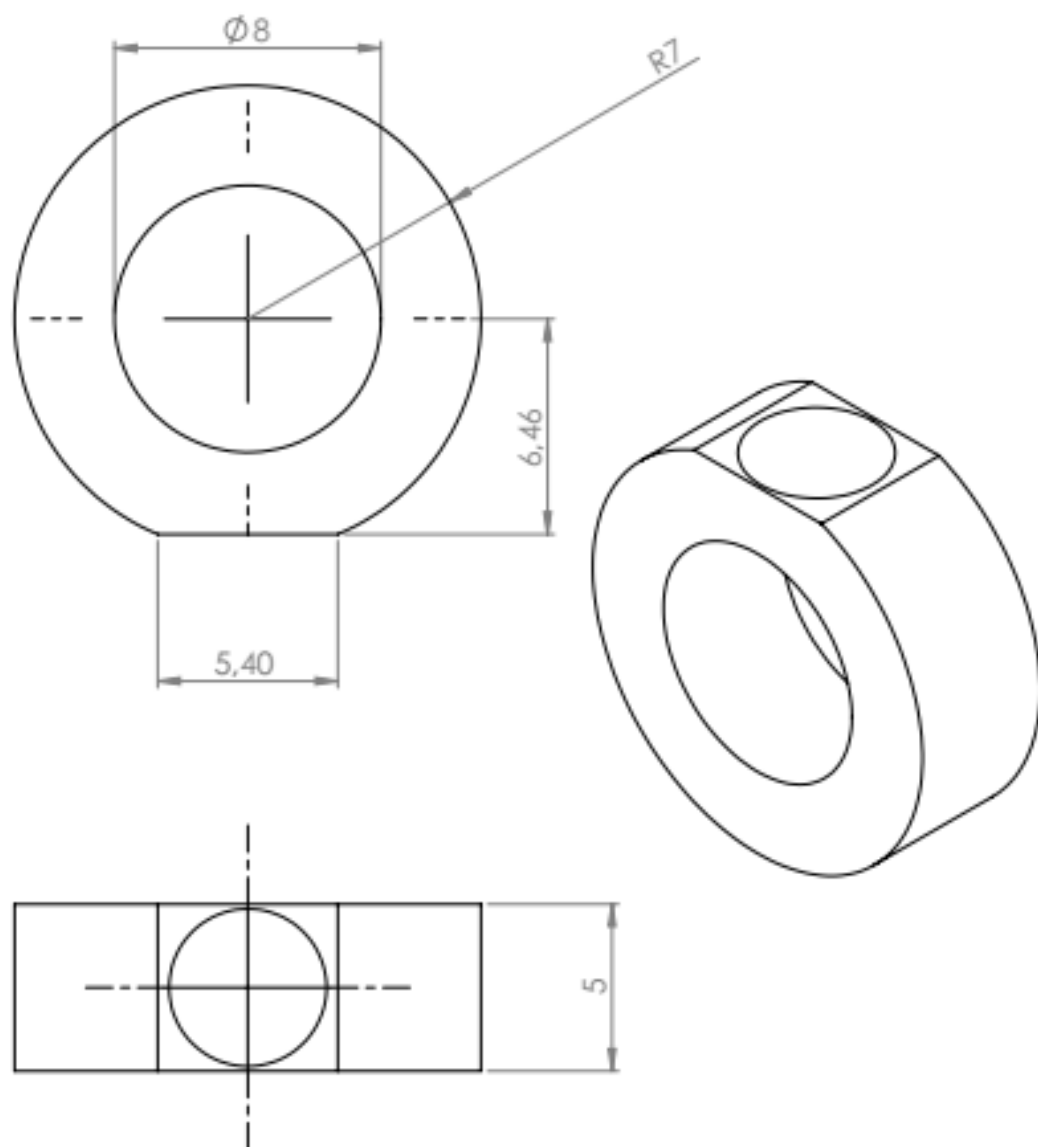


Figure 71: Polycapillary ring with joint indentation.

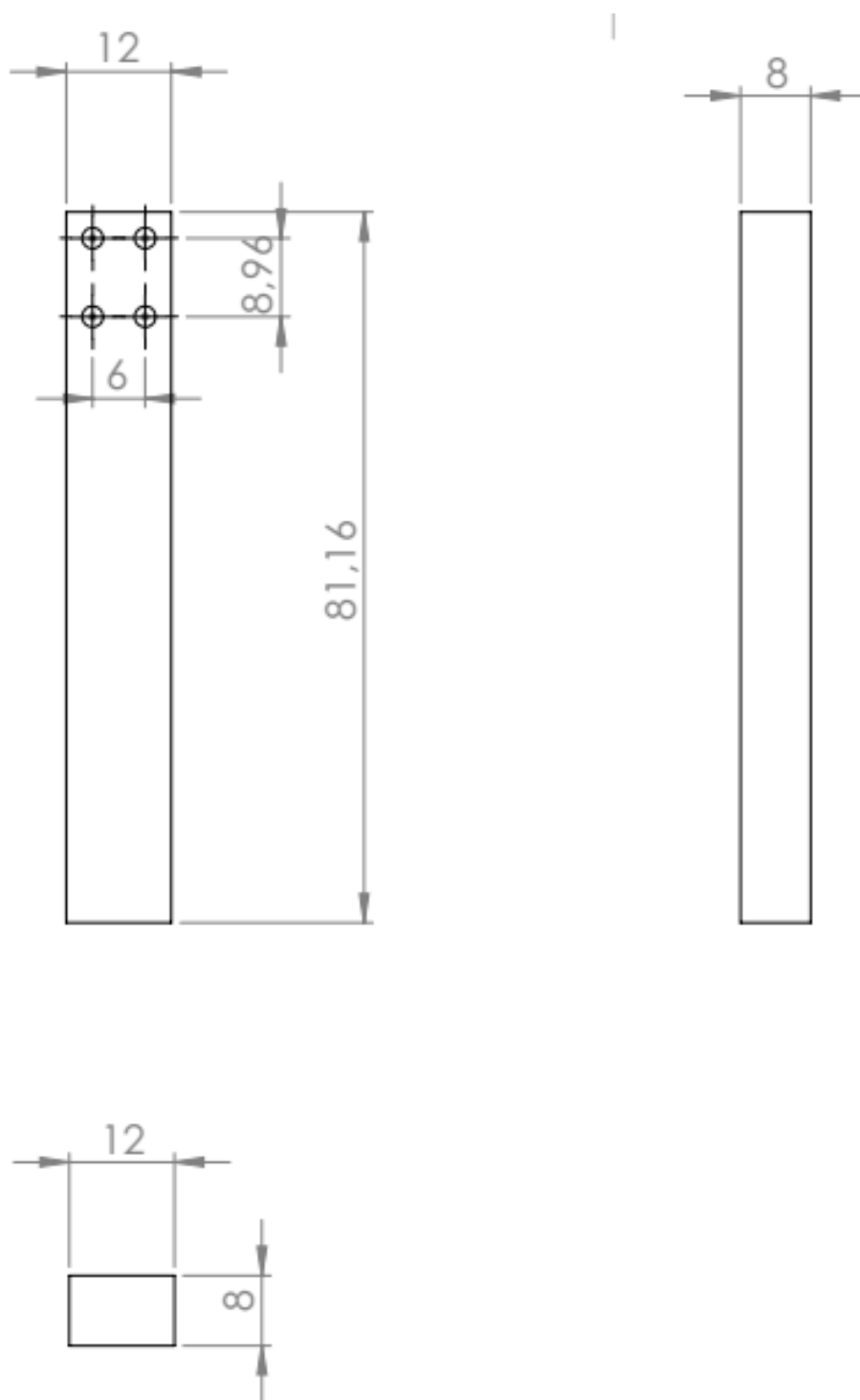


Figure 72: Polycapillary front support pole.

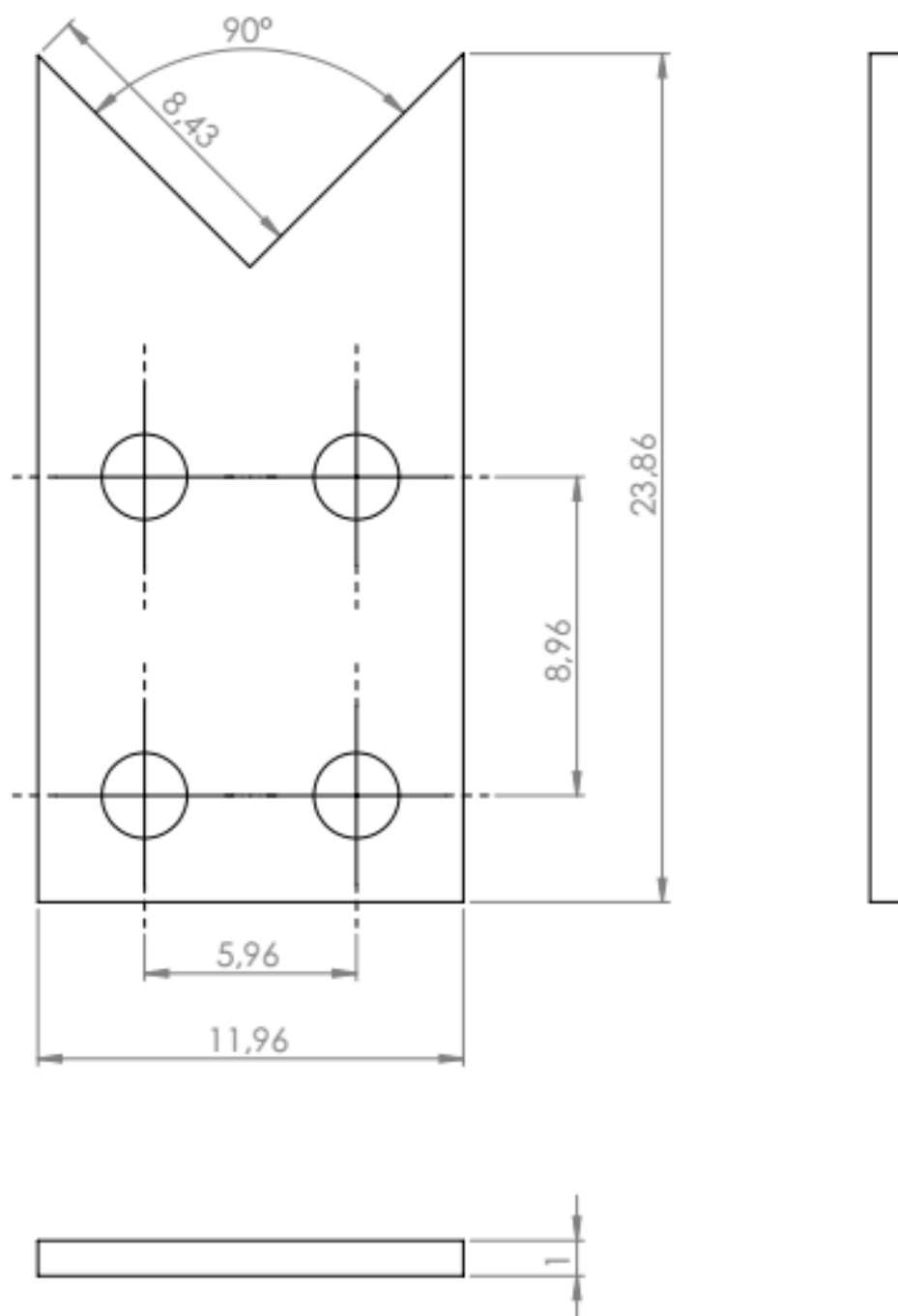


Figure 73: V-shaped front support.